

---

# Site C0013<sup>1</sup>

---

Expedition 331 Scientists<sup>2</sup>

## Chapter contents

Background and objectives	1
Operations	2
Lithostratigraphy	3
Biostratigraphy	6
Petrology	6
Geochemistry	10
Microbiology	13
Physical properties	14
References	15
Figures	17
Tables	59

## Background and objectives

Integrated Ocean Drilling Program (IODP) Site C0013 is located ~100 m east of the main hydrothermal mound chains of the Iheya North hydrothermal field (see Fig. F3 in Expedition 331 Scientists, 2011a). This area is characterized by patchy occurrences of numerous diffuse flow sites and associated chemosynthetic animal colonies, chiefly mussels and galetheid crabs. Most of the seafloor in the area is covered with pumiceous breccia and barite-anhydrite-carbonate crusts, whereas some of the bathymetric depressions host thin hemipelagic sediments.

A heat flow survey of the entire hydrothermal field (Fig. F1) shows that Site C0013 is located in a zone of relatively high heat flow, with a surficial temperature gradient estimated before drilling to be ~3°C/m, and is highly impacted by high-temperature fluids. A multichannel seismic survey predicts that nonstratified pumiceous pyroclastic deposits underlie the seafloor to a pronounced seismic reflector at 50–60 meters below seafloor (mbsf) (see Fig. F5 in Expedition 331 Scientists, 2011a). This reflector may be the boundary between volcanic basement and the overlying pyroclastic deposits, or it may simply be a hard layer within these deposits that would likely impede hydrothermal flow. Discovering the nature of this seismic reflector at 50–60 mbsf was an important drilling objective at Site C0013 that we failed to achieve because we were unable to drill deeper than 54.5 mbsf.

The scientific objectives for Site C0013 are similar to those for Expedition 331 as a whole, namely, to test for direct evidence of a “subvent biosphere”; to clarify the architecture, function, and impact of subseafloor microbial ecosystems; and to establish their relationship to the physical, geochemical, and hydrogeologic variations within a high-input hydrothermal mixing zone. Pore water chemistry and microbial community characterization of cores that penetrated <1 mbsf (J. Ishibashi et al., unpubl. data) suggest that microbial community structure changes rapidly with depth, from a psychrophilic-mesophilic methane-consuming community at shallow depth to a thermophilic-hyperthermophilic methane-producing community deeper. The shift in microbial community is likely associated with physical and chemical variations in pore water, in which the hydrothermal input increases with depth and where it will be heavily affected by spatial and temporal fluctuations in mixing between discharging hot hydrothermal fluid and recharging cold seawater.

<sup>1</sup>Expedition 331 Scientists, 2011. Site C0013. In Takai, K., Mottl, M.J., Nielsen, S.H., and the Expedition 331 Scientists, *Proc. IODP, 331*: Tokyo (Integrated Ocean Drilling Program Management International, Inc.).  
doi:10.2204/iodp.proc.331.103.2011

<sup>2</sup>Expedition 331 Scientists' addresses.

## Operations

### Arrival at Site C0013

The D/V *Chikyu* arrived at Site C0013 (Table T1) during the night of 8 September 2010, drifted the last mile, and set azimuth thrusters. The ship switched to dynamic positioning mode during the early hours of 9 September and sent the remotely operated vehicle (ROV) down to set five transponders. After the transponders were calibrated, we conducted a seabed survey with the ROV and picked the spot for the hard seabed guide base (27°47.831'N, 126°57.799'E) (Fig. F2). The ship repositioned, the guide base was lowered to the seabed, and the ROV locked the well head into a vertical position.

### Hole C0013A

After the seabed survey, on 10 September 2010 the decision was made to core a few pilot holes with the hydraulic piston coring system (HPCS) before committing to the main hole in the guide base. A perfluoromethylcyclohexane (PFC) contamination tracer was added to the active mud tank, and we decided to use microbeads with every HPCS and extended punch coring system (EPCS)/extended shoe coring system (ESCS) core. A plan to sample the drill mud from the active tank every 12 h was enacted.

The first coring attempt was 11 m east of the guide base (Fig. F2). The first run down to the seabed used the advanced piston corer temperature tool (APCT3) shoe, taking a temperature measurement just above the seabed. Following that, however, the HPCS did not fire when the mud pump rate was increased. The core barrel was pulled back up, reassembled, and sent back down. When it arrived at the seabed, we saw that the coring shoe was not protruding from the drill bit as it is designed to do. Before any action could be taken, the pins sheared and we watched the inner barrel slide to the seabed. We attempted to use slow pumping to push the inner barrel into the seabed in order to get core, but the inner barrel bent at the 8.5 m marker and snapped off. The bent and broken barrel required a full pipe trip to recover, leaving the lower half of the core barrel and the APCT3 tool on the seabed. Thus ended Hole C0013A.

### Hole C0013B

On 10 September 2010, immediately following Hole C0013A operations, the ship offset 2 m south and tripped the HPCS/ESCS/EPCS coring assembly to the seafloor. The EPCS inner barrel was dropped to the bit this time, cutting the first and only core in Hole C0013B (Fig. F2). As the core was pulled back up to

surface, the bit inadvertently pulled out of the hole, ending Hole C0013B.

### Hole C0013C

Hole C0013C was spudded with the HPCS on 11 September 2010, 5 m south of Hole C0013B (Fig. F2). When the inner barrel was recovered, the liner was stuck in the barrel and the core had to be pumped out. This was only partially successful. The drill bit again pulled out of the hole, so the ship offset once more to drill Hole C0013D.

### Hole C0013D

Hole C0013D was spudded on 11 September 2010, 2 m north of Hole C0013C (Fig. F2). After drilling to 3 mbsf so the bit would stay in the seabed, the first HPCS core recovered 95% of a 9.5 m advance. More than 200 ppm H<sub>2</sub>S was venting from the coring shoe, dispersing quickly to 98 ppm by the time the shoe was off. Core 331-C0013D-2H was shot using the HPCS and successfully recovered. The barrel came up too hot to touch, and the liner showed signs of melting; recovery on this attempt was only 15% of a 9.5 m advance. (The acrylic plastic becomes soft at 82°C at surface pressure conditions, as shown by a simple test done by Center for Deep Earth Exploration [CDEX] engineers; data not shown.) We switched to the EPCS to get through what seemed to be a hard layer that reduced HPCS recovery. A 4 m advance using the EPCS recovered 20% sediment. A subsequent switch to the ESCS gave only 1% recovery and a melted liner, so Hole C0013D was abandoned after reaching 35.5 mbsf.

### Hole C0013E

Hole C0013E was cored in the guide base at 27°47.4157'N, 126°53.8546'E on 12 September 2010 (Fig. F2). An 8.5 m advance below seafloor produced 6.08 m of very gassy (burp!) core. To avoid melting the core liner, we tried shooting Core 331-C0013E-2H as HPCS without any liner at all. Recovery was 1.21 m from what may have been a 5.5 m advance, with no indication of the system actually firing. Sediment was pumped out into plastic half-liners on the rig floor.

Switching to the ESCS for Core 331-C0013E-3X resulted in just 17 cm of sediment in the coring shoe and an empty liner after a 3 m advance. The situation was similar for Core 331-C0013E-4X; a 3.3 m advance gave only 10 cm of sediment in the coring shoe. Because the first attempt at HPCS coring without a liner misfired and failed, Core 331-C0013E-5H was taken liner-free with the HPCS. A 7 m advance

gave 1.29 m of core, which blew out of the barrel when it was extruded hydraulically. We switched back to the ESCS in an attempt to improve core recovery, but Core 331-C0013E-6X came back with only 49 cm of hard sediment in the core catcher.

Core 331-C0013E-7L was taken on 13 September and was the first test of the Baker Hughes INTEQ (BHI) coring system. Using the BHI system requires a bottom-hole assembly (BHA) change and a pipe trip between each core, so this decision was made with a significant level of angst. All other coring methods had met their limit, however, either because of formation hardness or the high temperatures encountered. A 9.2 m advance with the BHI system required ~18 h operational time and yielded only 2.1 m core, suggesting the formation was still too soft for coring with a diamond-impregnated bit. We therefore switched to the ESCS, but we cored 9.8 m without recovery; poor recovery was likely due to a microbead bag blocking a valve. Thus, the decision was made to stop using microbeads for the ESCS core barrel to avoid further core loss. The last core from Hole C0013E, Core 331-C0013E-9X, recovered only 0.25 m sediment from a 9.5 m ESCS advance, as well as some completely melted core liner. As all indications pointed to the fact that hot fluids were welling up the hole, we decided to end Hole C0013E at the penetrated depth of 54.5 mbsf.

### Casing and capping of Hole C0013E

At midday on 14 September 2010, the *Chikyu* moved to a nearby low-current area and prepared to drift and lower five joints of 5½ inch casing into Hole C0013E. The casing run started by evening, drifting the 9 nmi to Hole C0013E at 0.2–1.0 kt, with the casing lowered to 690 m drilling depth below seafloor (DSF). The hole was reentered on the morning of 15 September, and the casing was successfully hung from the guide base shortly after. By early afternoon, the ROV had landed the corrosion cap and we could observe vigorous fluid flow from the central stainless steel pipe mounted in the cap. It was time to move on to the next site (whew!).

### Hole C0013F

We returned to Site C0013 on 24 September 2010, after completing coring at Hole C0014G. The second visit was an attempt to collect cores using the aluminum liners that would survive the high temperatures at this site, which we obtained in Okinawa on 19 September. We had only three aluminum liners left at this point, having used the rest earlier in the month at Site C0014. The first core was shot 10 m southeast of the guide base, near Hole C0013C (Fig.

F2). The HPCS assembly was fired 2 m above seafloor, advancing 7.5 m into the sediment.

### Hole C0013G

After good recovery in Hole C0013E, the *Chikyu* moved to 10 m south of the guide base for Hole C0013G on 24 September 2010 (Fig. F2). We washed down to 7.5 mbsf in Hole C0013G and shot with the HPCS. We only advanced 1.8 m, to 9.3 mbsf, but with full recovery.

### Hole C0013H

Hole C0013H was spudded on 24 September 2010. High pressure was needed to fire the HPCS in the previous hole, so we picked up to above the seabed and circulated before entering Hole C0013H 2 m east of Hole C0013G (Fig. F2). Hole C0013H was washed down to 9.3 mbsf, where the HPCS was fired. Very high pressure was again needed before the shot went off, but we only advanced 0.6 m. Core recovery was 100%.

## Lithostratigraphy

Four lithostratigraphic units were identified at Site C0013, Iheya North hydrothermal field (Fig. F3; Table T2).

1. Unit I, the uppermost lithostratigraphic unit at Site C0013, comprises mud and grit with hydrothermally altered and mineralized material as major mineral components. It is 4–7 m thick, and its coarsest fraction contains as much as 50% detrital fragments of hydrothermal massive sulfide.
2. Unit II at Site C0013 is similar to Unit I, except that sediments are more consolidated and anhydrite breccia is present. The breccia consists of clasts of vein anhydrite with sulfide inclusions of sphalerite and pyrite. The thickness of Unit II varies from 6 to 8 m across Site C0013.
3. Unit III is similar to Unit II, but is differentiated by the presence of anhydrite nodules and reduced abundance of vein anhydrite. The thickness of Unit III varies from 7 to 10 m across Site C0013.
4. Unit IV comprises heavily silicified volcanoclastic rocks. It is encountered below ~26 mbsf in the bottom of Hole C0013D and to a depth of 45 mbsf in Hole C0013E. Recovery is very poor across this interval; thus, the lithological makeup of this unit is difficult to constrain.

Hydrothermal processes have significantly altered and/or replaced detrital siliciclastic and volcanic components in all units. We use the phrase “hydro-

thermally altered mud” to emphasize the importance of hydrothermal processes in controlling mineralogy, either by providing detrital components or by altering the primary mineralogy.

## Description of units

### Unit I

Intervals: Sections 331-C0013B-1T-1, 0 cm, to 1T-CC, 26 cm; 331-C0013C-1H-1, 0 cm, to 1H-5, 72 cm; 331-C0013D-1H-1, 0 cm, to 1H-3, 40 cm; 331-C0013E-1H-1, 0 cm, to 1H-5, 118 cm; 331-C0013F-1H-1, 0 cm, to 1H-8, 38 cm

Depths: Hole C0013B = 0–1.44 mbsf, Hole C0013C = 3.00–6.79 mbsf, Hole C0013D = 3.00–5.18 mbsf, Hole C0013E = 0–4.57 mbsf, Hole C0013F = 0–5.64 mbsf

Lithology: hydrothermally altered mud/clay, hydrothermal grit/gravel, and metalliferous detrital sulfide

Unit I comprises three main sediment types: hydrothermally altered mud, sand, and grit with unconsolidated medium- to coarse-grained hydrothermal sulfide lithoclasts. Within Holes C0013B and C0013E, hydrothermal clay is volumetrically subordinate to sand and grit. Grit predominates in Holes C0013C and C0013D, but top intervals were not cored in these holes, and thus the true thickness of mud is not represented. Coarser units occur irregularly (Fig. F4), and no correlations could be made between holes, indicating an irregular sedimentary architecture and interbedding of sediment types. The rapid lateral variation between holes at distances of <10 m, particularly in coarse sulfide content, suggests a proximal source for this material. This is difficult to reconcile with a source at the South Big Chimney Mound, some 100 m distant.

#### *Sediment types*

Hydrothermally altered mud and clay

The detrital clay size fraction has hydrothermally altered and detrital hydrothermal minerals as major sediment components. Sediment is unconsolidated.

Major mineral phases determined by X-ray diffraction (XRD) are kaolinite, illite, and barite. Accessory components include illite; detrital muscovite, some as small mica books 2–5 mm thick; angular quartz silt; detrital sphalerite and pyrite grains as large as 1 mm; disseminated wurtzite, sphalerite, pyrite, and galena; anhydrite, including euhedral anhydrite crystals; and acicular and partially devitrified volcanic spicules.

Hydrothermal grit/gravel

Grit or gravel layers contain discrete mineral grains and hydrothermal vein fragments or hydrothermal lithoclasts as major components. Detrital hydrothermal grains tend to be poorly sorted. Accessory components include quartz silt; discrete grains of wurtzite, sphalerite, pyrite, galena, and covellite; clasts of clear anhydrite veins with inclusions of galena and sphalerite; and opaque anhydrite, in some cases intergrown with talc and calcite.

Clasts of metalliferous detrital sulfide

Clasts of metalliferous detrital sulfide consist of sphalerite crystals intergrown with anhydrite and quartz, as well as discrete pyrite grains. Clasts are typically subrounded and irregularly spherical to oblate (Fig. F5A). With increasing textural maturity, the size of the sulfide grains decreases and their sphericity increases because of abrasion. Abrasion preferentially erodes sulfide in fragments with siliceous gangue, increasing their quartz volume fraction, as shown in Figure F5C. However, secondary euhedral anhydrite overgrowths are present on many sulfide-rich gravel and grit clasts (Fig. F5B).

### Unit II

Intervals: Sections 331-C0013C-1H-6, 0 cm, to 1H-CC, 30 cm; 331-C0013D-1H-3, 40 cm, to 2H-1, 40 cm; 331-C0013E-1H-5, 118 cm, to 4X-CC, 4 cm; 331-C0013F-1H-8, 38 cm, to 1H-CC, 62 cm

Depths: Hole C0013C = 6.79–12.51 mbsf, Hole C0013D = 5.18–12.90 mbsf, Hole C0013E = 4.57–12.74 mbsf, Hole C0013F = 5.64–7.50 mbsf

Lithology: hydrothermally altered mud, detrital metalliferous sulfide, and anhydrite breccia

Unit II consists of hydrothermally altered mud with some heavily veined intervals, as well as coarser lithologies containing anhydrite and detrital metalliferous massive sulfide lithoclasts.

#### *Sediment types and lithotypes*

Hydrothermally altered mud

The mud is pale gray with intense mottling and is often indurated. The detrital clay size fraction has hydrothermally altered or hydrothermal minerals as major components. Major minerals determined by XRD are kaolinite, illite, and anhydrite. Accessory minerals and components include discrete sulfide veins as wide as 1 mm (pyrite, sphalerite, and infrequent galena), vein anhydrite with sulfide mineralization, euhedral anhydrite crystals up to 2 mm in size, barite (detected by XRD only), fine acicular par-

tially devitrified volcanic glass spicules, and lithoclasts of hydrothermal sulfide.

#### Detrital metalliferous sulfide deposits

The detrital metalliferous sulfide deposits consist of poorly sorted detrital sulfide grains (see below). Layers are thin and generally in the grit- or sand-size fractions in Unit II (in Unit I they are coarser). Thin black bands containing sulfide mineral sand were also noted but were not logged as individual units. Components include angular quartz silt; aggregate detrital sulfide grains and discrete grains of wurtzite, sphalerite, pyrite, galena, and covellite; and clasts of clear vein anhydrite with inclusions of galena and sphalerite.

#### Clast- or matrix-supported anhydrite breccia

This lithotype comprises matrix- to clast-supported breccias with clasts of clear or white anhydrite (Fig. F6) in soft pale gray hydrothermal clay. Many are euhedral crystal fragments, up to 2 cm in size, and clearly formed in veins; others are more rounded but still an approximate euhedral form. Intervals with abundant euhedral anhydrite crystals exhibiting jigsaw fit, observed particularly well in X-ray computed tomography (CT) images, are interpreted as coarse veins fractured by drilling. A progression in clast shape can be seen from clear veins with inclusions of sulfide minerals (pyrite and sphalerite) to rounded anhydrite clasts that are opaque (Fig. F7).

### Unit III

Intervals: Sections 331-C0013D-2H-1, 40 cm, to 3T-CC, 45 cm; 331-C0013E-5H-1, 0 cm, to 6X-CC, 21 cm

Depths: Hole C0013D = 12.90–22.79 mbsf, Hole C0013E = 16.00–23.21 mbsf

Lithology: hydrothermally altered mud and anhydrite nodules

Unit III comprises hydrothermally altered mud with layers rich in nodular anhydrite. It is distinguished from Unit II by the presence of large polycrystalline anhydrite nodules and reduced abundances of clear vein anhydrite. Nodular anhydrite horizons were encountered in Holes C0013C and C0013D at similar depths, suggesting formation at a common depth or via a common sedimentary mechanism.

#### *Sediment types and lithotypes*

##### Hydrothermally altered mud

The mud is pale gray with intense mottling and is generally indurated. The detrital clay size fraction has alteration minerals as major components. Major minerals as determined by XRD are anhydrite, illite, and Mg chlorite. Minor talc is also present. Accessory minerals include sulfide minerals as discrete veins up

to 1 mm in width (pyrite, sphalerite, and infrequent galena), euhedral anhydrite crystals up to 2 mm in length, and coarse euhedral vein anhydrite, partially replaced by sulfide minerals.

##### Nodular anhydrite horizons

The nodular anhydrite horizons are similar to hydrothermal mud layers but contain white, opaque anhydrite nodules up to 5 cm in diameter (Fig. F8). The dominant component is always anhydrite, but minor dolomite, calcite, quartz, and talc, as well as 1%–2% fine-grained disseminated sphalerite and pyrite, are also typically present. Nodules commonly exhibit complex internal zonation, including coarsely crystalline veining, and many show pitted surfaces and truncation of internal zonation—clear evidence of erosion following precipitation.

### Unit IV

Intervals: Sections 331-C0013D-4X-1, 0 cm, to 4X-CC, 42.5 cm; 331-C0013E-6X-CC, 21 cm, to 9X-CC, 6.5 cm

Depths: Hole C0013D = 26.00–26.53 mbsf, Hole C0013E = 23.21–45.24 mbsf

Lithology: volcanic breccia

In Hole C0013E, Unit IV comprises silicified volcanic breccia from 23 mbsf (Section 331-C0013E-6X-CC, 8 cm) to 45 mbsf (interval 9X-1, 0–49 cm); it was also encountered at the base of Hole C0013D at 26 mbsf (Sections 331-C0013D-4X-1, 0 cm, to 4X-CC, 42.5 cm). Although described here as single unit, additional geochemical analysis of volcanic clast types and thin section description may further help subdivide the unit. A greater variety of clast types was encountered in Hole C0013E than in Hole C0013D, in which we only encountered a single silicified volcanic breccia horizon.

Resedimented clasts of volcanic breccia predominate as the main clast type, and both monomictic and polymictic types are present (Fig. F9). All lithoclasts are now matrix supported and cemented by quartz (in interval 331-C0013D-4H-1, 0–2 cm) and quartz ± anhydrite (from Core 6H through Section 9H-CC). Other volcanic components in the breccia include clasts of pumiceous to vesicular flow-banded lavas. The major mineral in all cases is quartz, which may be coarsely crystalline or fine grained, accompanied by Mg chlorite, muscovite, and illite. Domains of volcanic glass are commonly well preserved (Fig. F10). Clay minerals replace other primary volcanic phases such as muscovite. Correlation of individual volcanoclastic lithologies from hole to hole was not practical because Unit IV was only encountered in the deepest parts of Holes C0013E and C0013D. However, it is notable that at Site C0014, substantial

thicknesses of hydrothermally altered mud stratigraphically separate intervals dominated by volcanoclastic lithologies at 26–30 mbsf (Holes C0014B and C0014G), 54 to ~60 mbsf, and 126 mbsf (Hole C0014G). Hence, it is possible that distinct stratigraphic horizons are present and could be correlated on the basis of elemental composition between the two sites.

### Grain size distribution

Seven sediment samples, ranging in depth from 0.54 to 4.92 mbsf, were selected from Hole C0013F for grain size measurement; data are summarized in Table T3 and Figure F11. It should be noted that this sample set is sourced entirely from Unit I and is not representative of the drilled interval at Site C0013. The mean grain size of the measured sediments shows large variation downcore, ranging from  $7.13\Phi$  to  $2.89\Phi$  (7 to 135  $\mu\text{m}$ ). Clay fractions in the sediment samples are mostly <10%, whereas sand fractions are mostly >40%. According to the grain size classification of Folk and Ward (1957), five of the measured sediment samples are silty sand and only two samples are sandy silt (Fig. F12).

Grain size data indicate that most of the sediments are poorly sorted to very poorly sorted, with the standard deviation ranging from  $1.33\Phi$  to  $2.68\Phi$ . Skewness data suggest that only one sample (331-C0013F-1H-5, 15–16 cm) is coarse skewed and the others are all very fine skewed. Measured samples show platykurtic and leptokurtic to mesokurtic kurtosis according to classification by Blott and Pye (2001). Interestingly, two fine-grained samples (331-C0013F-1H-2, 45–46 cm, and 1H-5, 15–16 cm) show distinctly different distribution patterns when compared with the five coarser samples (Fig. F13), probably indicating different sedimentary provenance.

### Interpretation

At Site C0013, sediment lithologies are dominated by hydrothermal activity, either by in situ formation of hydrothermal minerals or through resedimentation of local hydrothermal deposits. Notable are the anhydrite-rich units, as anhydrite is undersaturated in cold seawater and thus dissolves. The presence of substantial anhydrite- and magnesium-rich clay horizons is evidence for subsurface temperatures greater than ~150°C. Were temperatures cooler than this for prolonged periods of time, anhydrite would not persist.

Clay and sulfate minerals predominate in the lithologies found at Site C0013. These minerals display replacement textures in hand specimen and under the binocular microscope, and/or they have hydrother-

mal associations in terms of their genesis. Key minerals include Mg chlorite and talc.

The hydrothermally altered sediments at Site C0013 likely sequester large quantities of sulfate and magnesium from interstitial water. The source of dissolved Mg cannot be hydrothermal fluids, as acidic rocks such as rhyolite are magnesium poor, especially in pumice (Kato, 1987), and high-temperature hydrothermal fluids are depleted in Mg in any case. Both sulfate and Mg doubtless derive from seawater, which is a major component of the fluids that have altered the sediment at Site C0013.

Pumice is a common seafloor sediment in the vicinity of knolls and seamounts in the middle Okinawa Trough area and is abundant within sedimentary sequences at other sites drilled during IODP Expedition 331. These pumices often contain parallel tube-like vesicles (Kato et al., 1987). Recent studies infer that tube pumice is formed in subaqueous eruptions at 500–1000 m water depth when seawater that is rapidly imbibed into the elongated vesicles reduces clast density and inhibits floating (Allen et al., 2010). According to this model, the pumiceous clasts accumulated by volcanic debris flows must originate from nearby seamounts, as they are buoyant for only a short time. It is reasonable to expect abundant pumice sedimentation at Site C0013 because it is located within the volcanic complex. Little if any pumice persists in the hydrothermally altered sediment at Site C0013. The relative rarity of pumice at Site C0013 is interpreted to be due to its destruction during intense hydrothermal alteration.

## Biostratigraphy

Core catcher material from Site C0013 was processed for micropaleontological examination (Table T4). Samples consist of clay clasts (often producing a relatively large, fine-grained [ $<63 \mu\text{m}$ ] sample of clay) and anhydrite, with smaller amounts of various sulfide minerals (euhedral pyrite > sphalerite > galena). Microfossils were not observed in any of these samples using light or electron microscopy.

Samples that possessed a higher proportion of base metal sulfides were observed at 9.5 mbsf (millimeter-scale sphalerite), 12.6 mbsf, and 12.8 mbsf (1–5 mm sphalerite). Material was examined using scanning electron microscopy for mineralogical identification, as reported in “[Petrology](#).”

## Petrology

As was noted in “[Lithostratigraphy](#),” pervasive hydrothermal alteration and sulfide mineralization are

ubiquitous in material recovered from Site C0013, which was targeted at a high-heat flow site ~0.1 km east of the main high-temperature chimneys of the Iheya North hydrothermal field (Takai et al., 2010). Following the failure of Hole C0013A, Holes C0013B (cored interval 0.0–9.5 mbsf), C0013C (cored interval 3.0–12.7 mbsf), and C0013D (cored interval 3.0–35.8 mbsf) were drilled within 5 m of each other along an approximate north–south line (Fig. F2). Hole C0013E, which utilized the drilling guide base, was spudded ~10 m west and 2 m upslope from the other three holes and cored from 0.0 to 54.5 mbsf. On returning to the site, Holes C0013F (cored interval 0.0–7.5 mbsf), C0013G (cored interval 7.5–9.3 mbsf), and C0013H (cored interval 9.3–9.9 mbsf) were drilled between Hole C0013E and the other holes. Given the close proximity of the holes, they can effectively be considered to represent a single drilled section for the purposes of petrological interpretation. Holes C0013G and C0013H recovered only drill-washed material and therefore provide no useful petrological information.

The following description of hydrothermal alteration and mineralization from Site C0013 is based primarily on visual descriptions of cores from Holes C0013B–C0013F and is supplemented by XRD analyses of representative samples, scanning electron microscope (SEM) imaging, and energy dispersive spectrometry (EDS) characterization of selected samples, along with a small number of polished thin section descriptions of more competent lithologies. Most of the rocks drilled at the site are composed of very fine grained material. With the exception of anhydrite, quartz, sulfide minerals, and native sulfur, most mineralogical determinations were made or confirmed using the results of XRD analysis. This is particularly true of Mg chlorite, talc, kaolinite, and muscovite within the altered sequence.

Difficulties encountered in drilling at the site (melted core liners and variable ground conditions leading to badly disturbed core, broken core, and patchy recovery), when coupled with the large number of whole-round samples removed from the core prior to lithological description, make it difficult to interpret the temporal and spatial relationships between alteration and mineralization styles observed in the core, except at the grossest level.

### Overview of hydrothermal alteration and mineralization at Site C0013

Hydrothermal alteration and mineralization at Site C0013 may be spatially divided into five assemblages, which exhibit a broadly consistent vertical distribution from the seafloor (Fig. F14):

1. From 0 to ~4 mbsf, generally moderately hydrothermally altered, variably sulfidic sediment is characterized by detrital sulfide (sphalerite-pyrite-covellite)–sulfate (anhydrite-barite) mineralization and local development of native sulfur, as well as the presence of kaolinite and muscovite.
2. Pale gray “hydrothermal clay” that features kaolinite and muscovite as well as anhydrite is best developed in Holes C0013C and C0013D, where it extends from ~4 to 6.5 mbsf. In Hole C0013E, it extends from 4 to 5 mbsf, and in Hole C0013F, from 4 to 5.5 mbsf.
3. A zone of pale bluish-gray to white mottled “hydrothermal clay,” featuring Mg chlorite as well as coarse (typically 4–5 cm) rounded nodules and brecciated, drilling-disturbed veins of white opaque anhydrite ± dolomite ± talc ± calcite ± quartz ± sphalerite ± pyrite underlies the kaolinite-muscovite-bearing alteration and extends to at least 23 mbsf in Holes C0013D and C0013E. Below this depth, recovery becomes too poor to confirm the presence of the assemblage. Fine-grained disseminated pyrite and sphalerite are present in low abundances (typically <<1%) throughout the zone, and rare narrow irregular anhydrite-sulfide and quartz-sulfide veins are also observed.
4. Recovery from below ~26 mbsf in Holes C0013C and C0013D, the two deepest holes at the site, consists of hard quartz and Mg chlorite–altered volcanic breccia with scattered quartz-sulfide (sphalerite-pyrite ± covellite ± native copper) veining and trace fine disseminated pyrite within clasts. This material is interpreted to be volcanic basement. The base of this unit is not well defined, as recovery from the lower portions of both Holes C0013C and C0013D is poor, although material recovered from Core 331-C0013E-9X was curated at a depth of 45 mbsf.
5. An interval featuring abundant euhedral anhydrite crystals, 1–2 cm in length, interpreted to be veins dismembered by drilling, overlaps the kaolinite and Mg chlorite-bearing alteration zones between ~4 and 5 mbsf and 9 and 10 mbsf. These veins are interpreted to overprint the other alteration at the site.

### Near-surface sulfidic sediment

Variably sulfidic sediment was intersected in the upper portion of all five successful holes drilled at Site C0013 and is best represented in Sections 331-C0013E-1H-1 through 1H-5 (0.0–4.6 mbsf). Even with the limited drilling available from the seafloor

at the site (only Holes C0013B, C0013E, and C0013F attempted to core the interval from 0 to 3 mbsf), it is apparent that this material shows rapid lateral and vertical variation in composition and grain size, suggesting that the sediment originated locally.

Sand- to grit-sized anhydrite crystal fragments and less abundant barite are present throughout the interval, as are 0.5–3 mm euhedral and subhedral fragments of sphalerite, pyrite, and, at significantly lower abundance, covellite. Galena and sulfosalts, including tetrahedrite-tennantite, are also detected by SEM as intergrowths with sphalerite. The sulfide-sulfate assemblage is reminiscent of the mineralogy of sulfide chimneys and mounds at Iheya North Knoll (Glasby and Notsu, 2003) and is interpreted to be sediment derived from the breakdown of nearby hydrothermal mounds. In Hole C0013E, the section from 0.16 to 4.1 mbsf averages >10% sulfide (visually estimated), with some layers as thick as 11 cm exceeding 50% total sulfide. The near-surface sequence is less heavily mineralized in the other holes drilled, although sulfide content locally exceeds 10% (visually estimated) over some intervals.

A distinctive yellow native sulfur-bearing horizon was also intersected in the uppermost 7.5 cm of Hole C0013E (Fig. F15A). This material contains fragments of quartz-altered volcanic rock, along with minor sphalerite and barite cemented in native sulfur. It is interpreted to represent sediment that has been infiltrated by liquid native sulfur on or close to the seafloor. Native sulfur melts at temperatures between 112° and 119°C at 1 atm (Haynes, 2010), implying that a similar temperature existed near the seafloor at the time this horizon formed. Native sulfur is also abundant in the sulfidic sediment at the top of Hole C0013F, occurring as a cement, similar to that seen in Hole C0013E, both at the top of the hole and as crystalline 1–3 mm linings on what must have been gaseous or fluid-filled voids in silty mud (Fig. F15B). Native sulfur is present to 0.7 mbsf, implying that it precipitated from H<sub>2</sub>S-rich fluid as it passed through the sediment.

XRD analysis of samples from within the sulfidic sediment detected minor quantities of kaolinite and muscovite, in addition to the phases noted above (Table T5).

SEM imaging of anhydrite from the sulfidic sediment shows evidence of incipient dissolution and replacement by gypsum (Fig. F16), implying that current temperatures in parts of the material are below ~40°C, the temperature below which anhydrite transforms to gypsum (MacDonald, 1953). Framboidal pyrite (Fig. F17), partially devitrified volcanic glass (Fig. F18), and opaline silica (Fig. F19) are also

observed by SEM, providing additional evidence that relatively low temperature conditions are locally present. However, the widespread presence of anhydrite crystal fragments within the sequence implies that temperatures of close to 150°C were prevalent (see “**Coarsely crystalline anhydrite veining**,” below).

### Kaolinite-muscovite alteration

Kaolinite-muscovite-anhydrite-bearing “hydrothermal clay” is typically pale gray to white. In drill core, the assemblage is massive in character, except when overprinted by coarsely crystalline euhedral anhydrite veining. In addition to kaolinite and muscovite, vermiculite may also be present (suggested by XRD). It is also considered likely that cryptocrystalline clays are present in the samples, although this will need to be confirmed through postexpedition research. Fine-grained disseminated pyrite is present throughout the alteration zone in low abundances (typically <<1%).

In detail, kaolinite-muscovite-bearing alteration is interlayered with more sulfidic horizons. This is not surprising, as ongoing alteration of footwall material would be expected in an actively discharging hydrothermal system during successive pulses of strong hydrothermal activity.

### Mottled Mg chlorite and nodular anhydrite alteration

Mg chlorite + anhydrite alteration is observed from ~6 to 12.5 mbsf in Hole C0013C (bottom of hole), from ~6 to 23 mbsf in Hole C0013D, from ~5 to 23 mbsf in Hole C0013E, and from ~5.5 to 9 mbsf in Hole C0013F (bottom of hole). The assemblage is distinguished visually by a distinct bluish-gray color and the presence of coarse (typically 4–5 cm), white, opaque, hard, rounded nodules and brecciated, drilling-disturbed intervals (possible veins) of anhydrite (Fig. F20). In many cases, anhydrite nodules also contain lesser amounts of one or more of dolomite, calcite, quartz, or talc and 1%–2% fine-grained sphalerite and pyrite. Fine-grained disseminated pyrite and sphalerite are present in low abundances (typically <<1%) throughout the zone, and rare narrow irregular anhydrite-sulfide and quartz-sulfide veins are also observed.

Many anhydrite nodules within the mottled alteration zone show pitted surfaces and truncation of internal zonation—clear evidence of erosion following precipitation (Fig. F20). This evidence indicates that the nodules have been either transported to their present location or precipitated and then chemically eroded during the evolution of the hydrothermal

system at Site C0013. It is not possible to distinguish between these two possibilities with the information available from the site to date, but either possibility implies that the nodular anhydrite is the earliest alteration event detected at Site C0013.

### Quartz + Mg chlorite–altered volcanic basement

Material recovered from below ~26 mbsf at Site C0013 consists of moderately to highly quartz + Mg chlorite–altered volcanoclastic breccia and conglomerates, interpreted to be volcanic basement. These rocks are best represented in Core 331-C0013E-7L but were also recovered in Cores 331-C0013E-6X and 331-C0013E-9X, as well as Core 331-C0013D-4X.

The variation in volcanic texture of these rocks is discussed in “**Lithostratigraphy.**” The rocks are distinguished by their high hardness and distinct quartz stockwork veining (Fig. F21). Thin section examination reveals that ~40% of the rock remains as volcanic glass, with the remainder devitrified and replaced by quartz, chlorite, and minor biotite (Fig. F22).

Sulfide mineralization is scarce in the altered volcanic rocks, mostly limited to very fine grained disseminated pyrite euhedra scattered in trace quantities throughout. Most quartz veins are barren of mineralization. However, a handful of mineralized quartz-sulfide veins were noted in the intervals intersected and were observed to contain sphalerite, pyrite, covellite, and, in one interval, somewhat unexpectedly, fine intergrowths of native copper and organic carbon (Fig. F23).

### Coarsely crystalline anhydrite veining

Coarsely crystalline euhedral anhydrite was intersected in Hole C0013C from ~5.5 to 9.0 mbsf, in Hole C0013D from ~4.0 to 12.0 mbsf, in Hole C0013E from ~4.5 to 11.5 mbsf, and in Hole C0013F from ~5.5 to 8.8 mbsf (bottom of hole) (Fig. F14). Although logged in drill core as “hydrothermal gravel” with a clay matrix, it is probable that the anhydrite crystals, which typically are between 1 and 2 cm in length, represent a vein network that has been heavily fragmented by drilling.

Anhydrite becomes insoluble in seawater at temperatures >150°C (Bischoff and Seyfried, 1978), requiring that downwelling seawater would precipitate anhydrite at or around the 150°C isotherm. The concentration of coarsely crystalline anhydrite across a relatively narrow depth interval at Site C0013 implies precipitation by this means. The coarsely crystalline

anhydrite zone overlaps the transition, confirmed by XRD, from muscovite-kaolinite to Mg chlorite–dominated “clay” alteration at Site C0013, which occurs at ~6 mbsf in Holes C0013C, C0013D, and C0013F and at ~5 mbsf in C0013E. The presence of anhydrite veins across both alteration zones implies that the veins are unrelated to these alteration assemblages and represent a later overprinting event.

### Significance of the transition in “clay” mineralogy

The transition from kaolinite-muscovite–rich to chlorite-rich rocks with increasing depth at Site C0013 is similar to the gradation from paragonitized to chloritized rocks that is documented for the basement underneath the Trans-Atlantic Geotraverse hydrothermal mound at the Mid-Atlantic Ridge (26°N) (Humphris et al., 1995). The difference in mineralogy between Iheya North Knoll and the Mid-Atlantic Ridge is partially explained by the lack of iron and the abundance of potassium available within the sequence at the site when compared with the mafic volcanic rocks of the mid-ocean-ridge setting.

The change in alteration mineralogy is consistent with the generally accepted compositional evolution of upwelling hydrothermal fluids in seawater-dominated submarine systems. Along the fluid flow path in a hydrothermal convection cell, it can be anticipated that Mg fixation in chlorite leads to a decrease in fluid pH, leading in turn to an increase in fluid K content, which should stabilize potassic phases such as muscovite and kaolinite in the shallower parts of a felsic-hosted system (Seyfried et al., 1999).

In their study of hydrothermal clay alteration associated with high-temperature discharge and sulfide mineralization at the Jade hydrothermal field, Izena Caldera, also in the Okinawa Trough, Marumo and Hattori (1999) report a similar vertical transition from Mg chlorite at depth to near-surface kaolinite and native sulfur. They interpret this variation to reflect variable amounts of cold seawater incorporated into hot hydrothermal fluids in subseafloor sediments and tuff. They note, however, that mixing alone cannot generate sufficiently low fluid pH to explain the abundance of kaolinite minerals at the Jade hydrothermal field. They infer that low pH values are attained through oxidation of H<sub>2</sub>S dissolved in the hydrothermal fluid or released from the fluid during decompression. We propose a similar model for Site C0013, supported by the high H<sub>2</sub>S values recorded for many of the cores recovered at the site. In this model, the Mg chlorite–dominated alteration observed from 5 to 6 mbsf at Site C0013 and the less

intense kaolinite-muscovite alteration appear to be part of a single alteration event, produced by the chemical evolution of upwelling high-temperature hydrothermal fluid. Therefore, at the time at which this alteration formed, Site C0013 was likely a site of hydrothermal discharge.

Accurate temperature estimation based on phyllosilicate and clay mineralogy in active hydrothermal systems is notoriously difficult (see for example, the discussion in Binns et al., 2007), as mineral stability is strongly influenced by fluid chemistry (which may vary rapidly, both temporally and spatially), rock composition, and confining pressure, and in many cases samples are in disequilibrium, limiting the use of many experimental studies. Although kaolinite may be stable at temperatures of up to ~290°C (Hurst and Kunkle, 1985) its stability field broadens with decreasing temperature, and it is most commonly found associated with lower temperature (~150°C) hydrothermal activity (Marumo, 1989). The predominance of Mg chlorite below ~6 mbsf at Site C0013 suggests alteration temperatures in the range of ~220°–300°C through this interval (Browne, 1978; Árkai, 2002).

### Relative timing of alteration and mineralization at Site C0013

Based on the limited drilling at Site C0013, the following sequence is inferred for the evolution of hydrothermal activity, summarized schematically in Figure F24:

1. The earliest alteration event preserved is represented by the white anhydrite ± dolomite ± talc ± calcite ± quartz ± sphalerite ± pyrite nodules and veins. As was noted above, this material shows evidence of either mechanical or chemical erosion, implying that it predates the pervasive alteration that affects the drilled sequence at the site. It is possible that this early anhydrite was initially formed by a very similar mechanism to that proposed for the coarsely crystalline anhydrite veins that are also seen (see below).
2. As discussed above, quartz + Mg chlorite alteration of volcanic basement, pervasive Mg chlorite alteration of sediment, and near-surface kaolinite-muscovite alteration are interpreted to be part of a single alteration event in a discharging hydrothermal system. This event is the second phase of alteration recorded at Site C0013. Variably sulfidic sediments at the top of the sequence are interpreted to represent the eroded
3. As was discussed previously, it is likely that the coarse-grained crystalline anhydrite veining was formed by heating of downwelling seawater to a temperature >150°C. Given the disturbed nature of much of the core recovered at the site, clear textural relationships are not observed. However, it is likely that this alteration event postdates the other hydrothermal alteration and records a recent influx of seawater into the system after discharge at the site ceased.

## Geochemistry

### Interstitial water

A total of 26 whole-round samples were processed at Site C0013 from five different holes. Routine samples were collected immediately above and/or below whole rounds dedicated for microbiology, usually at a frequency of one to two samples per 1.5 m section. We squeezed whole rounds at the laboratory temperature of ~20°C rather than at in situ temperature, as in situ temperatures varied from the ~4.5°–4.9°C of ocean bottom water in the Okinawa Trough to >150°C, as inferred from alteration mineral assemblages in the cores and the fact that the plastic core liners we used deformed and melted at depths below ~10–15 mbsf. We squeezed three samples from Hole C0013E that yielded no water (Table T6). Our deepest sample, from Core 331-C0013E-5H at 17 mbsf, was collected by piston coring without a liner; recovery in this core was only ~20%, and the rest of the core may have been washed away. Nonetheless, this sample appears to be sound based on its chemical composition.

Holes C0013B and C0013D were drilled within 3 m of each other. Hole C0013B sampled only shallow depths, yielding three samples from 0.5 to 1.3 mbsf, whereas Hole C0013D sampled a deeper interval, yielding eleven samples from 3.0 to 7.6 mbsf. For some elements, these two holes appear similar. By contrast, Hole C0013E, which lies ~8 m to the northwest, yielded four samples from 0.3 to 17 mbsf and is compositionally quite different from Holes C0013B and C0013D. Hole C0013F is more similar to Hole C0013E than to the others. Hole C0013G, for which there is only a single sample, is difficult to group (Table T6). These holes are thus compositionally quite variable. We infer that the variability stems from at least two competing processes that govern the chemistry of this region: (1) the dissolution of anhydrite

during recovery and processing of the core samples and (2) the influence of hydrothermal fluid migration within the sediment column.

### Major elements

Chloride, the major anion in seawater, is nearly constant with depth in Holes C0013B and C0013D at the concentration in seawater, except for two samples with concentrations as much as 5% higher at ~6 mbsf (Fig. F25). In Hole C0013E, however, Cl varies from ~34% lower than seawater to ~12% higher in the deepest sample from 17 mbsf. The deepest sample from Hole C0013F, at 5.7 mbsf, is depleted in Cl relative to seawater, as is the single sample from Hole C0013G at 8.7 mbsf. Bromide generally follows the same pattern as Cl (Fig. F25). As the major cation in seawater, Na (Fig. F26) generally follows Cl, as expected from the charge balance constraint. Na calculated from charge balance generally agrees with Na measured by ion chromatography, with a few exceptions (Table T6). The Na/Cl ratio is higher than in seawater for three shallow samples from Hole C0013B, probably because of expulsion of Na from ion exchange sites in clay minerals by other cations, but these ratios decrease steeply with depth to values lower than in seawater in all the other holes, showing that Na is being removed from the seawater-derived pore water into alteration minerals over this interval and at greater depths. The other alkali elements, K (Fig. F26), Rb, Cs (Fig. F27), and Li (Fig. F28), increase slightly with depth near the bottom of Hole C0013D and greatly in Hole C0013E to concentrations that are quite enriched for a seafloor hydrothermal system. These high concentrations are reached because felsic volcanic rocks are richer in alkali elements than are mid-ocean-ridge basalts. Boron and silicon likewise exhibit large enrichments (Fig. F28), consistent with the influence of high-temperature fluid.

Mg increases with depth in Holes C0013B and C0013D and to a lesser extent in Hole C0013F (Fig. F26), probably because of ion exchange with clays, as for Na, but decreases to only 7 mM in Hole C0013E. A decrease with depth is expected, as Mg from seawater-derived solutions in seafloor hydrothermal systems is typically removed into smectite and mixed-layer clay minerals at low temperature and into chlorite (at  $\geq 230^\circ\text{C}$ ) and amphiboles (at  $\geq 280^\circ\text{C}$ ) at higher temperatures (Mottl, 1983). Ca increases irregularly with depth in all five holes (Fig. F26), to concentrations nearly five times that in seawater. Although some of this increase is typical for hydrothermal solutions, as Ca is typically leached from the host rock (Mottl, 1983), much of the in-

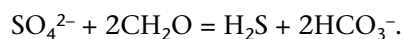
crease at Site C0013 is an artifact of anhydrite, which is abundant throughout the core and which certainly dissolved during the 3–25 h between the arrival of the core on deck and the squeezing of sediment to separate pore water. Dissolution of anhydrite can also be inferred from the large increases in sulfate, which reach concentrations more than three times that in seawater. The composite sum of Ca plus Mg for all samples from this site increases nearly linearly with sulfate (Fig. F29), as would be expected if anhydrite dissolution, followed by exchange of dissolved Ca for Mg in clay minerals in the core, is the major source of the alkaline earth elements and sulfate that we measured in solution. It could be argued from Figure F29 that the relationship between these cations and sulfate is different for each hole. Such differences in slope probably result from variability in hydrothermal fluid content and in the amount of anhydrite and clay at various depths from hole to hole. These variations, in turn, would produce variable rates of anhydrite dissolution and ion exchange of dissolved Ca for Mg and Na in clay minerals. By contrast to the holes with increasing sulfate, sulfate decreases with depth in Hole C0013F to less than a third the concentration in seawater, as would be expected from anhydrite precipitation within the hydrothermal system with increasing temperature (Mottl, 1983). Refractive index, which varies with salinity, reflects the sum of all of these changes in major element concentrations.

The deepest sample obtained from this site, from Hole C0013E at 17 mbsf, is in many ways a typical high-temperature solution from a seafloor hydrothermal system. Relative to seawater, it is slightly briny at 623 mM Cl; it has elevated Ca, K, Rb, Cs, B, and Si and depleted Mg and sulfate; and it has lost Na to the altered rocks. Although these characteristics are not surprising for hydrothermal systems (Mottl, 1983; Von Damm, 1995), both Cl and K (81 mM) concentrations are higher for this sample than those observed at the nearby Iheya North vents (e.g., Kawagucci et al., 2011). However, the Yonaguni IV system, which lies several hundred kilometers to the southwest, does contain comparable Cl and K concentrations (Suzuki et al., 2008). This deepest sample from Hole C0013E also differs from a typical mid-ocean-ridge hot spring in its high alkalinity (22 mM) and its high concentrations of the nutrient species ammonium, phosphate, and silicon, as discussed in the next section.

### Alkalinity and nutrients

Alkalinity increases irregularly with depth to a concentration >10 times that in seawater (Fig. F30),

probably because of oxidation of organic matter in the sediment approximated by the reaction



In basalt-hosted, sediment-free mid-ocean-ridge hydrothermal systems, alkalinity typically decreases to low and often negative values because of production of acidity accompanying Mg removal into alteration minerals (Mottl, 1983); that acidity is apparently being neutralized by reaction with sediment at Site C0013. Although we did not measure  $\text{H}_2\text{S}$  because the cores were purposely allowed to outgas for safety reasons, hydrogen sulfide was likely quite abundant in these cores, as evidenced by the high total sulfur in the sediment (Fig. F31) and the presence of sulfide minerals. Ammonium (Fig. F30) likewise increases with depth, as would be expected from the oxidation of organic matter. Phosphate is irregularly present at surprisingly high concentrations. It is possible that these nutrients have been introduced into these holes by lateral flow from Hole C0013A and subsequent holes, as these were drilled only 2–10 m away from each other and lateral flow has been inferred at Site C0013 from other data. As the holes were drilled within a few hours of each other, this lateral flow would have to have been relatively fast. Phosphate does not appear to be coupled to ammonium, and an especially phosphate-rich interval from 4.2 to 6.0 mbsf indicates that phosphate may be locally derived by mineral dissolution.

## Summary

Interstitial water at Site C0013 is clearly influenced by hydrothermal activity. This influence is apparent even though the pore water we analyzed has been greatly affected by dissolution of anhydrite during recovery and processing of the cores. The deepest sample from Hole C0013E likely represents the most pristine hydrothermal fluid recovered at this site, and it is noteworthy that its high K and Cl values reside at the higher end of the end-member fluid estimates that have previously been published for the nearby vents (e.g., Kawagucci et al., 2011).

## Headspace gas

Methane was detected in all samples at Site C0013 (Fig. F32). Concentrations increase with depth and reach hundreds of micromolar, peaking at ~10 mbsf before decreasing again with depth. Methane measured in safety gas (Table T7) and science gas samples (Table T8) exhibit similar trends, but concentrations from the heated safety gas vials are more scattered and about a factor of two higher. Ethane was observed in 6 of 16 safety gas samples, with concentra-

tions typically less than 1  $\mu\text{M}$ . Of these, only two showed evidence for propane and other higher hydrocarbons (Sections 331-C0013E-5H-1, shot with no core liner, and 7L-1, cored using the BHI hard rock system, which recovered rocks in this core). These two headspace samples also had low levels of butane, ethylene, and propylene, suggesting that all these gases resulted from the breakdown of larger organic molecules because of frictional heating during drilling. Although Site C0013 was one of the highest temperature sites we cored, none of the other 18 safety gas samples showed clear evidence for contamination. Figure F32 shows the observed methane to ethane ratio for samples with >400 ppm methane in the safety gas vial. In this figure, the sample with the lowest ratio is from Section 331-C0013E-5H-1, one of the samples that showed clear evidence for hydrocarbon contamination. The other samples show ratios >2000, with most >6000. A peak in methane combined with a consistently high methane-to-ethane ratio suggests biogenic hyperthermophilic methane production at this site, bounded above and below by zones of methane destruction and/or dilution.

Hydrogen was observed in 10 of the science gas samples from Holes C0013B–C0013E (Fig. F32). Its concentration increases logarithmically with depth, exceeding 200 nM at 12 mbsf and reaching micromolar concentrations at 20 mbsf. The logarithmic increase with depth suggests a deep hydrogen source and a relatively shallow  $\text{H}_2$  sink at ~10 mbsf. The sink could be methanogenesis and/or sulfate reduction. Significant hydrogen was observed in all science gas samples from Holes C0013F–C0013H. We suspect that this hydrogen is a consequence of using aluminum core liners during drilling.

## Sediment carbon, nitrogen, and sulfur composition

Calcium carbonate ( $\text{CaCO}_3$ ) content calculated from inorganic carbon concentration at Site C0013 is generally low, with most samples having <0.1 wt%  $\text{CaCO}_3$  (mean = 0.7 wt%). Only three samples have concentrations >1 wt% (Table T9; Fig. F33); one of these, Sample 331-C0013E-2H-CC, has 41.9 wt% and is likely anhydrite containing inclusions of calcite, dolomite, and talc, based on shipboard core descriptions (see “Lithostratigraphy”). Without these three samples, the mean  $\text{CaCO}_3$  concentration is 0.08 wt%.

For Holes C0013B–C0013E, total organic carbon (TOC) content ranges from below detection (<0.001 wt%) to 1.76 wt%. Six samples have TOC >1 wt%. Of concern is the fact that Holes C0013B–C0013E were

cored using plastic core liners, which melted at this site. Also of note, Section 331-C0013C-1H-1 has a TOC concentration of 1.2 wt%, but its total nitrogen (TN) content was too low to be detected. We were initially concerned that the low TN suggests the TOC derives from melted core liner. However, of the six samples with >1 wt% TOC, two are from Holes C0013F–C0013H, which were drilled using aluminum core liners. These two samples (at 5.8 and 9.6 mbsf) also have no detectable TN, indicating that some carbon-rich samples also have high C/N. Still, it remains likely that the melted core liners contributed a significant amount of organic carbon to some samples recovered from Holes C0013B–C0013E.

Beyond this observation, it is difficult to interpret the TOC and TN data except to state that sediments at Site C0013 are characterized by low organic carbon content. Excepting the two samples with TOC >1 wt% (at 5.8 and 9.6 mbsf), TOC in Holes C0013F–C0013H decreases with depth, from ~0.1 wt% in the uppermost few meters below seafloor to 0.01 wt% by 8 mbsf (Fig. F31). This trend suggests that hydrothermal alteration and possibly also microbial activity remineralize sedimentary organic carbon relatively quickly.

Total sulfur (TS) concentrations are generally high, ranging from 0.9 to 65.8 wt% (Table T9), reflecting the significant amount of sulfide and/or sulfate minerals observed throughout the sediments. TS decreases with depth (Fig. F31): all values >20 wt% are found in the uppermost 10 mbsf, and values >32 wt% are restricted to the uppermost 2 mbsf in Hole C0013E, where pyrite is abundant.

## Microbiology

### Total prokaryotic cell counts

The abundance of microbial cells in the subseafloor at Site C0013 was evaluated by fluorescent microscopy using SYBR Green I as a fluorochrome dye. Total cell biomass at Site C0013 is generally lower than the detection limit of our onboard counting method at this site of  $4.4 \times 10^6$  cells/mL sediment. Only one sample from 3.14 mbsf in Hole C0013D presented cell numbers greater than the detection limit, and this sample may have been contaminated by drilling fluid (Tables T10, T11). Microbial cell abundance even in the shallowest sediment at Site C0013 was lower than that at Sites C0015 and C0017. This result suggests that most of the core samples at Site C0013 were exposed to a higher temperature range than microbes can survive.

### Cultivation of thermophiles

Growth of *Thermococcales* (e.g., *Thermococcus*) at 80°C and *Aquificales* (e.g., *Persephonella*) and thermophilic *Epsilonproteobacteria* (e.g., *Nitratiruptor*) at 55°C was examined for all core samples from Site C0013. No growth was observed for any of the microorganisms tested.

### Cultivation of iron-oxidizing bacteria

Selected samples from Site C0013 were incubated in artificial seawater (ASW) media A and B for depths from 1.09 to 17.04 mbsf. Of these, only Sample 331-C0013B-1T-CC, 6–12 cm, showed significant growth (mainly in ASW media A). Contamination tests were not run for this sample, and the pristine sampling of the core catcher was questioned. In an attempt to answer the question of contamination, another sample (331-C0013F-1H-3, 43–58 cm) from approximately the same depth was inoculated when we returned to drill Hole C0013F. After a 4.5 day incubation period, this sample showed no growth in ASW media A. This result would suggest that the core catcher was indeed contaminated. Nevertheless, subsamples from Section 331-C0013B-1T-CC were stored for future analysis.

### Contamination test

Fluorescent microspheres were used to test for contamination in all the cores taken by the HPCS and the first core by the EPCS at Site C0013. Fewer microspheres were observed in the deeper cores from Site C0013 (Table T11). Considering that the plastic core liner often melted at Site C0013, the fluorescent microspheres might also melt in the deeper samples. The perfluorocarbon tracer (PFT) test was conducted only in Hole C0013F (Table T12).

### Conclusions

We expected to find microbiological evidence for an active subvent biosphere at Site C0013, but we found neither abundant microbial cells nor detectable growth of (hyper)thermophiles in the onboard measurements and experiments. We were not able to measure temperature in the subseafloor at Site C0013, but there is ample evidence from melting of the plastic core liners, alteration mineralogy and pore water chemistry, and direct observation of hydrothermal fluid emission during the drilling operation that Site C0013 has a steep thermal gradient. It appears that most of the subseafloor environment we sampled at this site has been exposed to tempera-

tures that exceed the habitable and survival limits of microorganisms.

## Physical properties

Physical property measurements were made at Site C0013 to nondestructively characterize lithostratigraphic units and states of sediment consolidation.

### Density and porosity

Bulk density was determined from both gamma ray attenuation (GRA) measurements on whole cores (with the multisensor core logger for whole-round samples [MSCL-W]) and moisture and density (MAD) measurements on discrete samples (see “[Physical properties](#)” in Expedition 331 Scientists, 2011b). A total of 64 discrete samples were analyzed for MAD (1, 15, 20, 15, 10, 2, and 1 samples from Holes C0013B, C0013C, C0013D, C0013E, C0013F, and C0013G, respectively). Wet bulk density is roughly constant with depth (Fig. [F34](#)), as determined by both MAD and GRA, although the latter values are generally lower than the former and exhibit more scatter. This is expected of GRA-derived density, as GRA is very sensitive to incompletely filled core liners and the presence of voids and cracks.

The average bulk density in Holes C0013C, C0013D, and C0013F is  $\sim 1.9$  g/cm<sup>3</sup>; a narrow higher density zone (2.5 g/cm<sup>3</sup>) exists between 8 and 9 mbsf in Holes C0013C and C0013D. In the uppermost 10 m of Hole C0013E, density is generally higher ( $\sim 2.4$  g/cm<sup>3</sup>), but at greater depth it is similar to that in Holes C0013C, C0013D, and C0013F. Bulk density measured in Holes C0013G and C0013H is slightly higher,  $\sim 2$ – $2.2$  g/cm<sup>3</sup>, and broadly consistent with other densities observed in the 8–12 mbsf range. Bulk density increases to values  $>2.5$  g/cm<sup>3</sup> below 22 mbsf in Holes C0013D and C0013E.

Porosity was calculated from MAD measurements. It is generally quite high (40%–60%) and decreases slightly with depth (Fig. [F35](#)), except within two intervals: between 8 and 9 mbsf in a high-density anhydrite-rich layer and at  $>22$  mbsf where volcanoclastic rock dominates. Porosity drops to  $\sim 20\%$  within both intervals.

Grain density was calculated from discrete MAD measurements and is also approximately constant with depth ( $\sim 2.7$ – $3.1$  g/cm<sup>3</sup>) (open symbols, Fig. [F36](#)), except at the top of Hole C0013E, where grain densities are higher ( $\sim 3.5$  g/cm<sup>3</sup>) in an interval that appears to have a higher fraction of dense sulfide minerals.

Density and porosity results from the seven holes at Site C0013 reveal a coherent pattern that describes

four clear lithological boundaries or units based on density. Bulk density in the uppermost Unit I (0 to  $\sim 5$  mbsf; see “[Lithostratigraphy](#)”) is relatively constant at  $1.7$ – $1.9$  g/cm<sup>3</sup> for most holes (Fig. [F36](#)), with the exception of Hole C0013E (and possibly Hole C0013B), where bulk densities are relatively high in surface sediments. Lithostratigraphic Unit II is a narrower zone of higher bulk density ( $\sim 2.5$  g/cm<sup>3</sup>) between  $\sim 5$  and 10 mbsf. Bulk densities found in Unit III (12 to  $\sim 26$  mbsf) are similar to those found in Unit I. Within Unit IV (depths  $>25$  mbsf), bulk density is also relatively high ( $\sim 2.5$ – $2.9$  g/cm<sup>3</sup>) and porosity decreases sharply from  $\sim 60\%$  to  $<20\%$  (Fig. [F36](#)). These density variations appear to reflect lithological variations, which range from predominantly hydrothermally altered mud with varying amounts of sulfidic material to more cemented anhydrite breccias ( $\sim 8$ – $10$  mbsf) and then to volcanoclastic breccia at depths  $>22$  mbsf.

### Density and porosity changes across lithological unit boundaries

At the Unit I/II boundary, bulk density increases and porosity decreases, consistent with a transition from a zone of water-rich hydrothermally altered mud to a more cemented anhydrite-rich layer. At the Unit II/III boundary, bulk density decreases and porosity increases; this boundary is coincident with the return to a less cemented mud-rich zone in Holes C0013C–C0013E. At the Unit III/IV boundary ( $\sim 22$  mbsf), bulk density increases sharply and is similar to grain density. Porosity decreases sharply as well. These changes are consistent with the transition from a water-rich anhydrite mud to a more compacted volcanoclastic breccia.

### Electrical resistivity (formation factor)

Formation factor is a measure of the connected pore space within sediment and is used to calculate the bulk sediment diffusion coefficient. Electrical impedance measurements were made at 38 depths (1, 2, 14, 9, 10, 1, and 1 measurements in Holes C0013B, C0013C, C0013D, C0013E, C0013F, C0013G, and C0013H, respectively). Formation factors calculated for Site C0013 generally range from  $\sim 4.9$  to 10 and are roughly constant with depth (Fig. [F37](#)). There is some indication that formation factor increases downcore in Holes C0013D and C0013E, but there is no clear pattern among the seven holes.

### Discrete *P*-wave velocity and anisotropy measurements

*P*-wave velocity and relative anisotropy were measured only on samples indurated enough to cut sam-

ple polyhedrons, which was rarely the case. *P*-wave velocity determined on discrete samples from between 20 and 25 mbsf in Holes C0013D and C0013E range from 3000 to 4000 m/s (data not shown).

### Thermal conductivity

Thermal conductivity was measured on whole-round cores. A total of 58 measurements were made (2, 19, 5, 19, 10, 2, and 1 measurement from Holes C0013B, C0013C, C0013D, C0013E, C0013F, C0013G, and C0013H, respectively). Values range from a low of ~0.5 W/(m·K) in Hole C0013C to high values of 3–6 W/(m·K) in Holes C0013D and C0013E (Fig. F38). The average thermal conductivity for all seven holes is  $2 \pm 1$  W/(m·K). Thermal conductivity is relatively constant with depth. It exhibits a loose and inverse correlation with porosity (Fig. F36). At the same time that porosity decreases, thermal conductivity increases as water is forced from void spaces because the thermal conductivity of grains is greater than that of the water. Narrow zones of higher thermal conductivity are also roughly coincident with peaks in MSCL-W *P*-wave velocity, where higher velocities should also correspond to regions comprising less porous and denser material (Fig. F36).

### MSCL-I and MSCL-C imaging

MSCL-derived core images and color analyses are presented in the visual core descriptions (VCDs).

### MSCL-W derived electrical resistivity

MSCL-W-based resistivity data for Site C0013 are generally constant and low (~1–2 Ωm), but there are regions of higher resistivity (5–30 and >100 Ωm) between ~7.5 and 12 mbsf in Holes C0013C and C0013D. At >27 mbsf in Hole C0013E, resistivity is quite high and ranges from 100 to 300 Ωm. There is no obvious relationship with the discrete measurements of formation factor (Fig. F39 versus Fig. F37).

## References

- Allen, S.R., Fiske, R.S., and Tamura, Y., 2010. Effects of water depth on pumice formation in submarine domes at Sumisu, Izu-Bonin arc, western Pacific. *Geology*, 38(5):391–394. doi:10.1130/G30500.1
- Árkai, P., 2002. Phyllosilicates in very low-grade metamorphism: transformation to micas. In Mottana, A., Sassi, F.P., Thompson, J.B., Jr., and Guggenheim, S. (Eds.), *Micas: Crystal Chemistry and Metamorphic Petrology*. Rev. Mineral. Geochem., 46(1):463–478. doi:10.2138/rmg.2002.46.11
- Bischoff, J.L., and Seyfried, W.E., 1978. Hydrothermal chemistry of seawater from 25°C to 350°C. *Am. J. Sci.*, 278(6):838–860. doi:10.2475/ajs.278.6.838
- Binns, R.A., Barriga, F.J.A.S., and Miller, D.J., 2007. Leg 193 synthesis: anatomy of an active felsic-hosted hydrothermal system, eastern Manus Basin, Papua New Guinea. In Barriga, F.J.A.S., Binns, R.A., Miller, D.J., and Herzig, P.M. (Eds.), *Proc. ODP, Sci. Results*, 193: College Station, TX (Ocean Drilling Program), 1–17. doi:10.2973/odp.proc.sr.193.201.2007
- Blott, S.J., and Pye, K., 2001. GRADISTAT: a grain size distribution and statistics package for the analysis of unconsolidated sediments. *Earth Surf. Processes Landforms*, 26(11):1237–1248. doi:10.1002/esp.261
- Browne, P.R.L., 1978. Hydrothermal alteration in active geothermal fields. *Annu. Rev. Earth Planet. Sci.*, 6:229–248. doi:10.1146/annurev.ea.06.050178.001305
- Expedition 331 Scientists, 2011a. Expedition 331 summary. In Takai, K., Mottl, M.J., Nielsen, S.H., and the Expedition 331 Scientists, *Proc. IODP*, 331: Tokyo (Integrated Ocean Drilling Program Management International, Inc.). doi:10.2204/iodp.proc.331.101.2011
- Expedition 331 Scientists, 2011b. Methods. In Takai, K., Mottl, M.J., Nielsen, S.H., and the Expedition 331 Scientists, *Proc. IODP*, 331: Tokyo (Integrated Ocean Drilling Program Management International, Inc.). doi:10.2204/iodp.proc.331.102.2011
- Folk, R.L., and Ward, W.C., 1957. Brazos River bar [Texas]: a study in the significance of grain size parameters. *J. Sediment. Res.*, 27(1):3–26. http://jsedres.sepmonline.org/cgi/content/abstract/27/1/3
- Glasby, G.P., and Notsu, K., 2003. Submarine hydrothermal mineralization in the Okinawa Trough, SW of Japan: an overview. *Ore Geol. Rev.*, 23(3–4):299–339. doi:10.1016/j.oregeorev.2003.07.001
- Haynes, W.M. (Ed.), 2010. *CRC Handbook of Chemistry and Physics* (91st ed.): Boca Raton, Florida (CRC Press)
- Humphris, S.E., Herzig, P.M., Miller, D.J., Alt, J.C., Becker, K., Brown, D., Brüggemann, G., Chiba, H., Fouquet, Y., Gemmell, J.B., Guerin, G., Hannington, M.D., Holm, N.G., Honnorez, J.J., Itturino, G.J., Knott, R., Ludwig, R., Nakamura, K., Petersen, S., Reysenbach, A.-L., Rona, P.A., Smith, S., Sturz, A.A., Tivey, M.K., and Zhao, X., 1995. The internal structure of an active sea-floor massive sulphide deposit. *Nature (London, U. K.)*, 377(6551):713–716. doi:10.1038/377713a0
- Hurst, V.J., and Kunkle, A.C., 1985. Dehydroxylation, rehydroxylation, and stability of kaolinite. *Clays Clay Miner.*, 33(1):1–14. doi:10.1346/CCMN.1985.0330101
- Kato, Y., 1987. Woody pumice generated with submarine eruption. *Chishitsugaku Zasshi*, 93:11–20.
- Kawagucci, S., Chiba, H., Ishibashi, J., Yamanaka, T., Toki, T., Muramatsu, Y., Ueno, Y., Makabe, A., Inoue, K., Yoshida, N., Nakagawa, S., Nunoura, T., Takai, K., Takahata, N., Sano, Y., Narita, T., Teranishi, G., Obata, H., and Gamo, T., 2011. Hydrothermal fluid geochemistry at the Iheya north field in the mid-Okinawa Trough: implication for origin of methane in seafloor fluid circulation systems. *Geochem. J.*, 45(2):109–124. http://www.terrapub.co.jp/journals/GJ/abstract/4502/45020109.html

- MacDonald, G.J.F., 1953. Anhydrite-gypsum equilibrium relationships. *Am. J. Sci.*, 251(12):884–898. doi:10.2475/ajs.251.12.884
- Marumo, K., and Hattori, K.H., 1999. Seafloor hydrothermal clay alteration at Jade in the back-arc Okinawa Trough: mineralogy, geochemistry, and isotope characteristics. *Geochim. Cosmochim. Acta*, 63(18):2785–2804. doi:10.1016/S0016-7037(99)00158-1
- Mottl, M.J., 1983. Metabasalts, axial hot springs, and the structure of hydrothermal systems at mid-ocean ridges. *Geol. Soc. Am. Bull.*, 94(2):161–180. doi:10.1130/0016-7606(1983)94<161:MAH-SAT>2.0.CO;2
- Seyfried, W.E., Jr., Ding, K., Berndt, M.E., and Chen, X., 1999. Experimental and theoretical controls on the composition of mid-ocean ridge hydrothermal fluids. *Rev. Econ. Geol.*, 8:181–200.
- Suzuki, R., Ishibashi, J.-I., Nakaseama, M., Konno, U., Tsunogai, U., Gena, K., and Chiba, H., 2008. Diverse range of mineralization induced by phase separation of hydrothermal fluid: case study of the Yonaguni Knoll IV hydrothermal field in the Okinawa Trough back-arc basin. *Resour. Geol.*, 58(3):267–288. doi:10.1111/j.1751-3928.2008.00061.x
- Takai, K., Mottl, M.J., and Nielson, S.H.H., 2010. Deep hot biosphere. *IODP Sci. Prosp.*, 331. doi:10.2204/iodp.sp.331.2010
- Von Damm, K.L., 1995. Controls on the chemistry and temporal variability of seafloor hydrothermal fluids. In Humphris, S.E., Zierenberg, R.A., Mullineaux, L.S., and Thomson, R.E. (Eds.), *Seafloor Hydrothermal Systems: Physical, Chemical, Biological, and Geological Interactions*. Geophys. Monogr., 91:222–247.

**Publication:** 4 October 2011

**MS 331-103**

**Figure F1.** Two-dimensional heat flow anomalies of the Iheya North hydrothermal fields. **A.** Plot of horizontal variation in heat flow within the hydrothermal field and the central valley. **B.** Plot of estimated heat flow pattern in an east–west section through the hydrothermal field and the central valley.

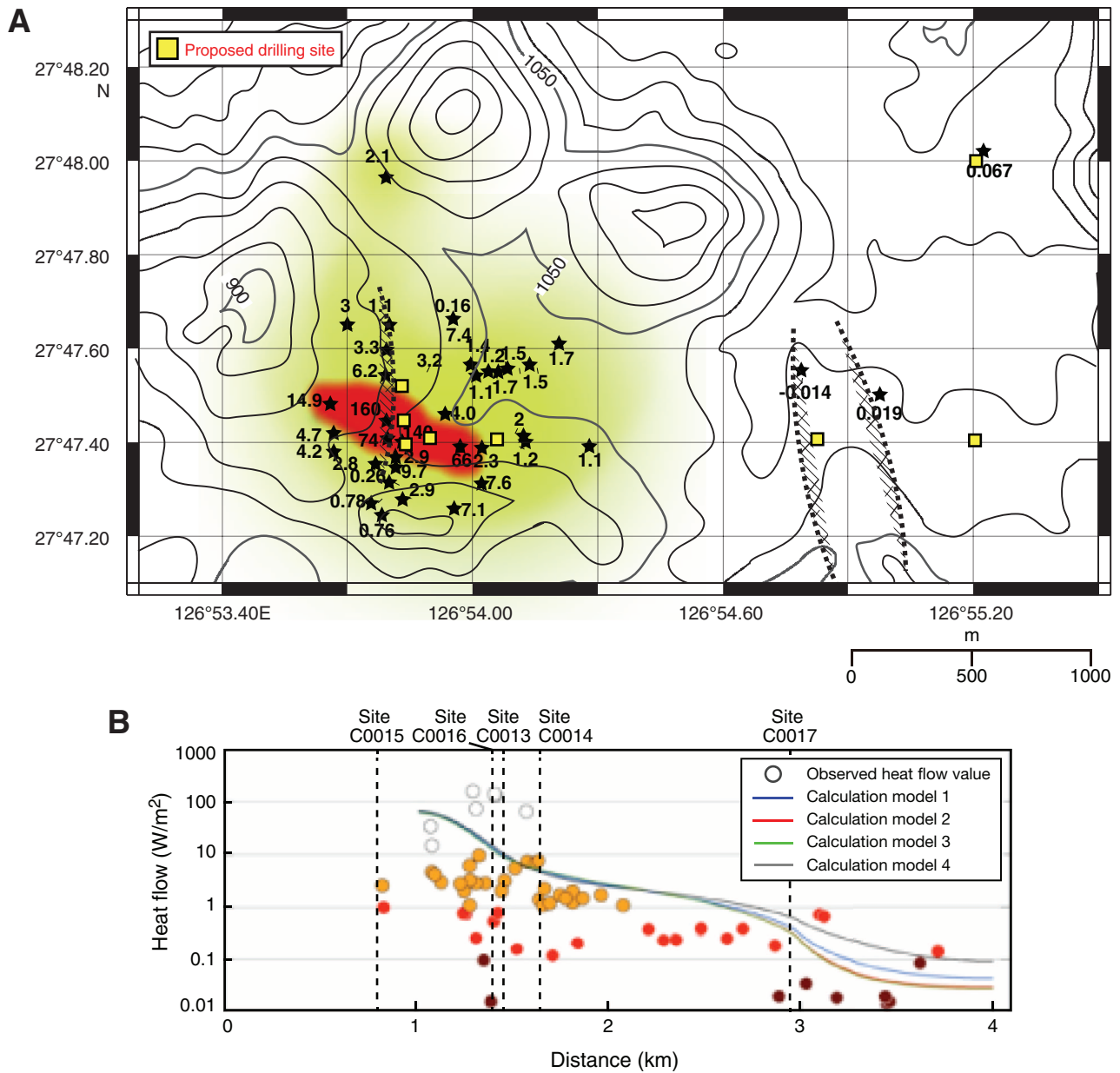


Figure F2. Bathymetric map, Site C0013.

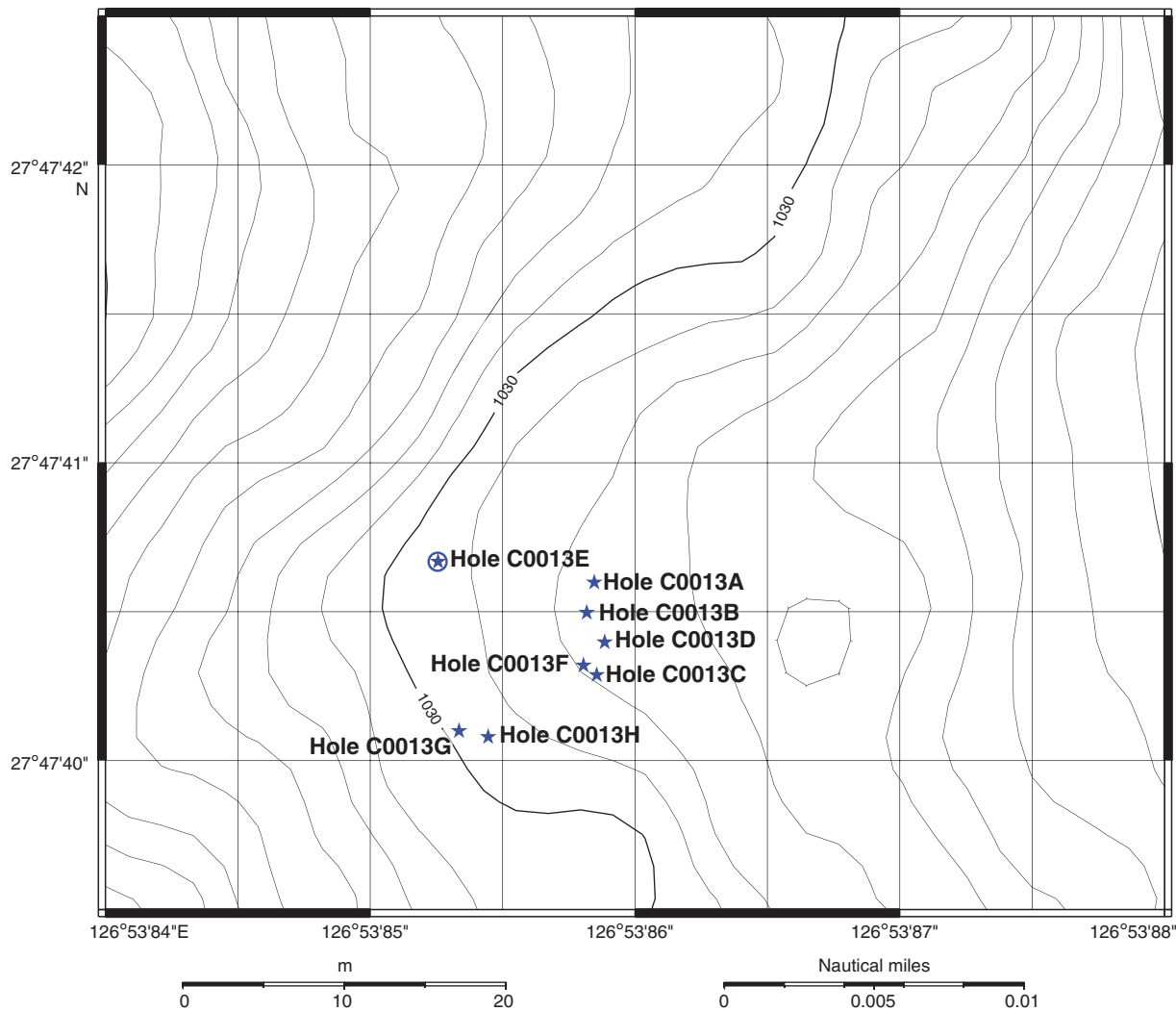
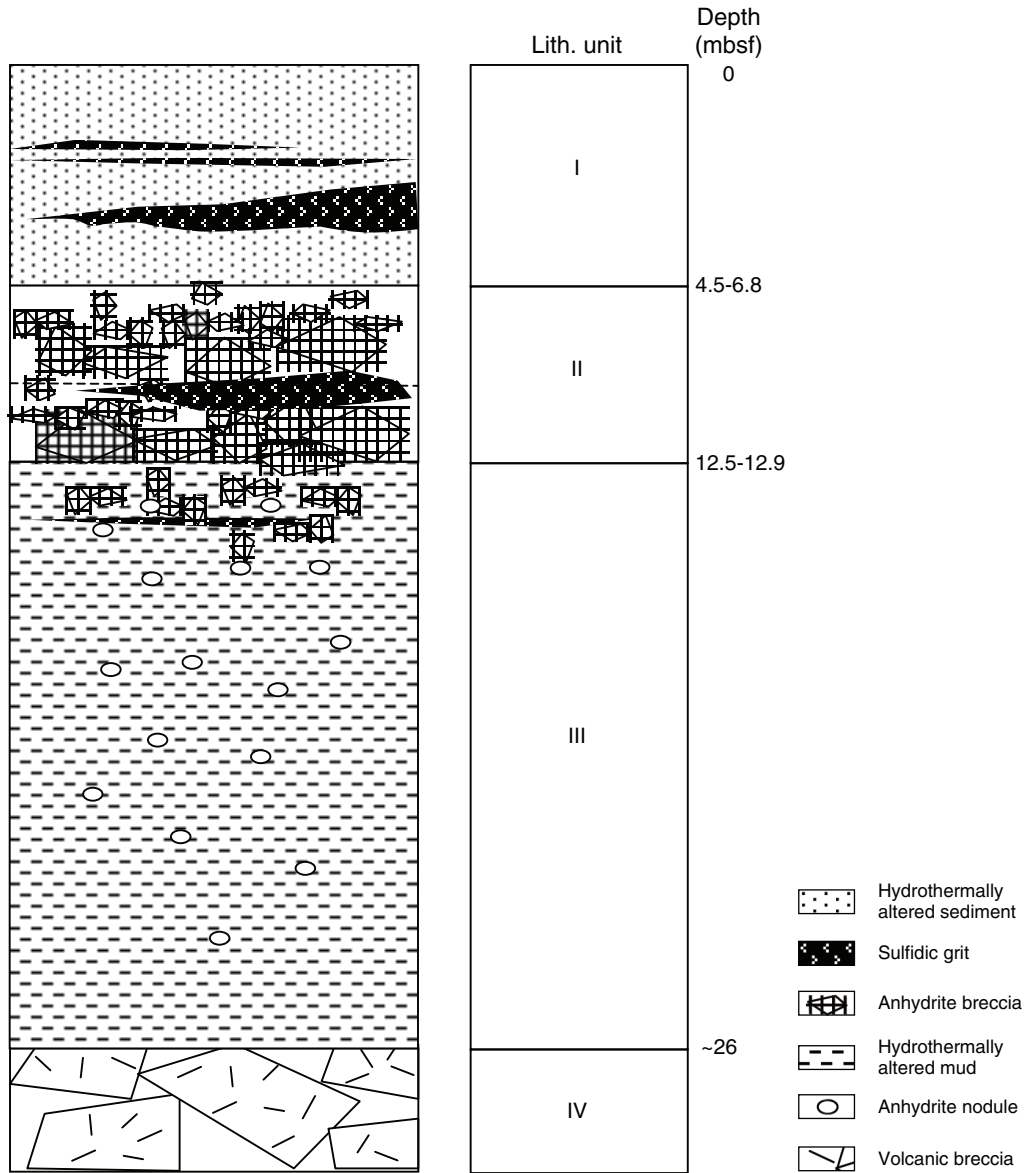
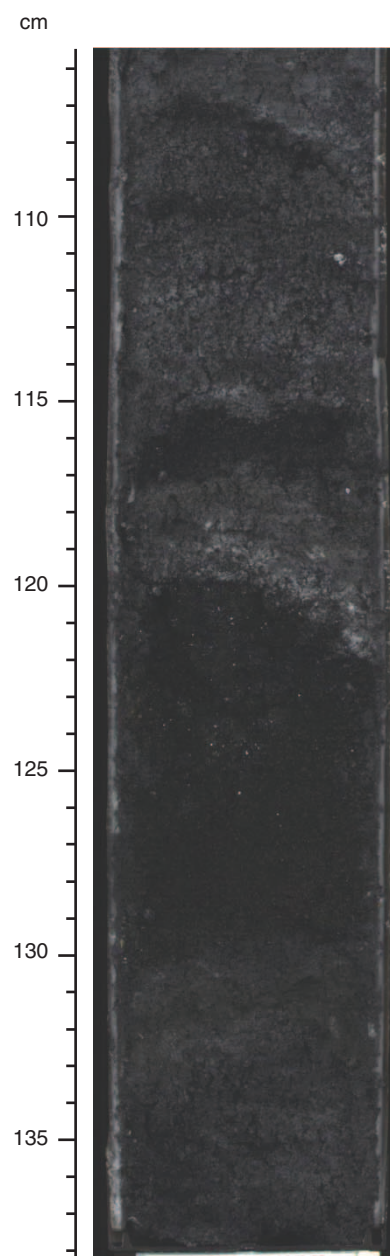


Figure F3. Diagram of lithostratigraphy at Site C0013.



**Figure F4.** Core photograph illustrating the tight interbedding between gray hydrothermally altered mud and black coarse-grained sulfidic grit (interval 331-C0013E-1H-4, 106–138 cm).



**Figure F5.** Core photographs of hydrothermal lithoclasts. **A.** Subrounded grains of sphalerite with minor anhydrite and pyrite grains (interval 331-C0013E-1H-4, 106–138 cm). **B.** Oblate sphalerite grains with euhedral anhydrite overgrowths (bottom right) (interval 331-C0013E-1H-4, 106–138 cm). **C.** Rounded, near-spherical hydrothermal lithoclast of sphalerite and quartz (interval 331-C0013E-1H-5, 75 cm).



**Figure F6.** X-ray CT scan (left) and core photograph (right) of euhedral vein anhydrite disrupted by drilling (interval 331-C0013C-1H-5, 2–24 cm). Note the high-density response on X-ray CT due to the presence of sulfide minerals on the left side of the image.

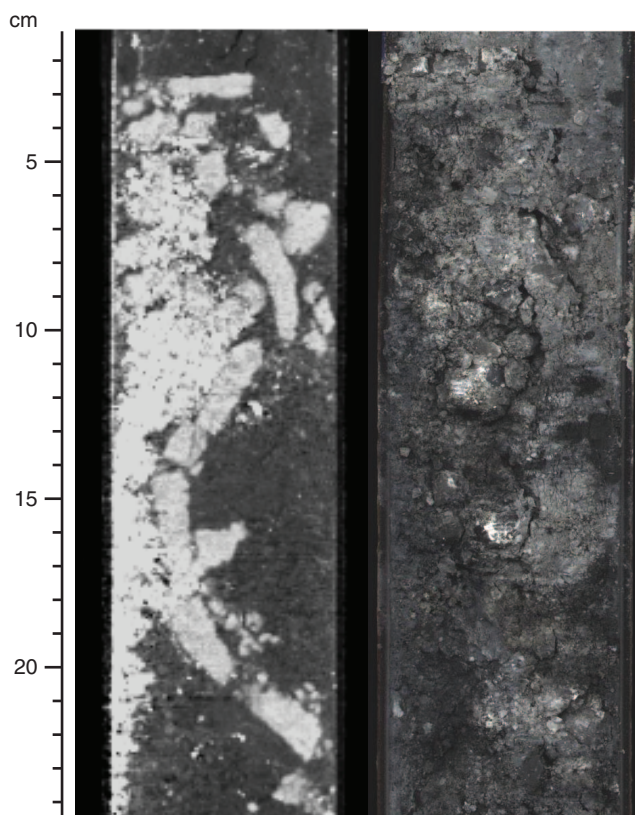


**Figure F7.** Core photographs of vein clasts from Unit II (interval 331-C0013C-1H-5, 0–25 cm). **A.** Euhedral anhydrite crystal with sphalerite inclusions. Box = area shown in B. **B.** Close-up showing inclusions of sphalerite. **C.** Anhydrite vein with sphalerite and numerous calcite and anhydrite overgrowths.

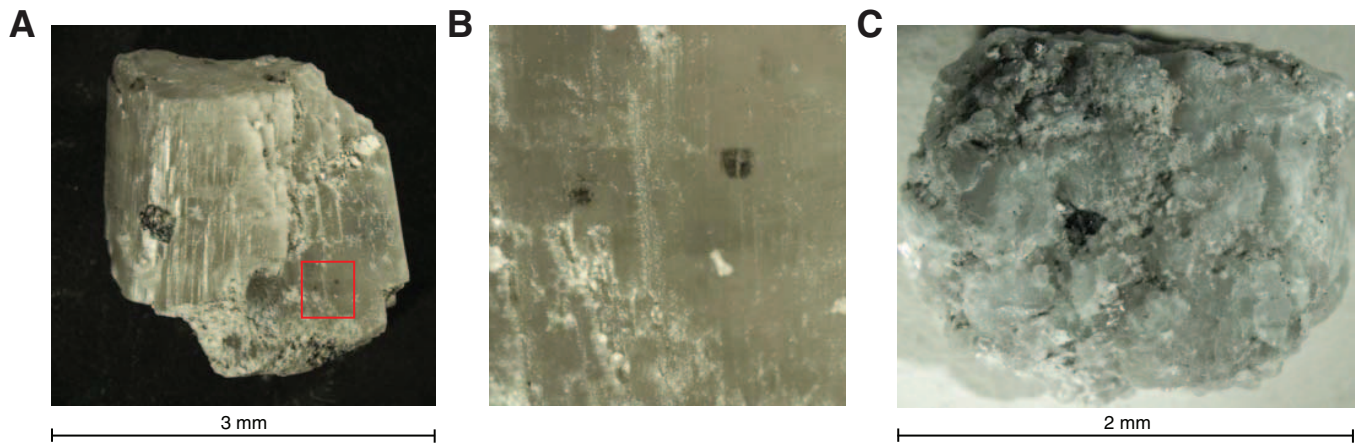


**Figure F8.** X-ray CT scan (left) and core photograph (right) of nodular anhydrite interval (331-C0013D-2H-1, 0–58 cm). Compare to Figure F6. Note rounding of clast, reduced brightness in X-ray CT image, and aggregate structure.

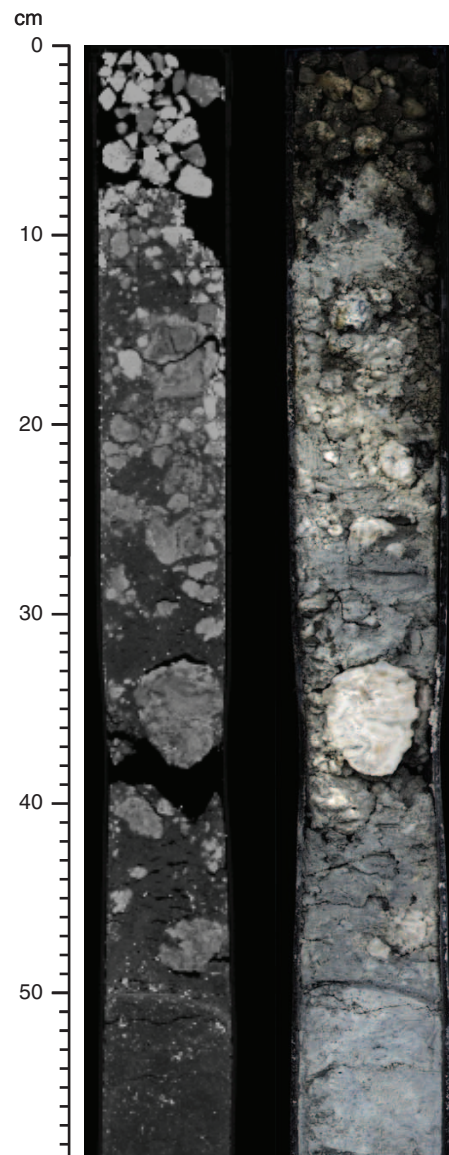


**Figure F9.** Core photographs. **A.** Interval 331-C0013E-6X-CC, 28–43 cm. a = heavily vesiculated glass, now devitrified to clay and minor Mg chlorite. b, c = monomictic breccias comprising clasts of hydrothermally altered pumice in silica. Note the jigsaw texture, which indicates minimal movement of clasts. d = interbedded gray hydrothermal mud. **B.** Interval 331-C0013E-6X-CC, 8–27 cm. e = block of polymictic volcanic breccia in devitrified lava. f, g = complete loss of original textures because of silicification.

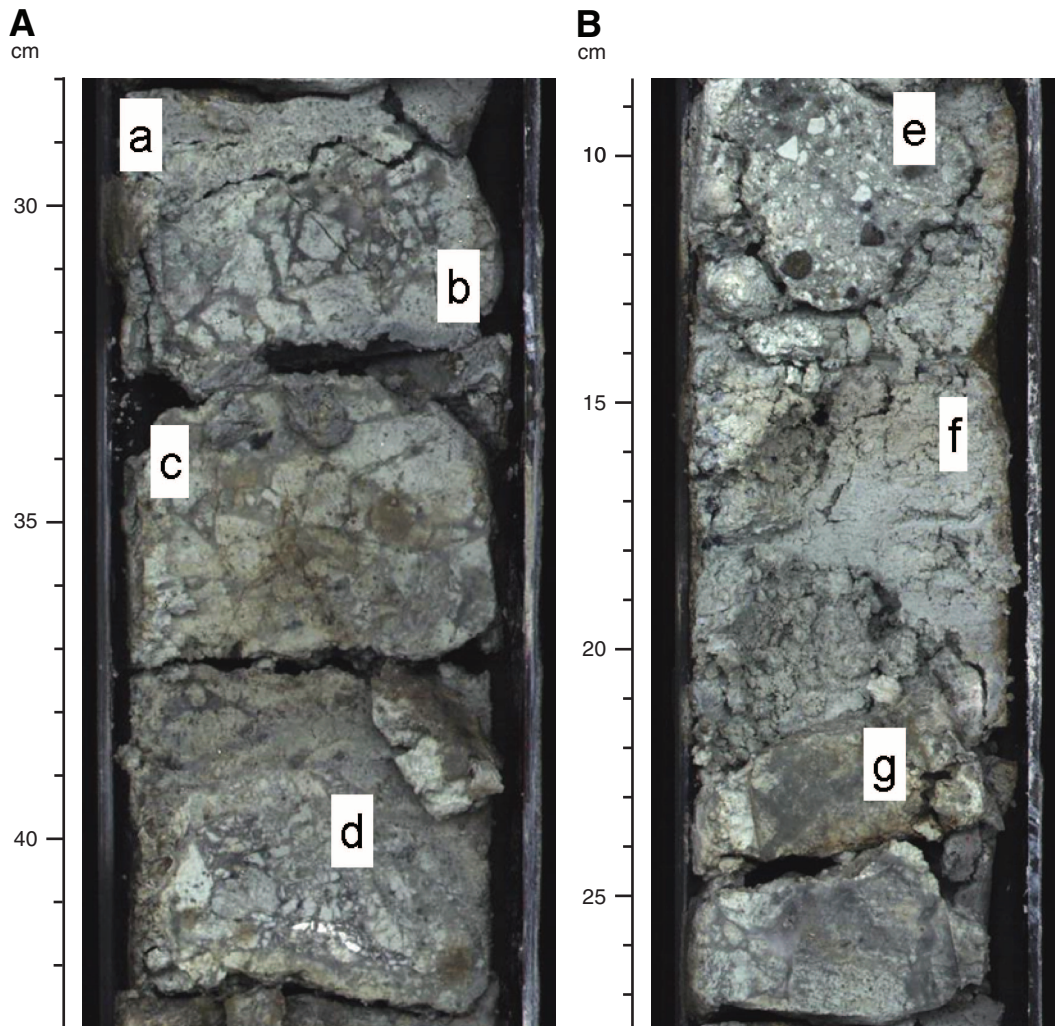


**Figure F10.** A–C. Thin section images of a polymict volcanic breccia clast containing vesicular flow-banded glassy volcanic rock in a silicified matrix, Site C0013. Primary volcanic glass forms the ground mass of the pumice clasts (extinct in cross polars in B and C). Quartz and opaque sulfide mineralization follow stretched vesicles. Secondary illite and Mg chlorite predominate over primary phyllosilicates.

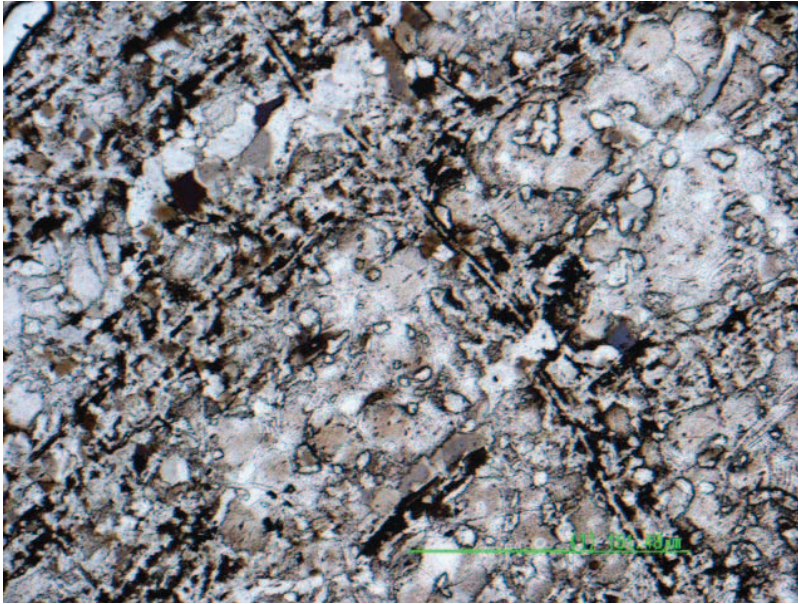
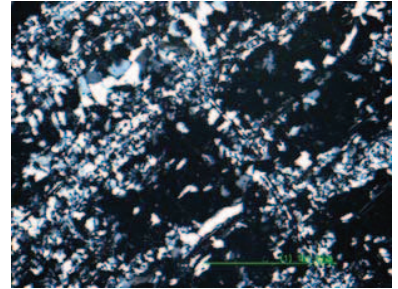
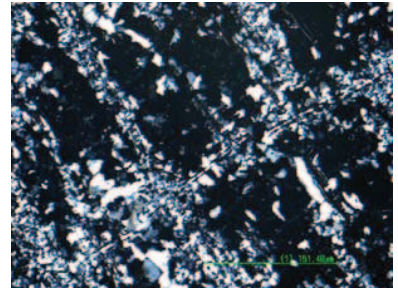
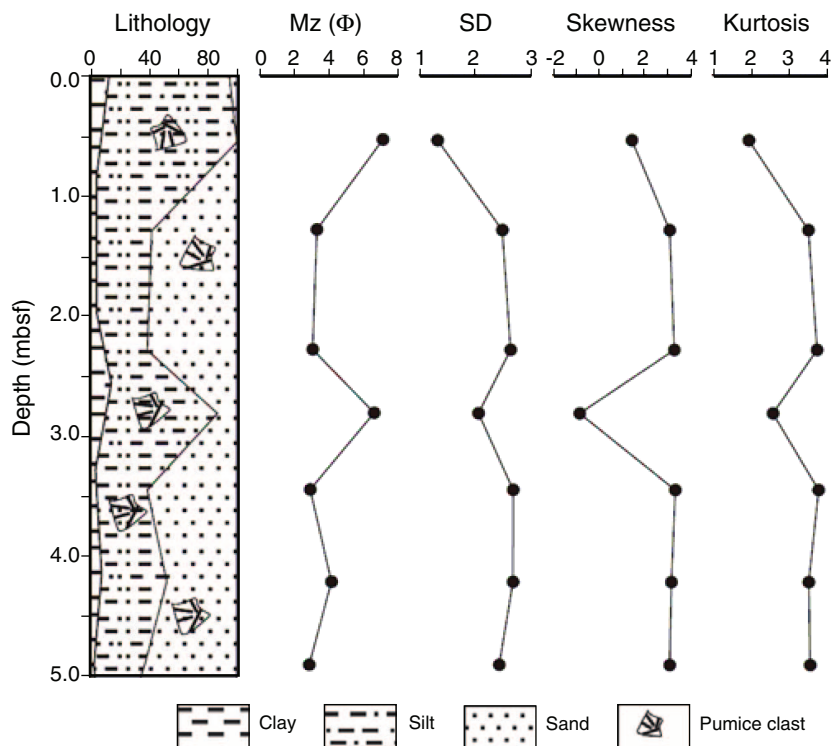
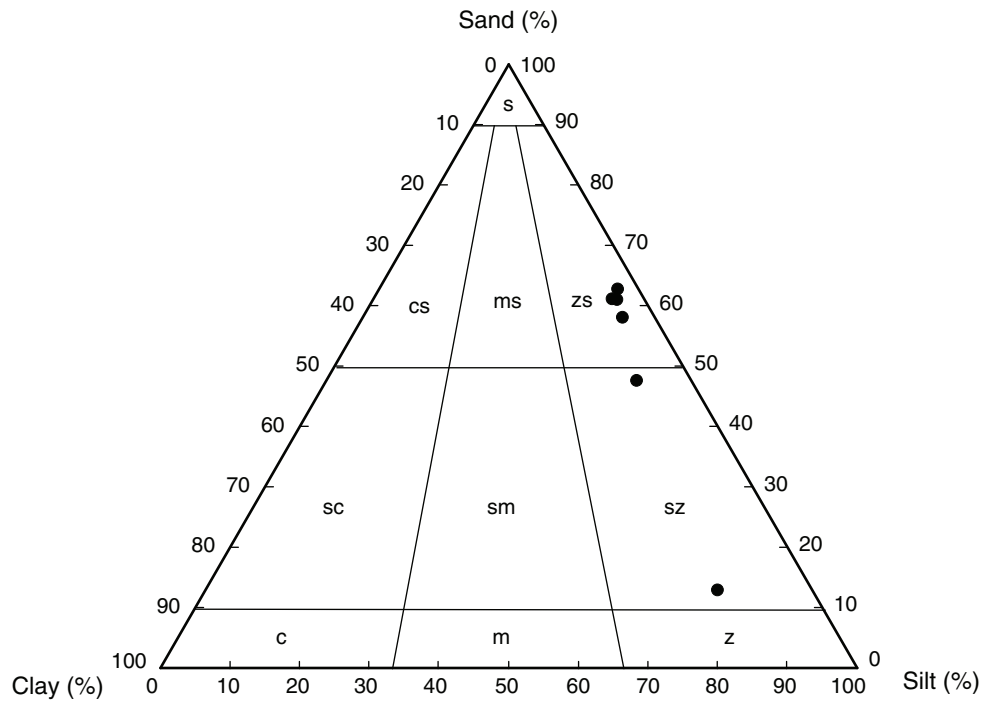
**A****B****C**

Figure F11. Plots of grain size compositions of sediments from Hole C0013F. SD = standard deviation.



**Figure F12.** Diagram of grain size classification based on Folk and Ward (1957), Hole C0013F. s = sand, cs = clayey sand, ms = muddy sand, zs = silty sand, sc = sandy clay, sm = sandy mud, sz = sandy silt, c = clay, m = mud, z = silt.



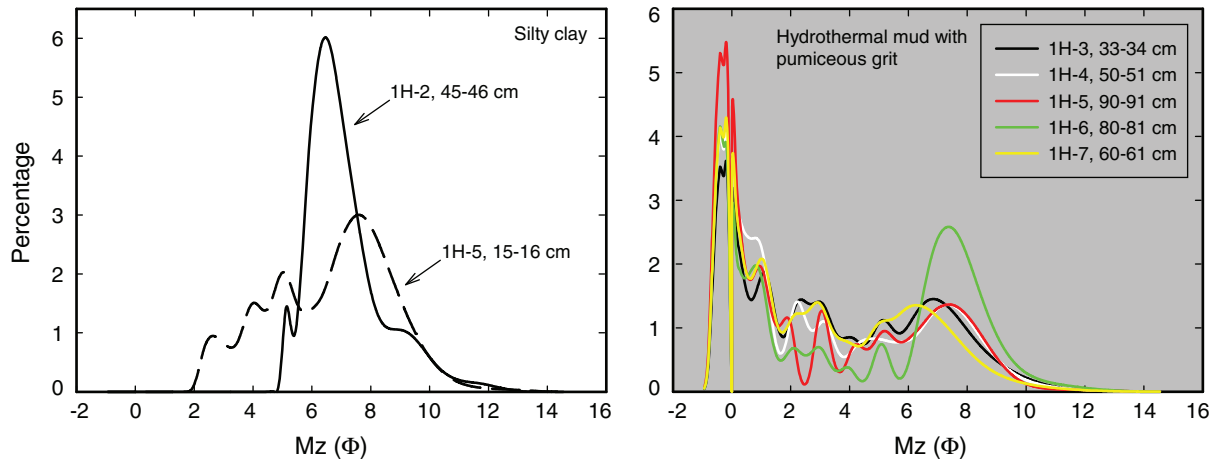
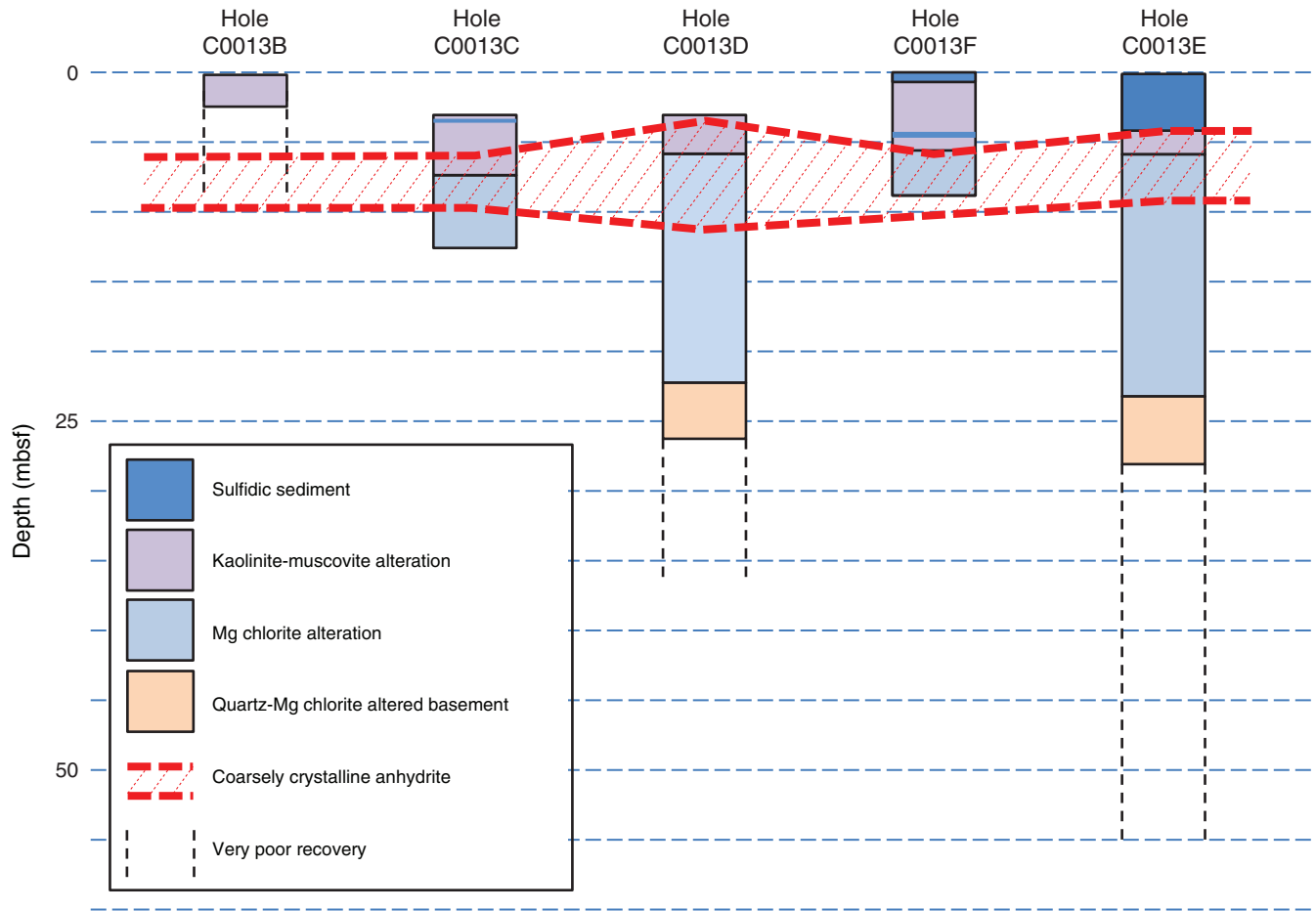
**Figure F13.** Plot of volume percentages of grain size fractions of Hole C0013F sediments.

Figure F14. Summary of alteration assemblages and major mineral phases identified at Site C0013.



**Figure F15.** Core photographs. A. Native sulfur-bearing unit at the top of Hole C0013E (interval 331-C0013E-1H-1, 0–8 cm). Note that sulfur occurs as veinlets and cements the other components of the unit, implying that it was liquid when the interval formed. (Continued on next page.)

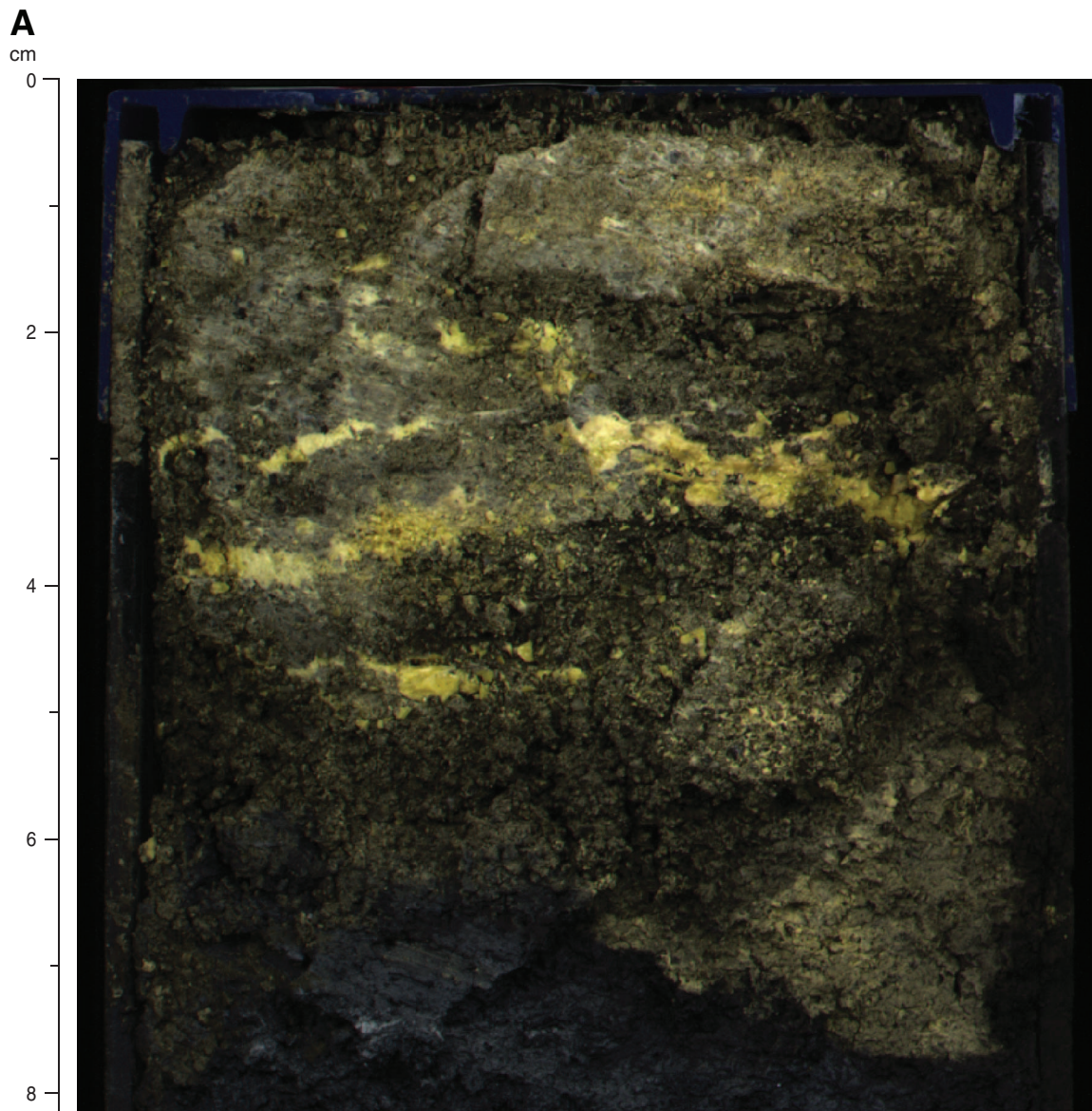
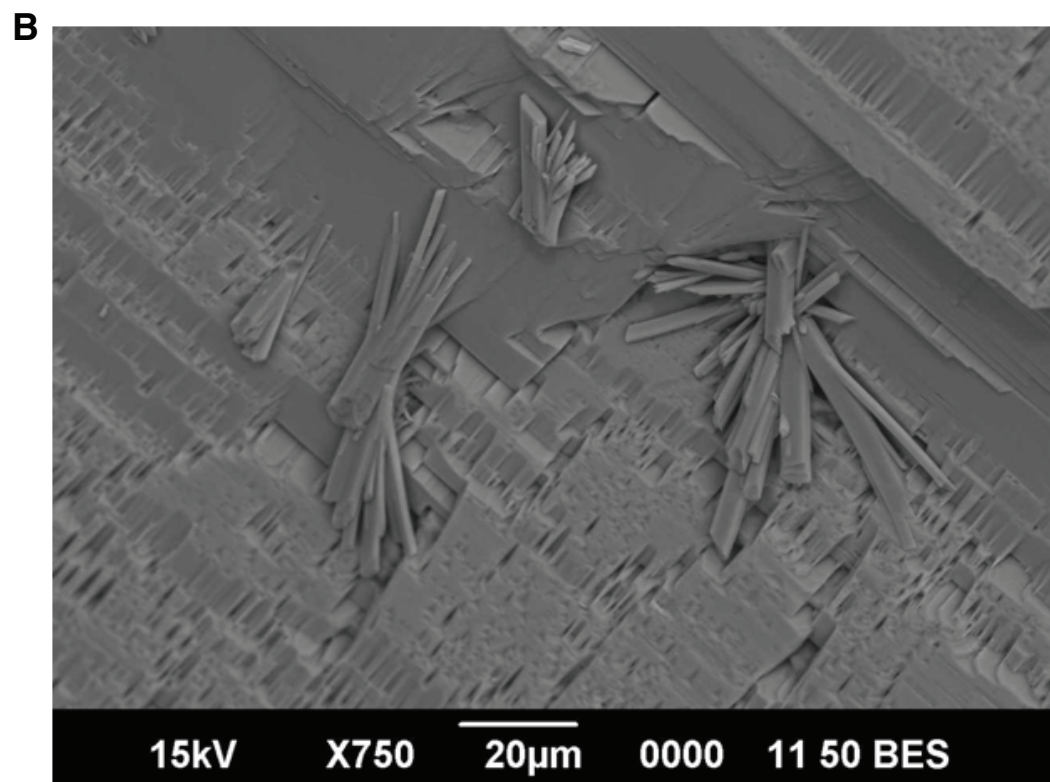
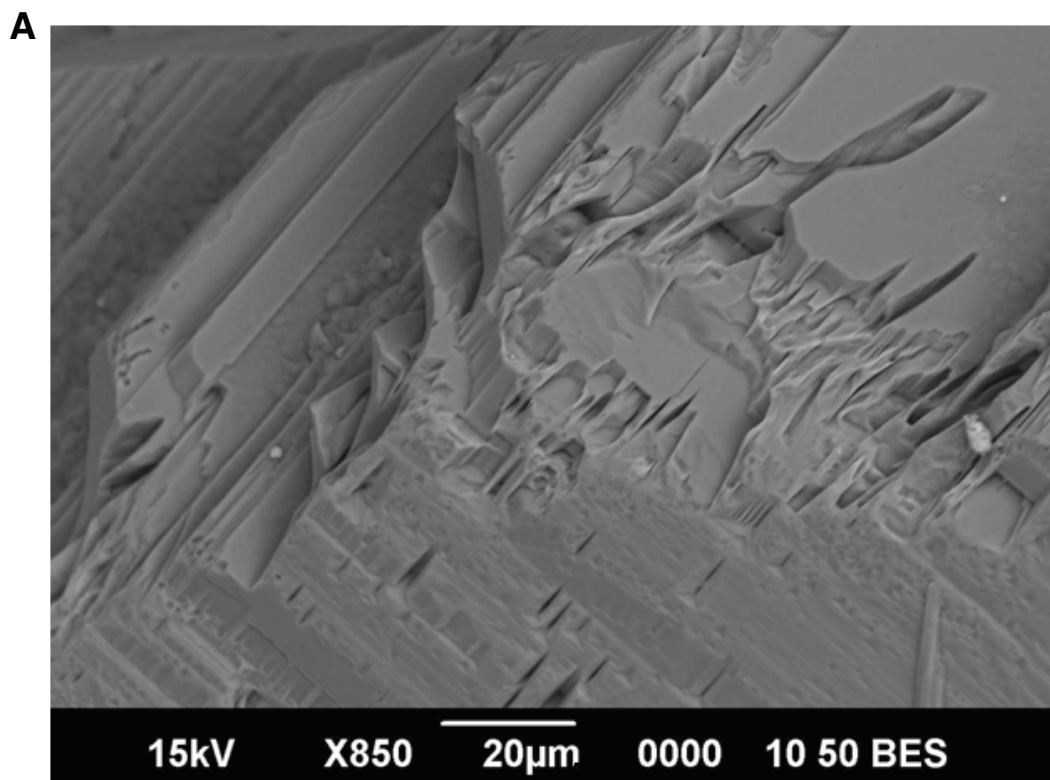


Figure F15 (continued). B. Native sulfur-lined voids (interval 331-C0013F-1H-2, 33–38 cm).

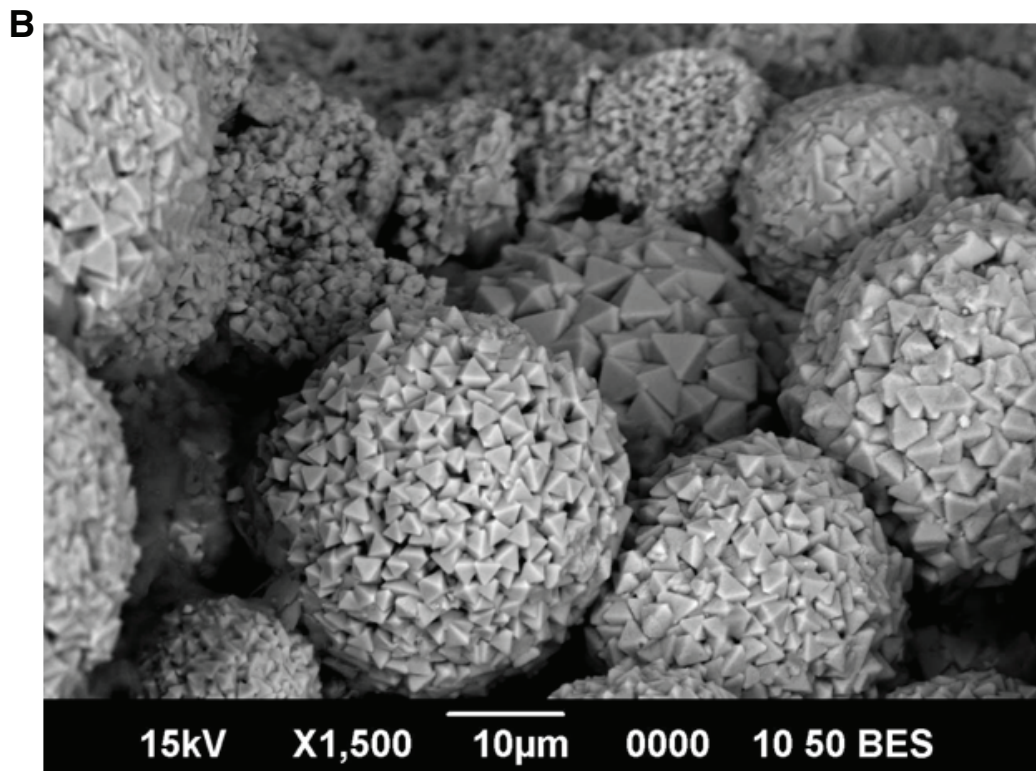
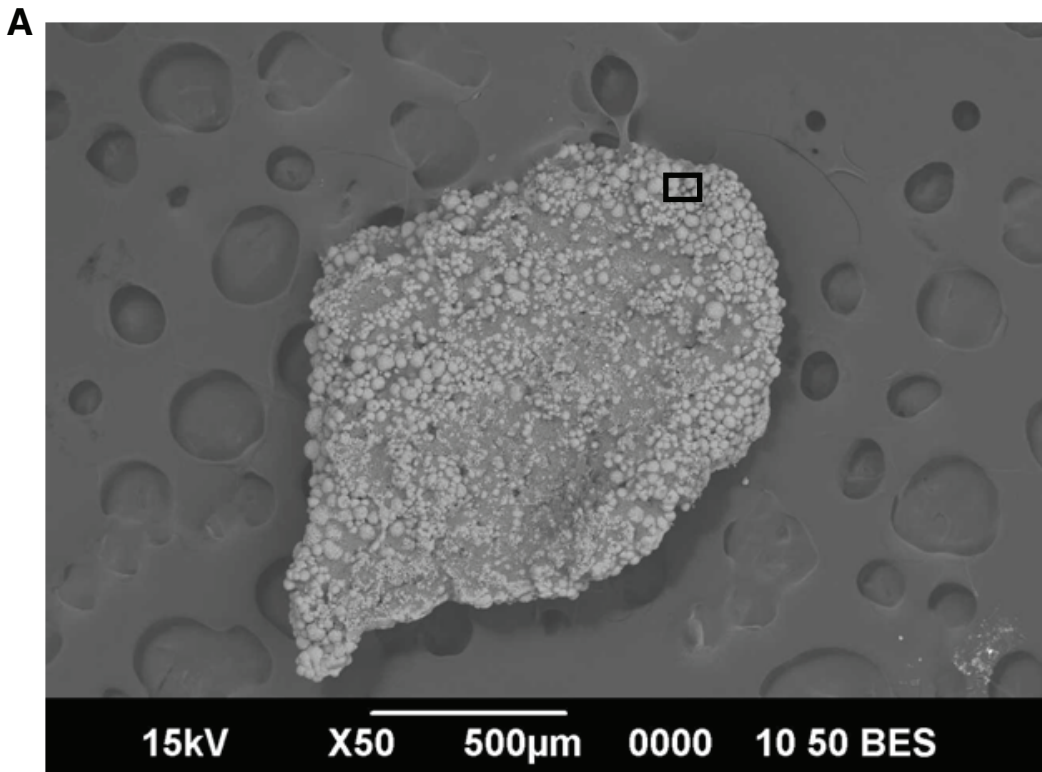
**B**  
cm



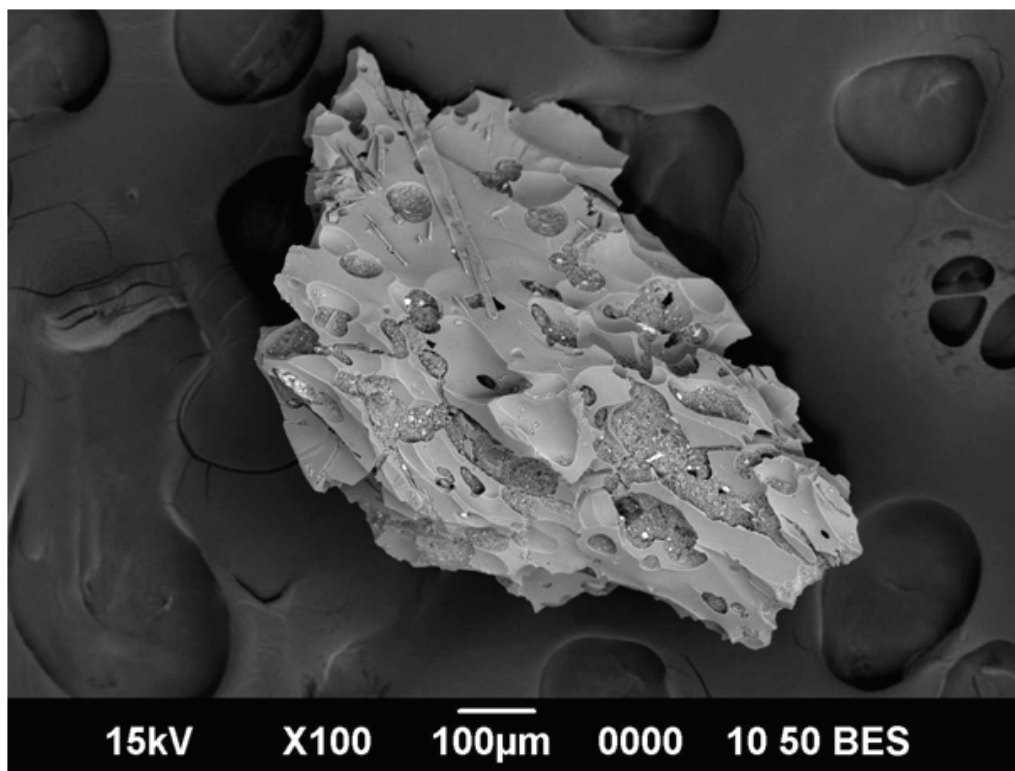
**Figure F16.** High-resolution SEM photomicrographs of the surface of an anhydrite grain from Sample 331-C0013B-1T-CC-WR, 25–26 cm, showing (A) dissolution pitting across its surface and (B) hydration to gypsum during dissolution.



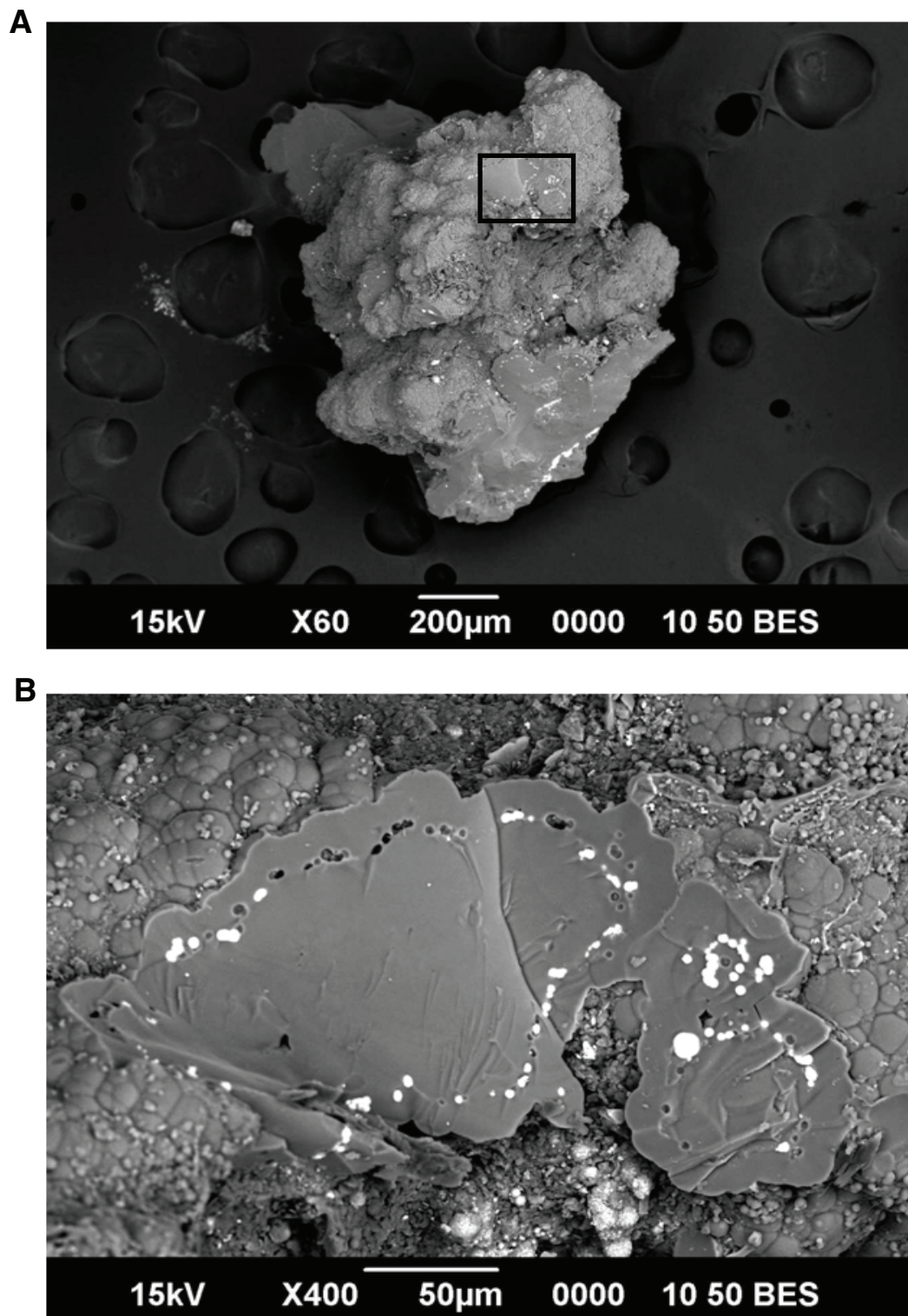
**Figure F17.** A. SEM photomicrograph of a framboidal pyrite aggregate from Sample 331-C0013B-1T-CC-WR, 25–26 cm. B. High-resolution SEM photomicrograph of the box from A. Framboidal pyrite aggregates are common in the sulfidic sediment sequence.



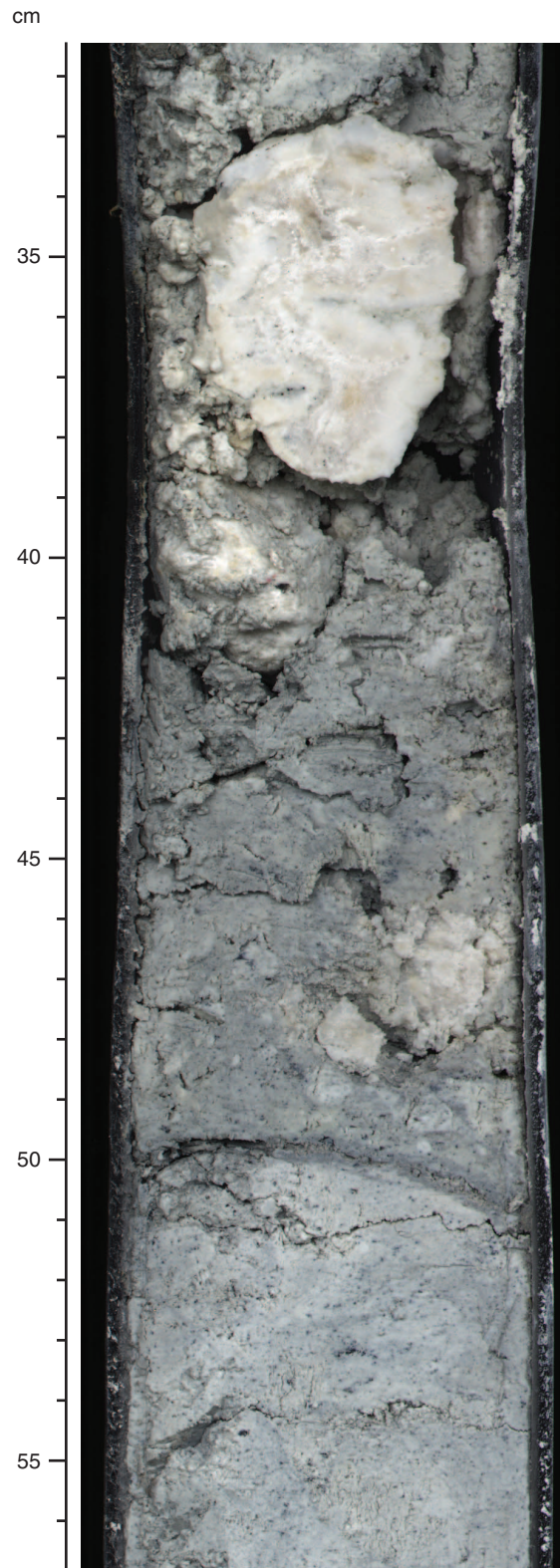
**Figure F18.** SEM photomicrograph of volcanic glass from Sample 331-C0013B-1T-CC-WR, 25–26 cm, illustrating incipient breakdown to clay aggregates.



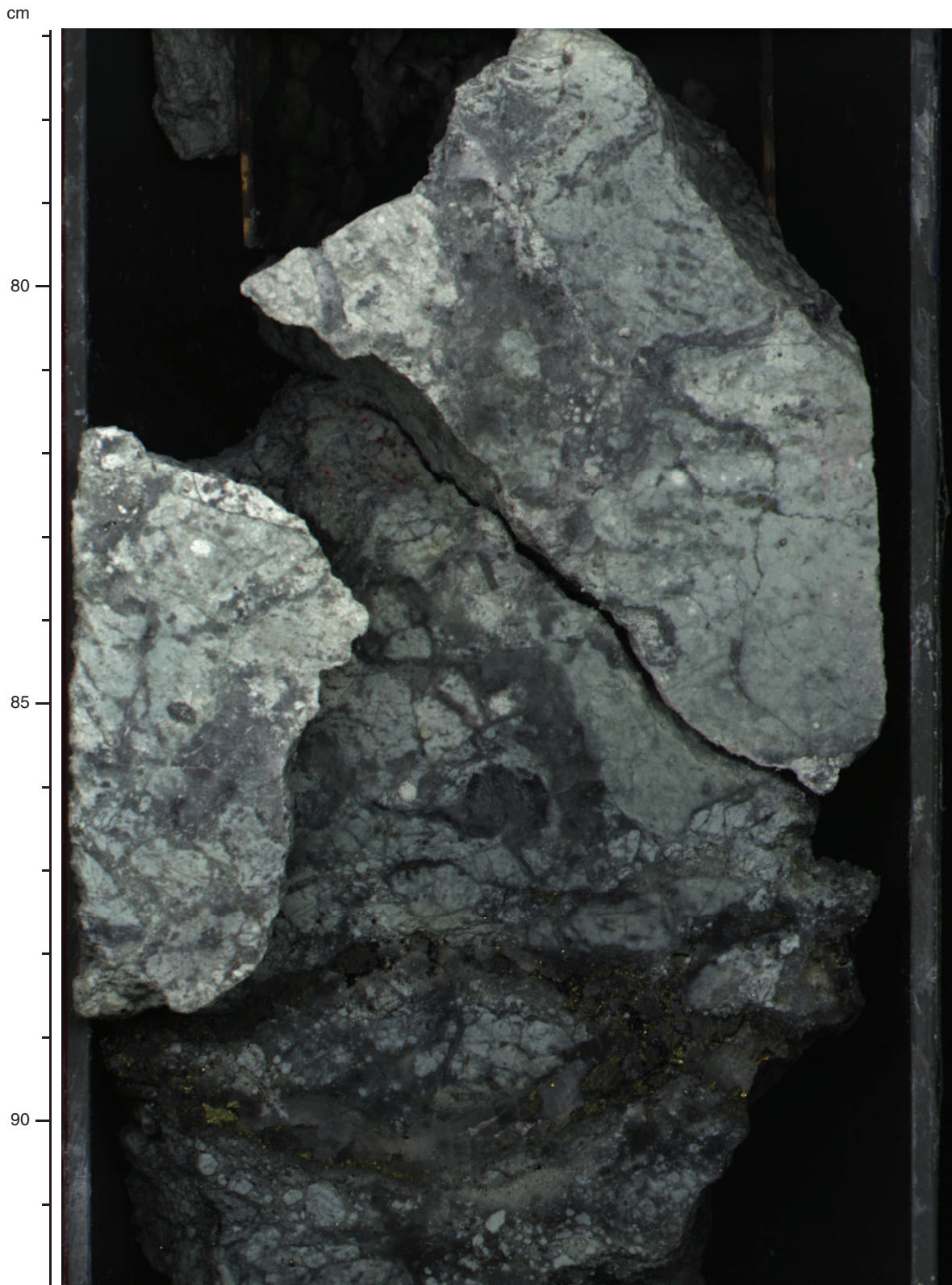
**Figure F19.** SEM photomicrographs. A. Opaline silica (Sample 331-C0013B-1T-CC-WR, 25–26 cm). B. Close-up of area from box in A. The bright white material is arsenic sulfide (from EDS analysis).



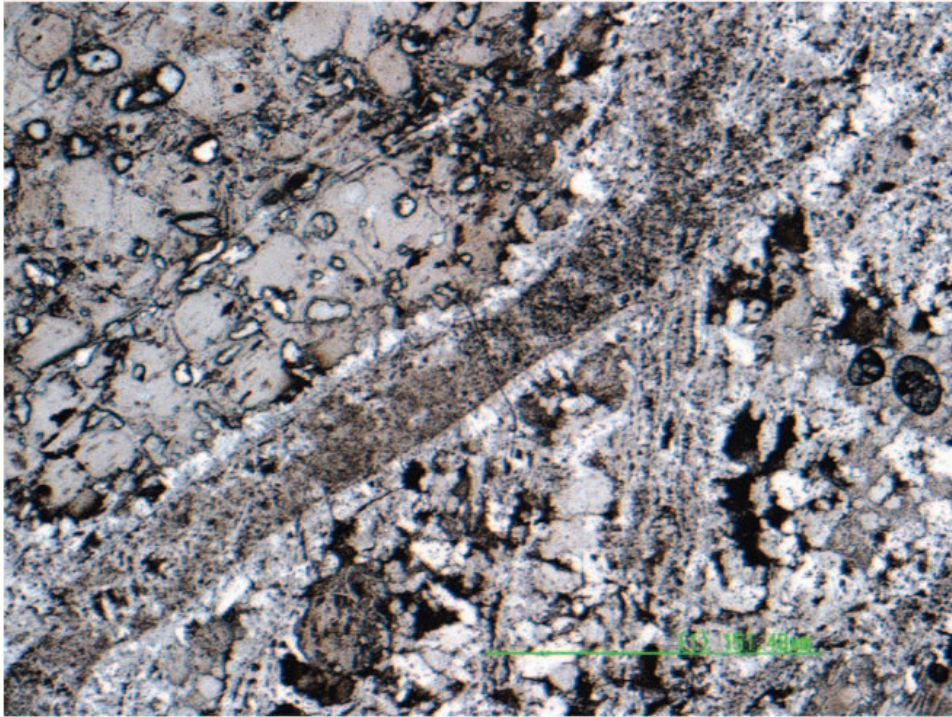
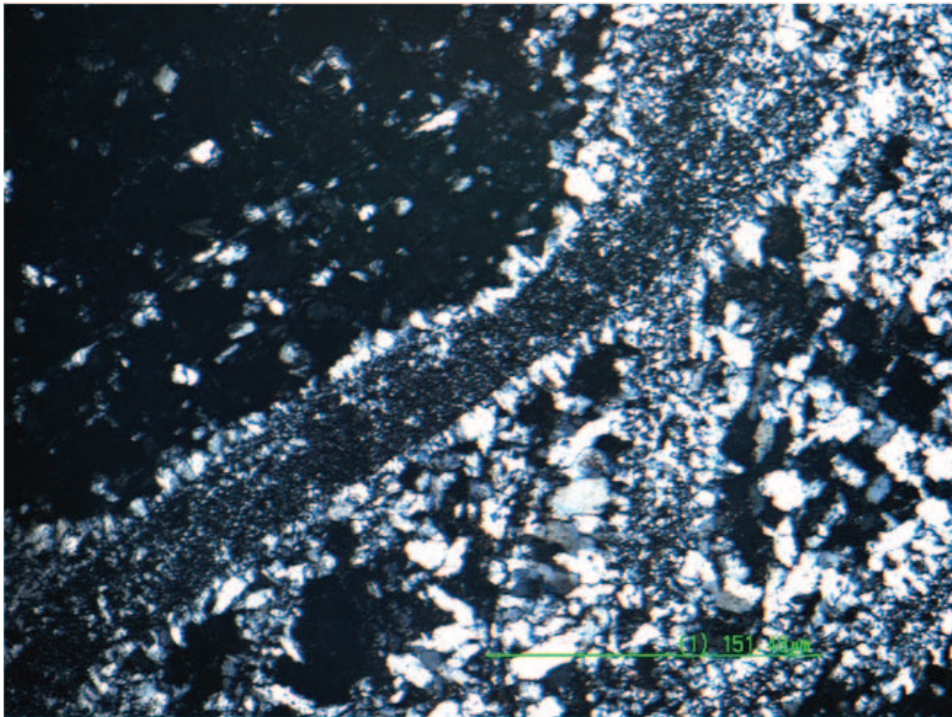
**Figure F20.** Core photograph of mottled Mg chlorite + anhydrite alteration, showing distinctive bluish-gray clay and white nodules of anhydrite (interval 331-C0013D-2H-1, 31.5–56 cm). Note the truncation of the internal structure of the large nodule at the top of the image, indicating physical or chemical erosion following precipitation.



**Figure F21.** Core photograph of moderately quartz + Mg chlorite–altered volcanic basement showing typical quartz stockwork veining and a strongly mineralized vein containing sphalerite, pyrite, and covellite (interval 331-C0013E-7L-2, 77–92 cm).



**Figure F22.** Plane-polarized (A) and cross-polarized (B) transmitted light photomicrographs of moderately quartz + Mg chlorite–altered volcanic basement showing remnant volcanic glass (isotropic material, top left) surrounded by quartz + Mg chlorite alteration (Sample 331-C0013E-7L-CC, 60–62 cm). Field of view = 450  $\mu\text{m}$ .

**A****B**

**Figure F23.** A. Low magnification backscattered electron SEM photomicrograph of organic carbon–clay matrix containing elemental Cu (Sample 331-C0013E-7L-2-W, 35.0–35.1 cm). B. Higher magnification image of the same material, showing the form of the Cu (bright flakes).

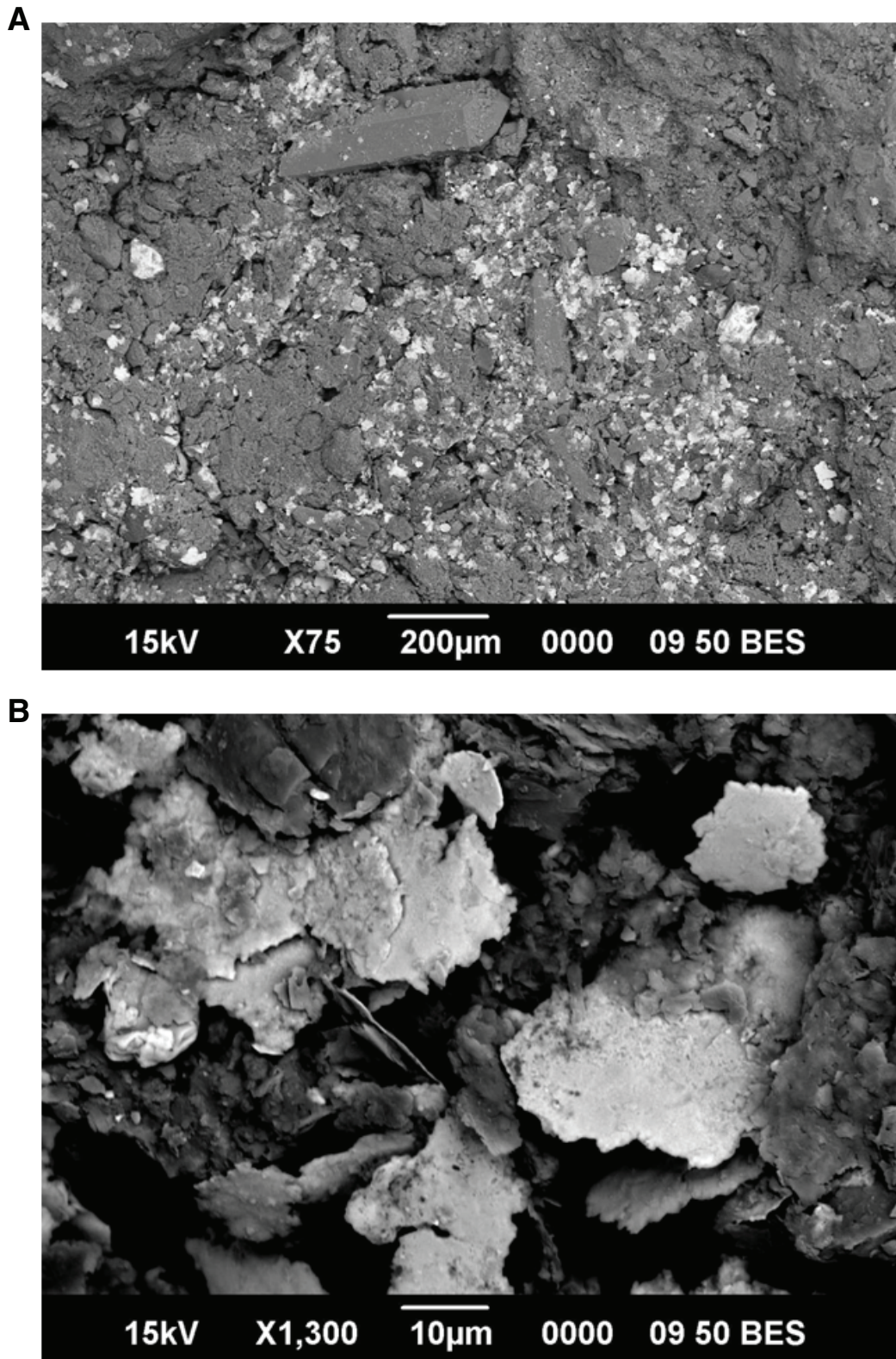


**Figure F24.** Schematic summary of evolution of hydrothermal activity and alteration at Site C0013. **A.** Eroded anhydrite veining/nodules lie within sediment on unaltered volcanic basement. **B.** Hydrothermal fluid discharge (red arrows) through the basement to the seafloor alters the volcanic rocks and sedimentary sequence and forms sulfide chimneys at the seafloor. (Continued on next page.)

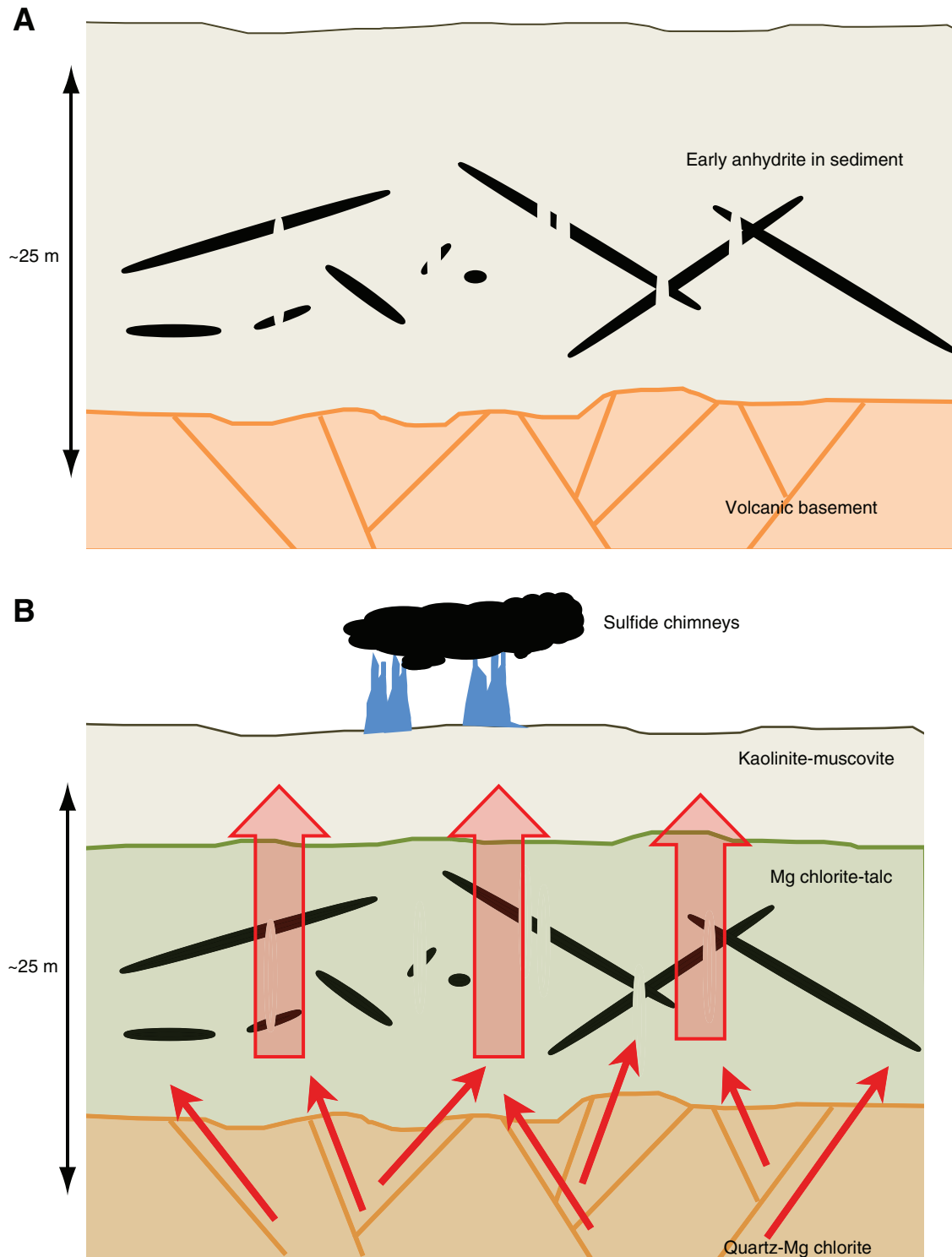


**Figure F24 (continued). C.** As the system cools and discharge ceases, seawater (blue arrows) infiltrates the altered sequence, crystallizing coarse anhydrite above the 150°C isotherm (red dashed line) while sulfide chimneys collapse to form locally sulfidic sediment.

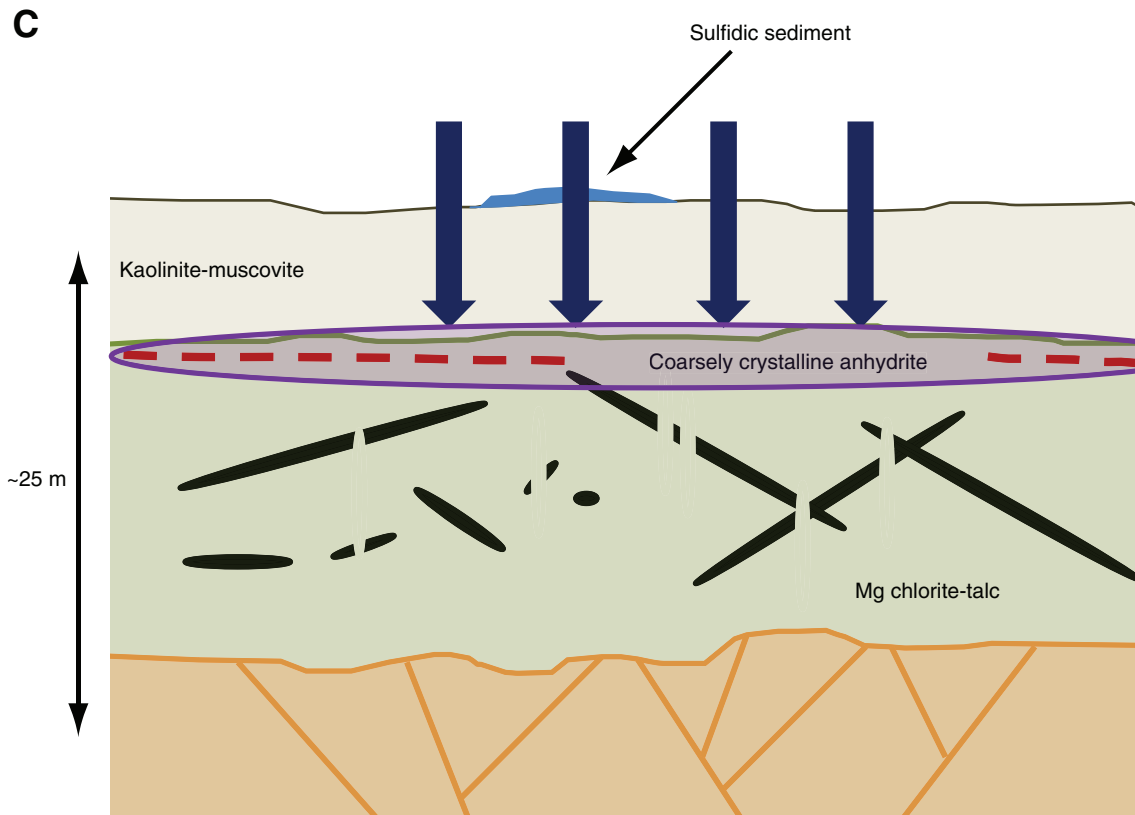
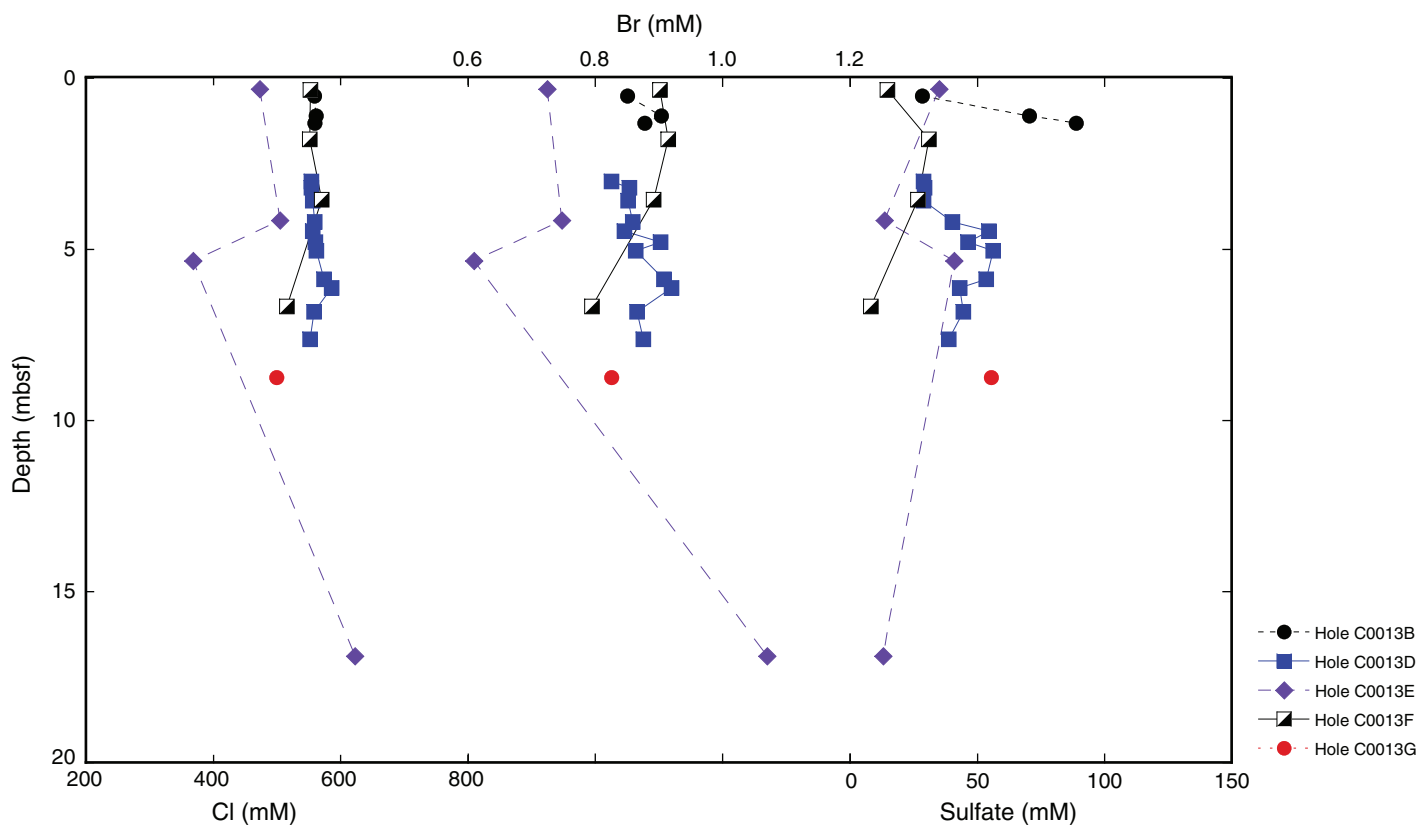


Figure F25. Plot of Cl, Br, and sulfate in pore water, Site C0013.





**Figure F26.** Plot of sodium by ion chromatography and by charge balance, Na/Cl molar ratio, K, Mg, and Ca in pore water, Site C0013.

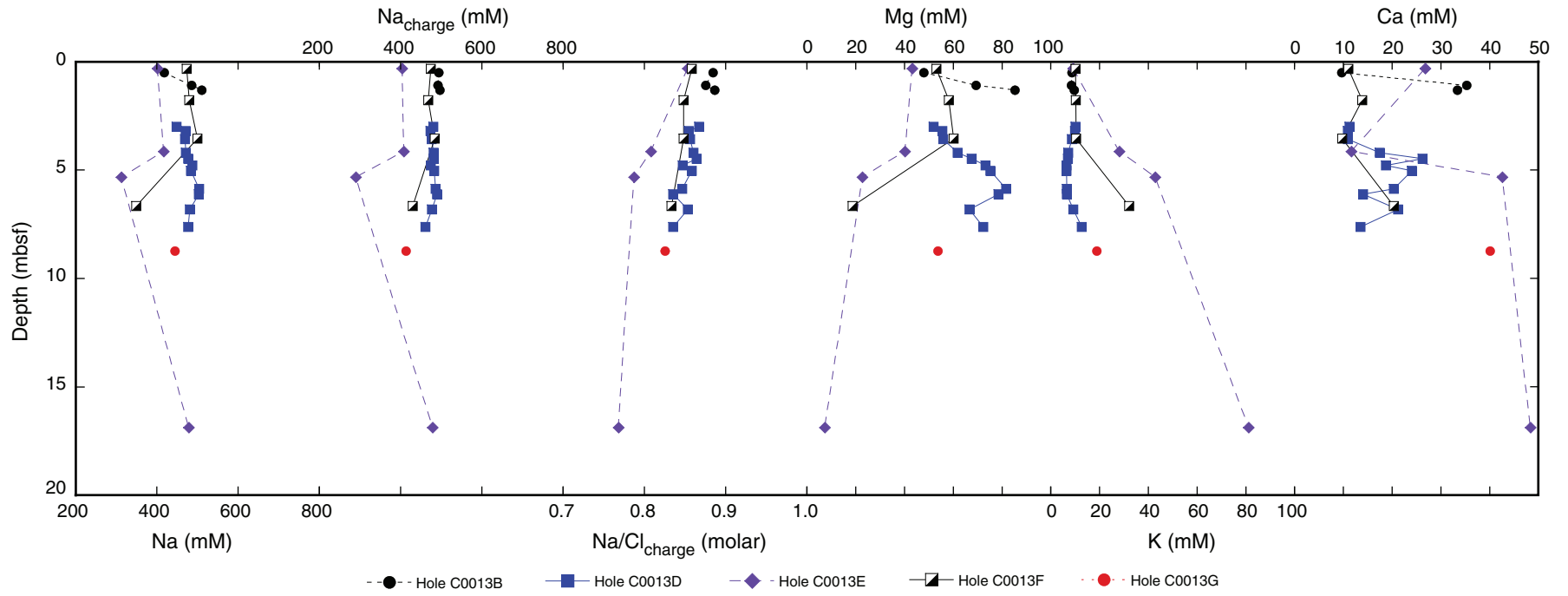


Figure F27. Plot of Rb and Cs in pore water, Site C0013.

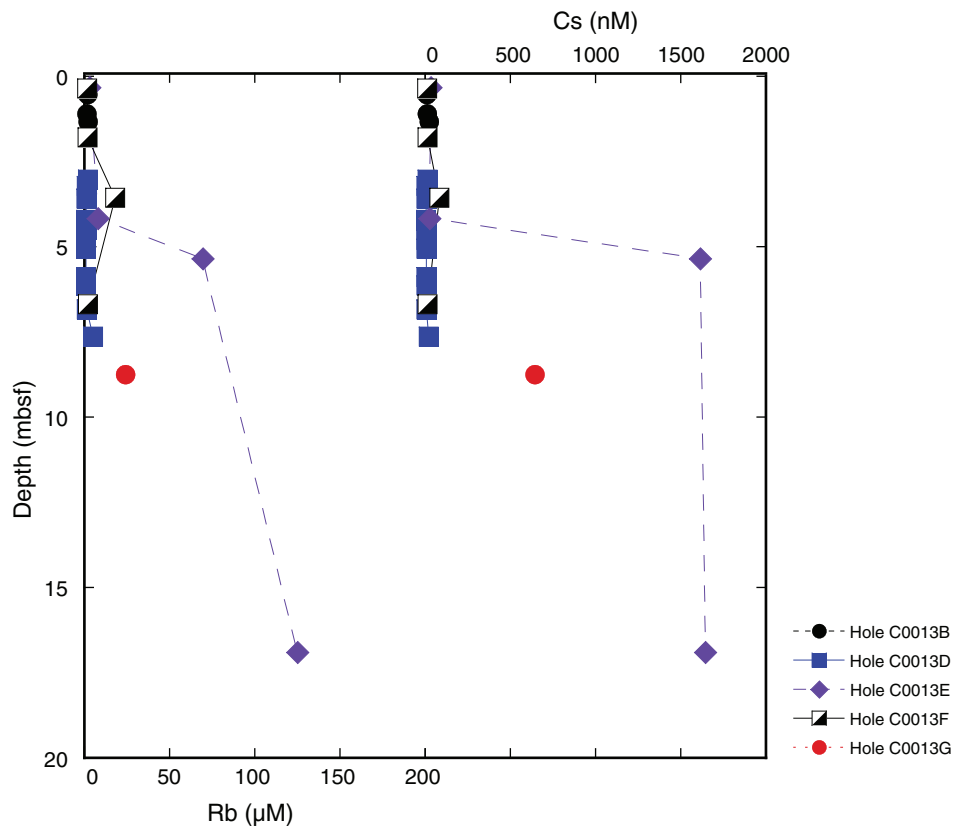




Figure F28. Plot of boron, Li, Sr, and Si measured via ICP-OES in pore water, Site C0013.

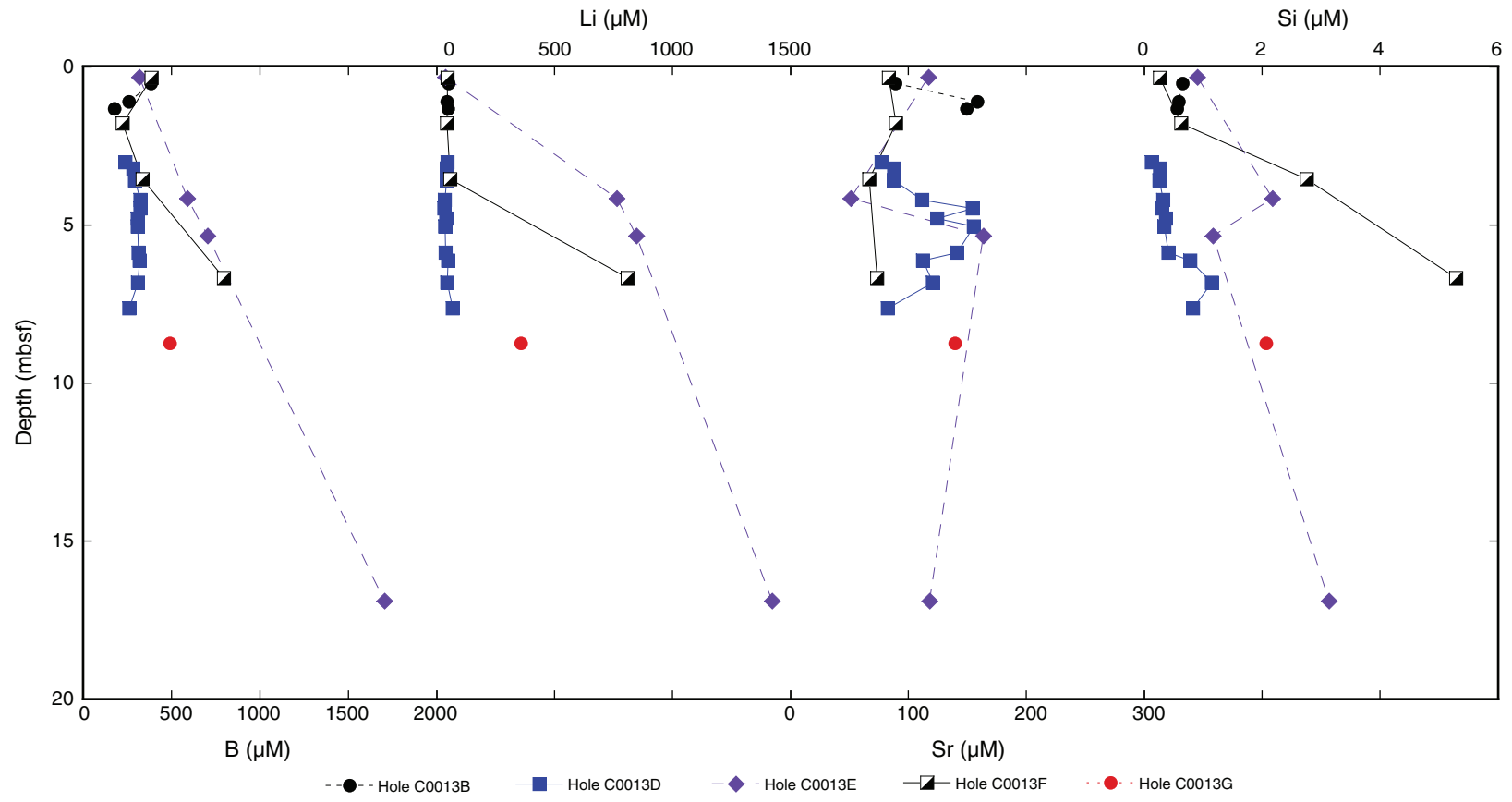


Figure F29. Plot of calcium plus magnesium in pore water plotted as a function of sulfate, Site C0013.

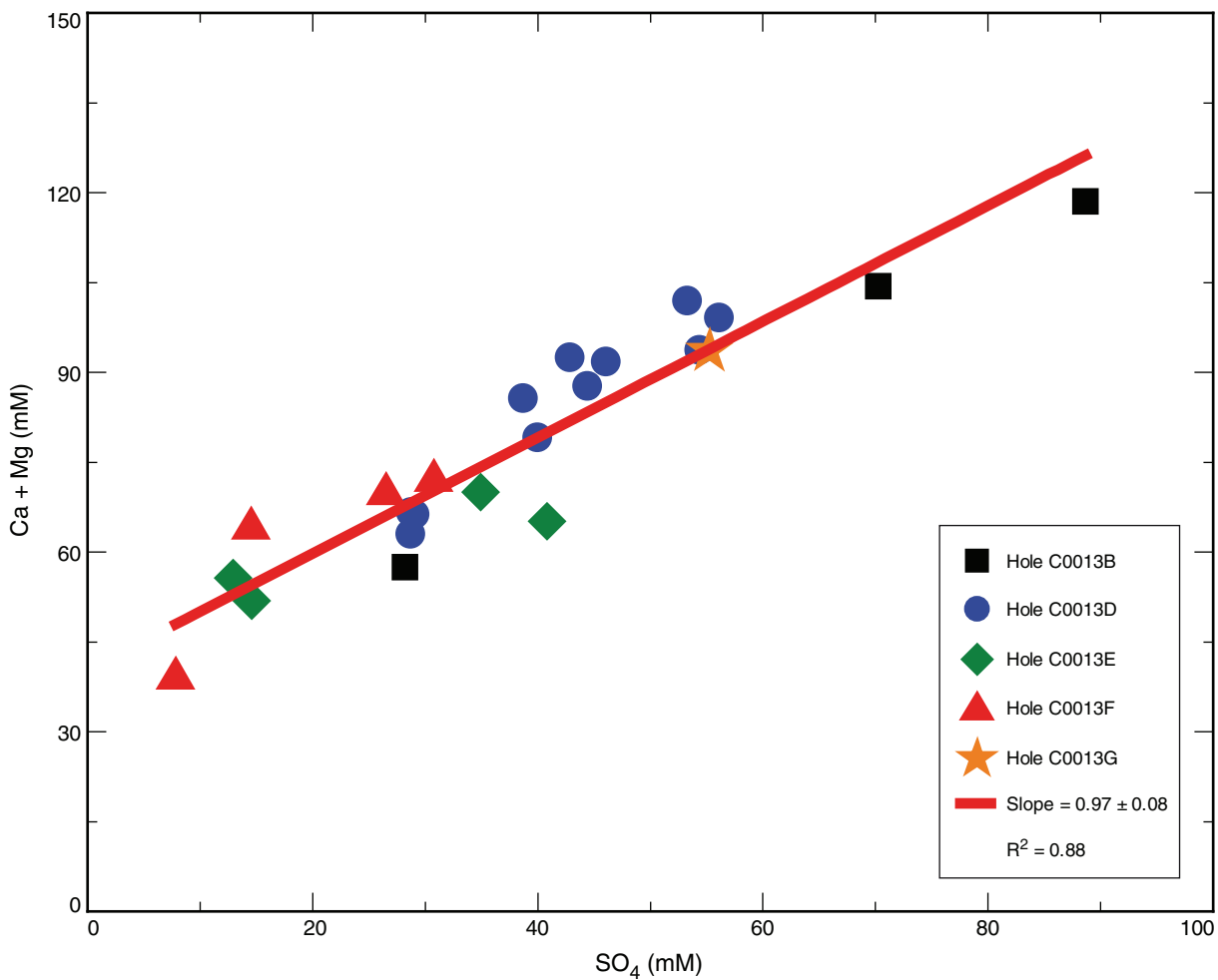
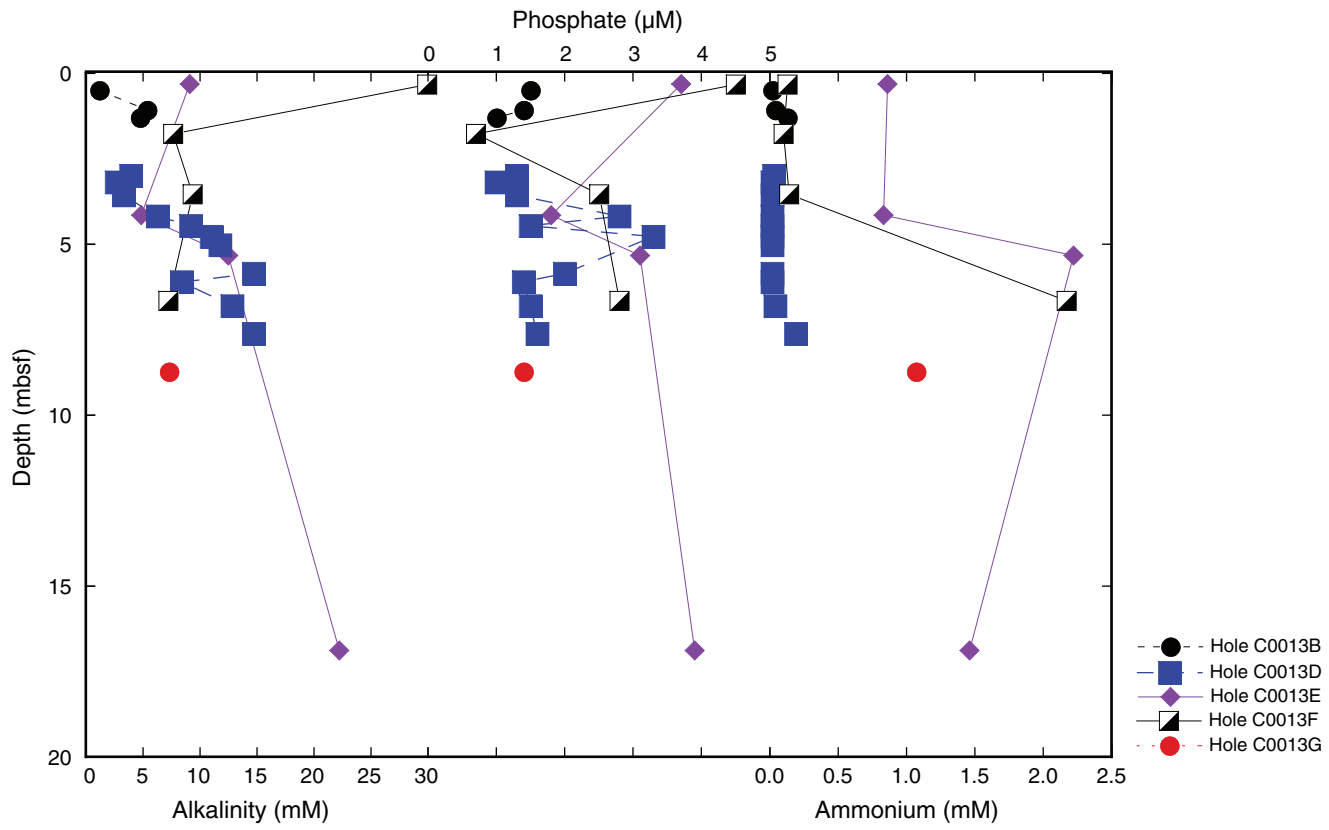
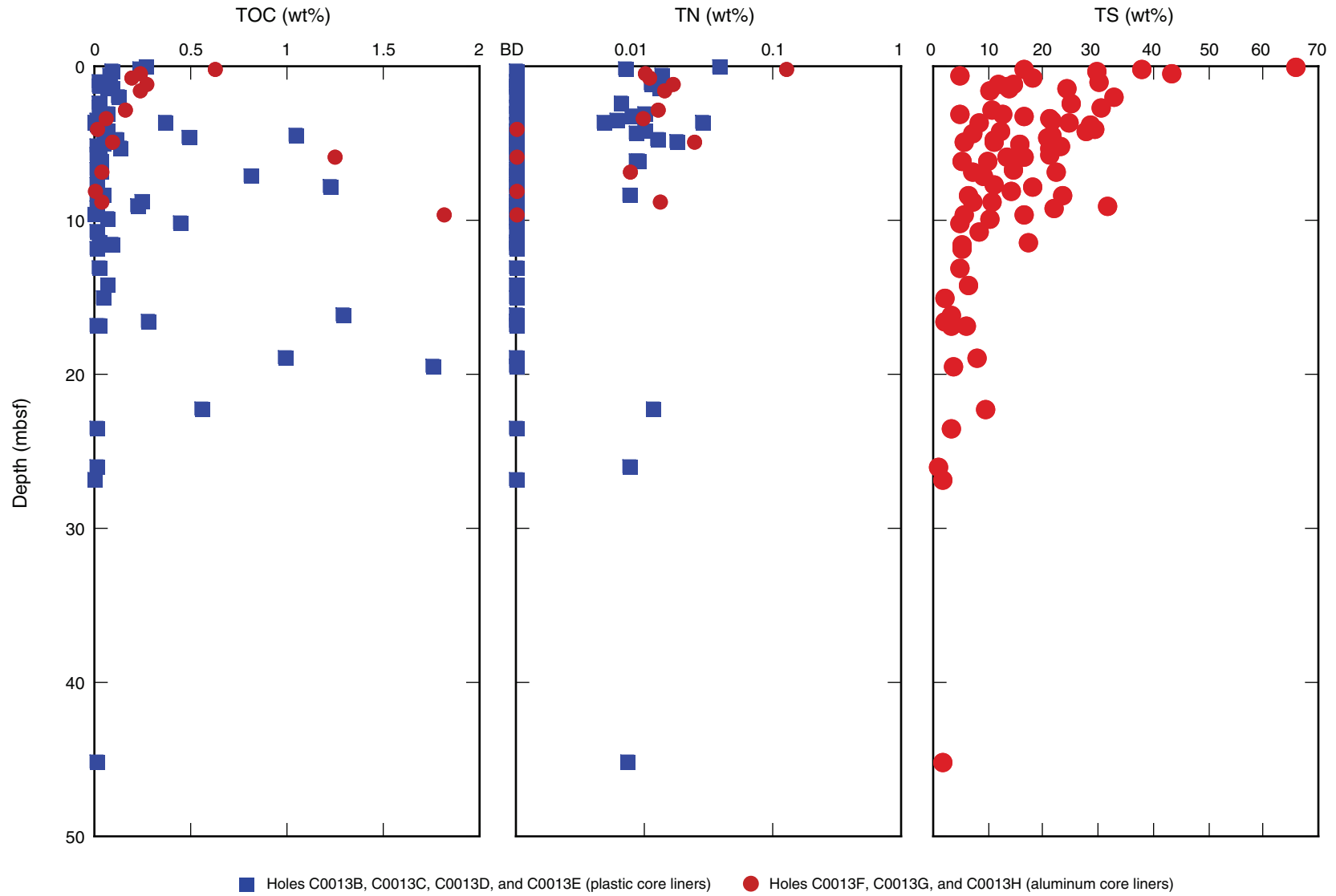


Figure F30. Plot of alkalinity, phosphate, and ammonium in pore water, Site C0013.





**Figure F31.** Total organic carbon (TOC), total nitrogen (TN), and total sulfur (TS) concentrations in sediments from Site C0013. **A.** TOC concentrations on a linear scale. **B.** TN concentrations on a log scale. **C.** TS concentrations on a linear scale.





**Figure F32.** Plot of hydrogen, methane (science gas samples on left and safety gas samples on right), and methane/ethane in headspace gas, Site C0013.

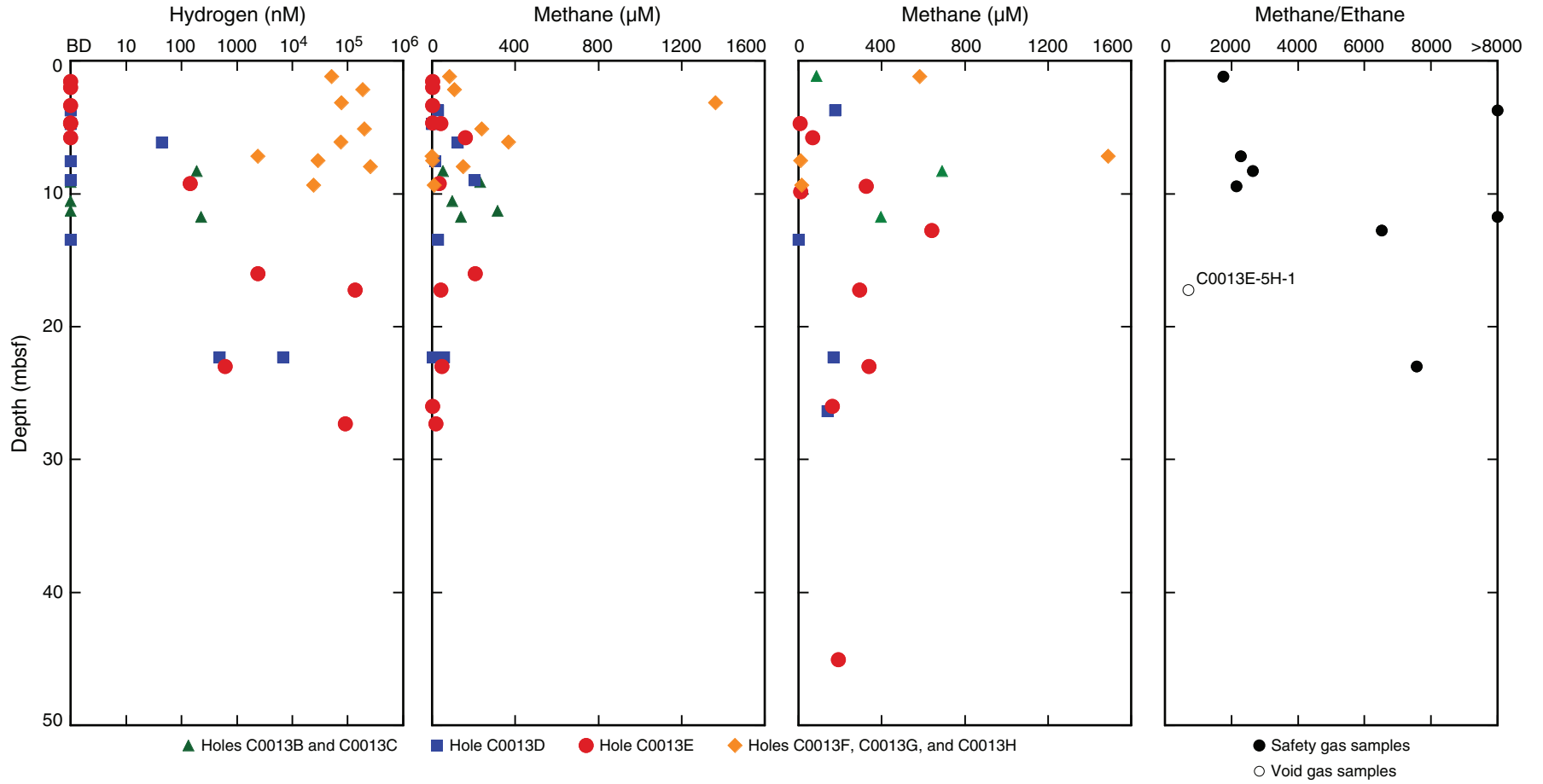


**Figure F33.** Plot of calcium carbonate ( $\text{CaCO}_3$ ) content of sediments calculated from inorganic carbon concentrations at Site C0013. All samples except three have  $<1\%$  wt%  $\text{CaCO}_3$ .

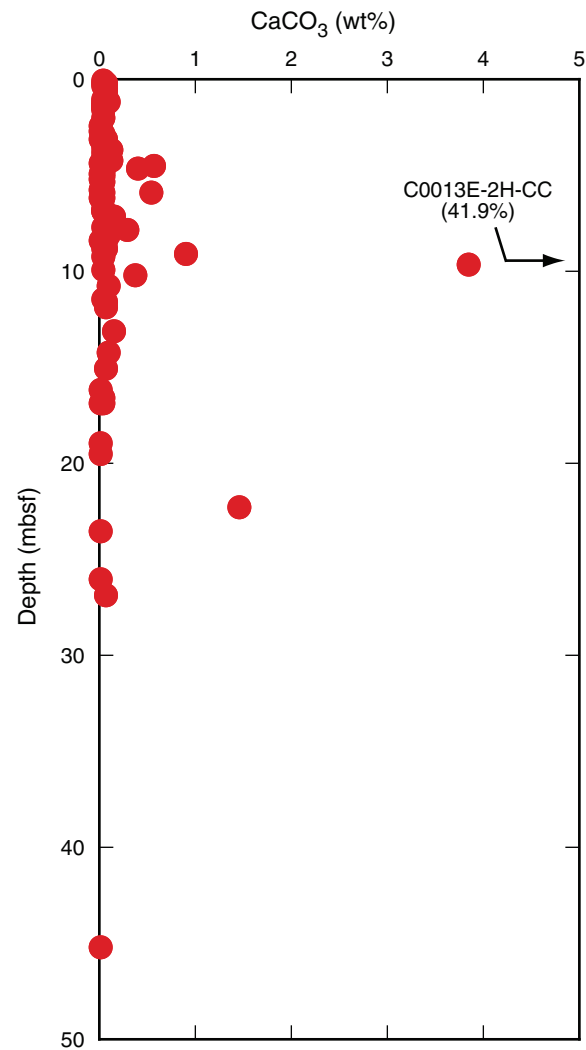


**Figure F34.** Plot of discrete measurements of bulk density (large solid symbols) and GRA-derived bulk density from the MSCL-W (small open symbols), Site C0013. GRA-derived bulk density values  $<0 \text{ g/cm}^3$  are omitted for clarity.

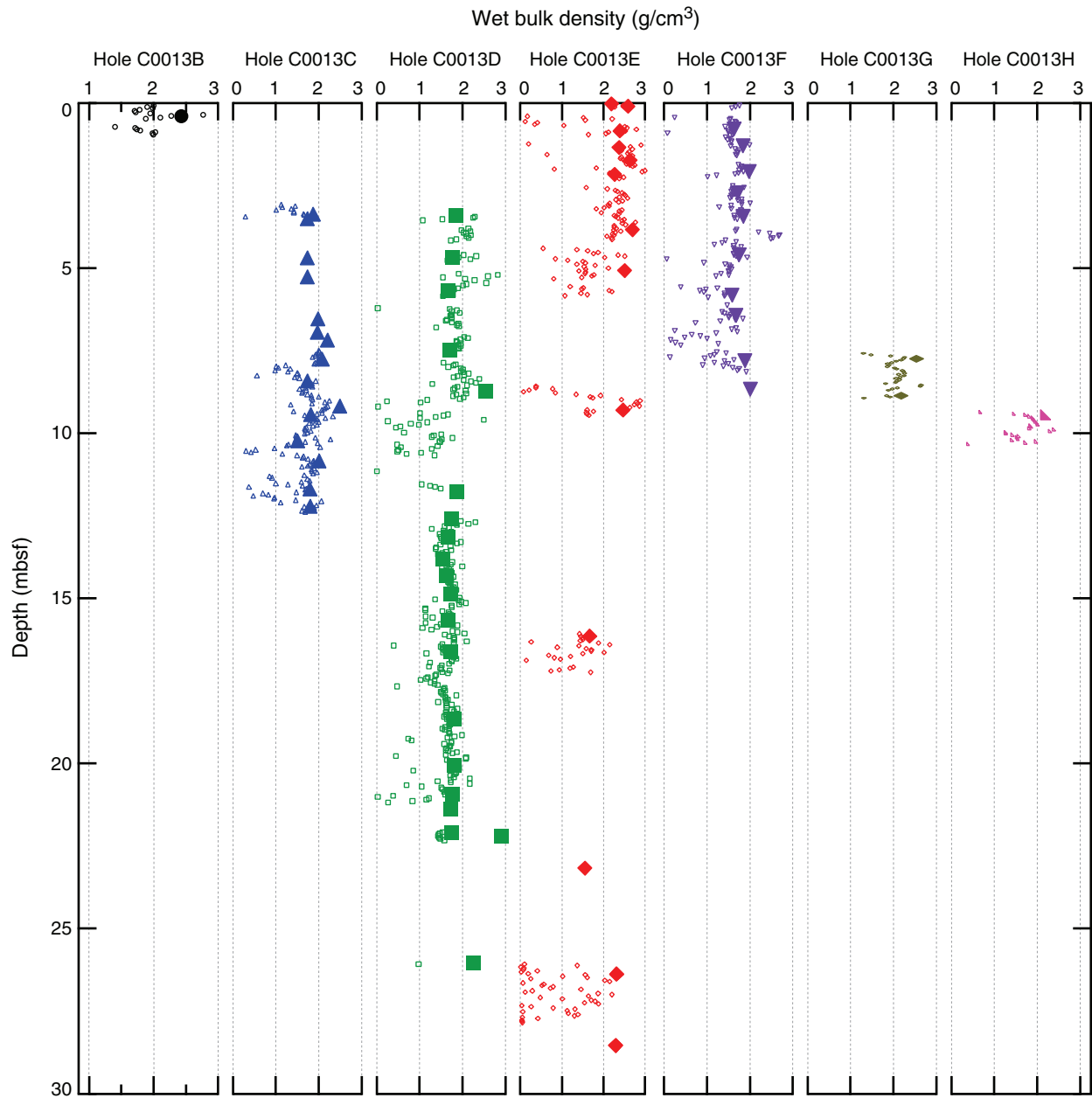
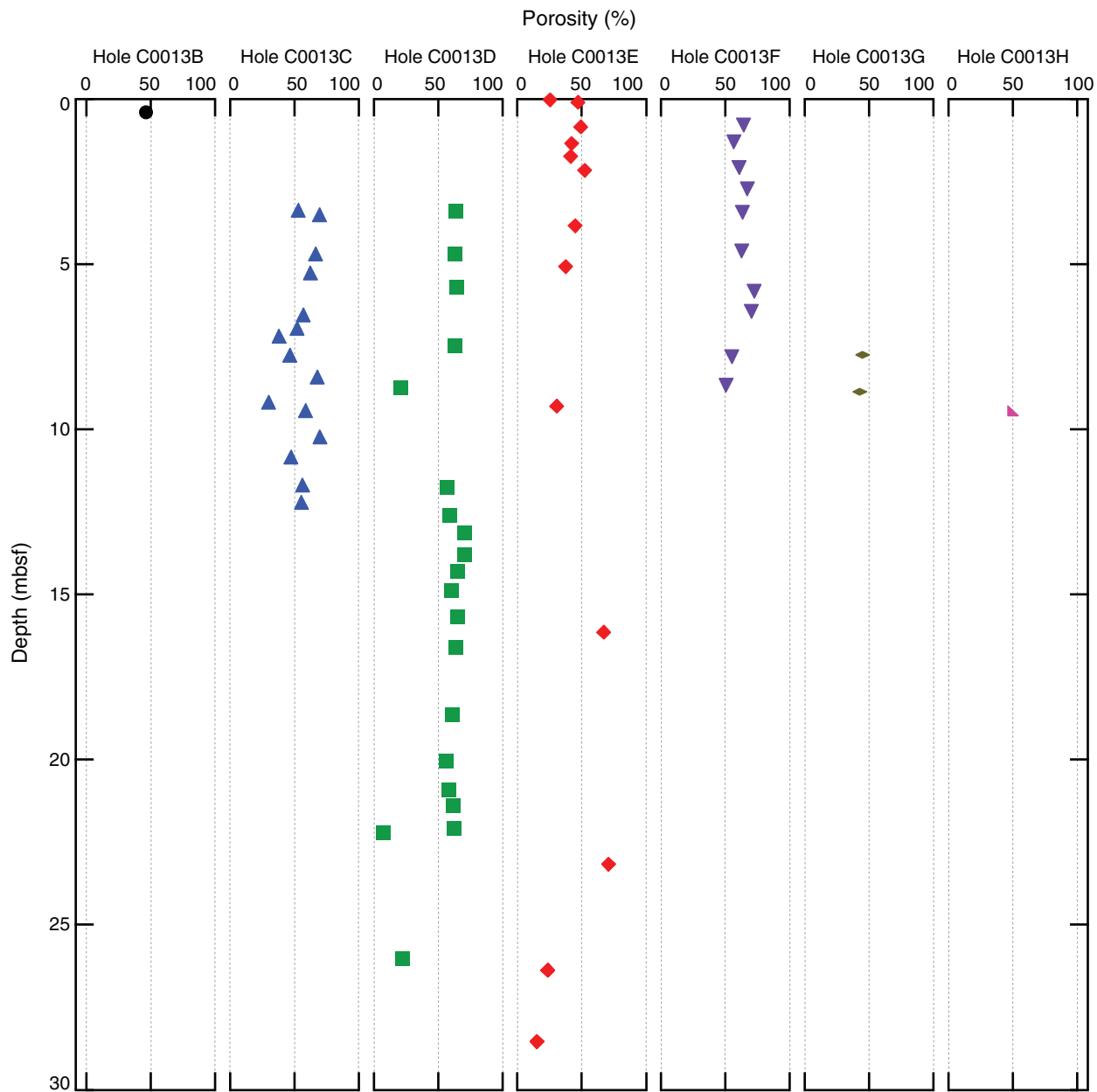


Figure F35. Plot of porosity calculated from discrete MAD measurements, Site C0013.



**Figure F36.** Comparison of physical properties parameters in Holes C0013C–C0013H. Density = wet bulk density (solid symbols) and grain density (open symbols). *P*-wave velocities are MSCL derived (lines). Thermal conductivity is shown as symbols. Dashed boxes represent the approximate extent of relatively dense layers with lithology different from the surrounding sediment, based on the presence of high bulk density, low porosity regions that also have increased thermal conductivity and *P*-wave velocities. Note the change in the *P*-wave velocity axis for Holes C0014F–C0014H. A. Hole C0013C. B. Hole C0013D. C. Hole C0013E. (Continued on next page.)

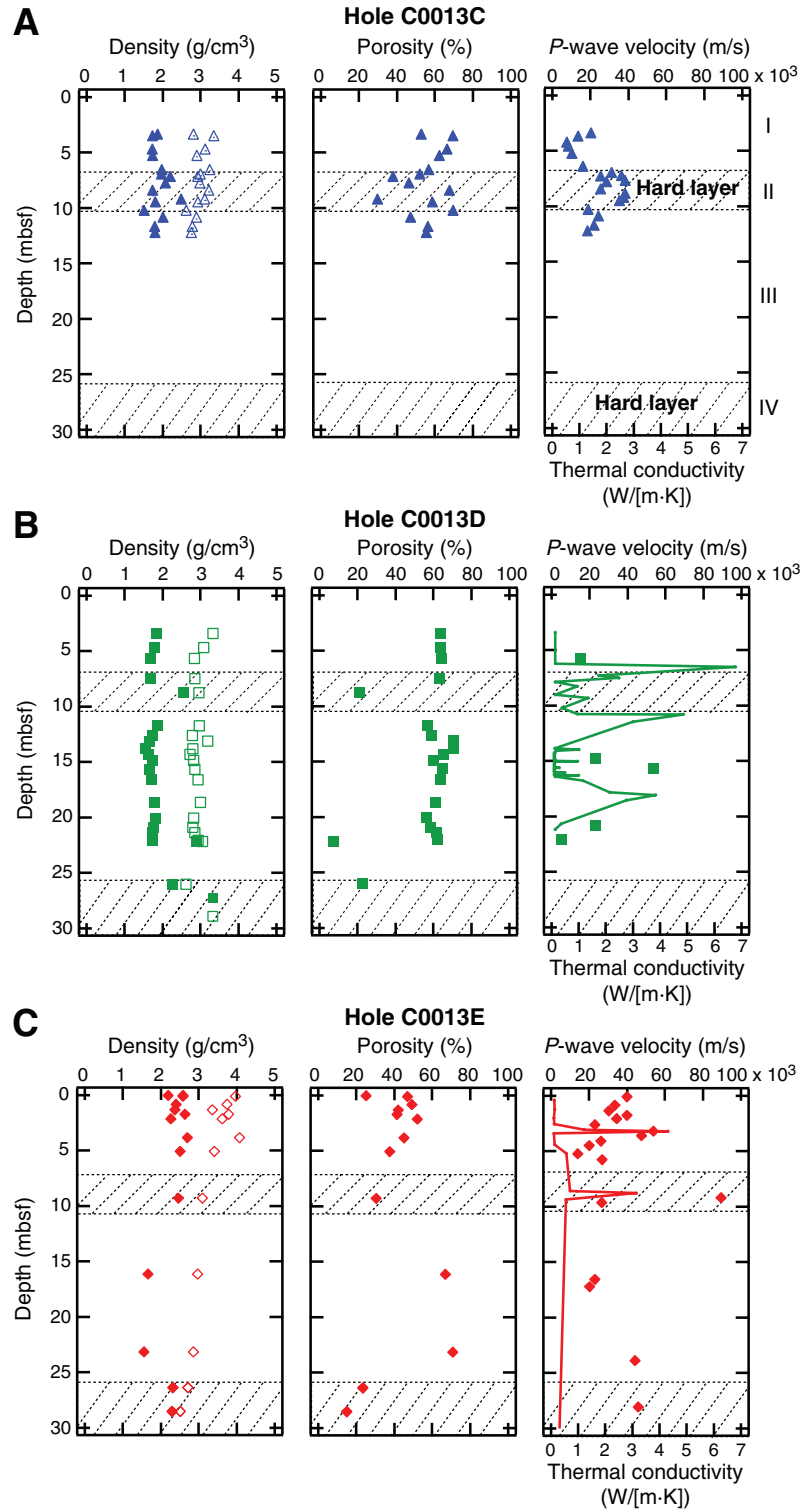


Figure F36 (continued). D. Hole C0013F. E. Hole C0013G. F. Hole C0013H.

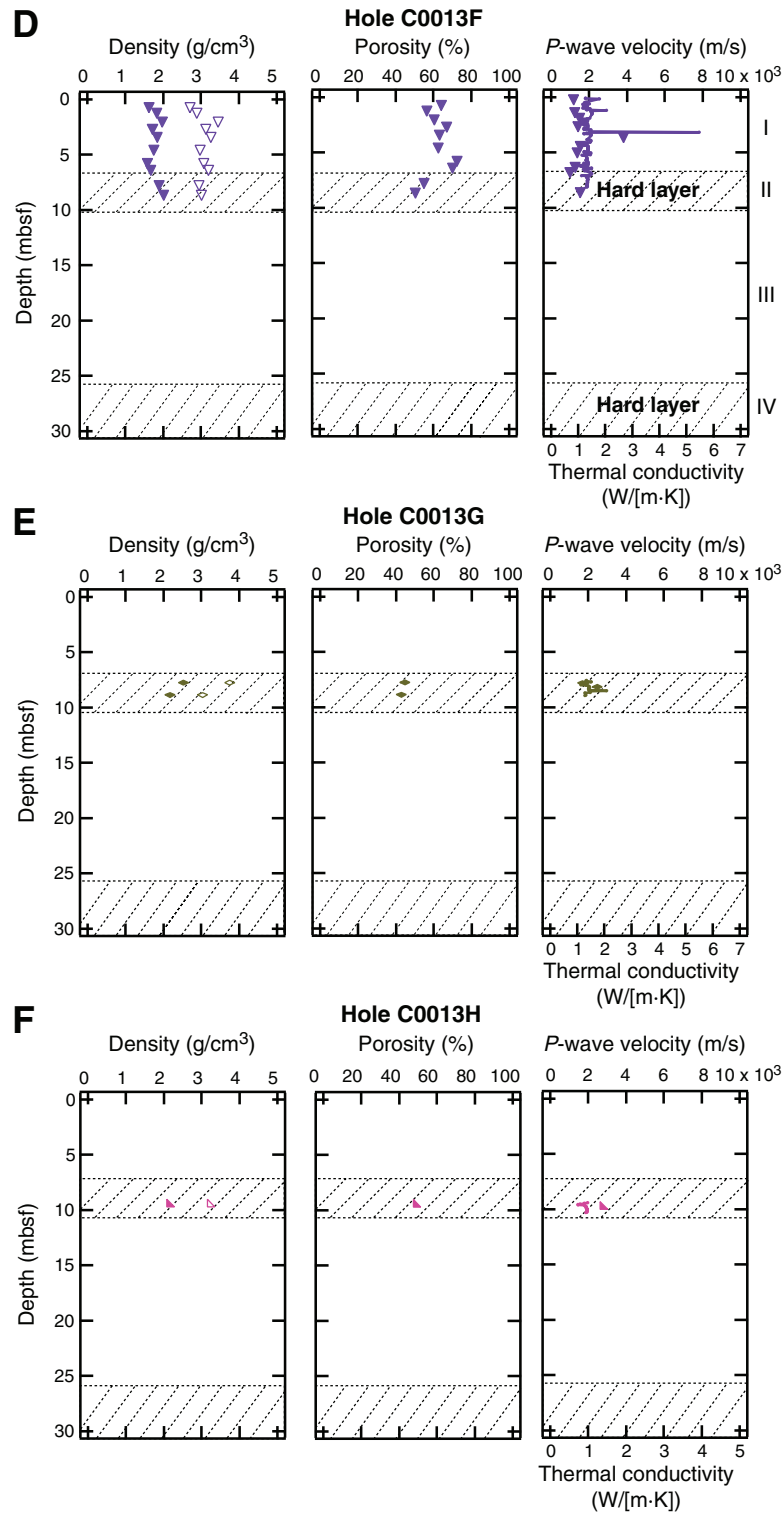


Figure F37. Plot of formation factor calculated from discrete electrical resistivity measurements, Site C0013.

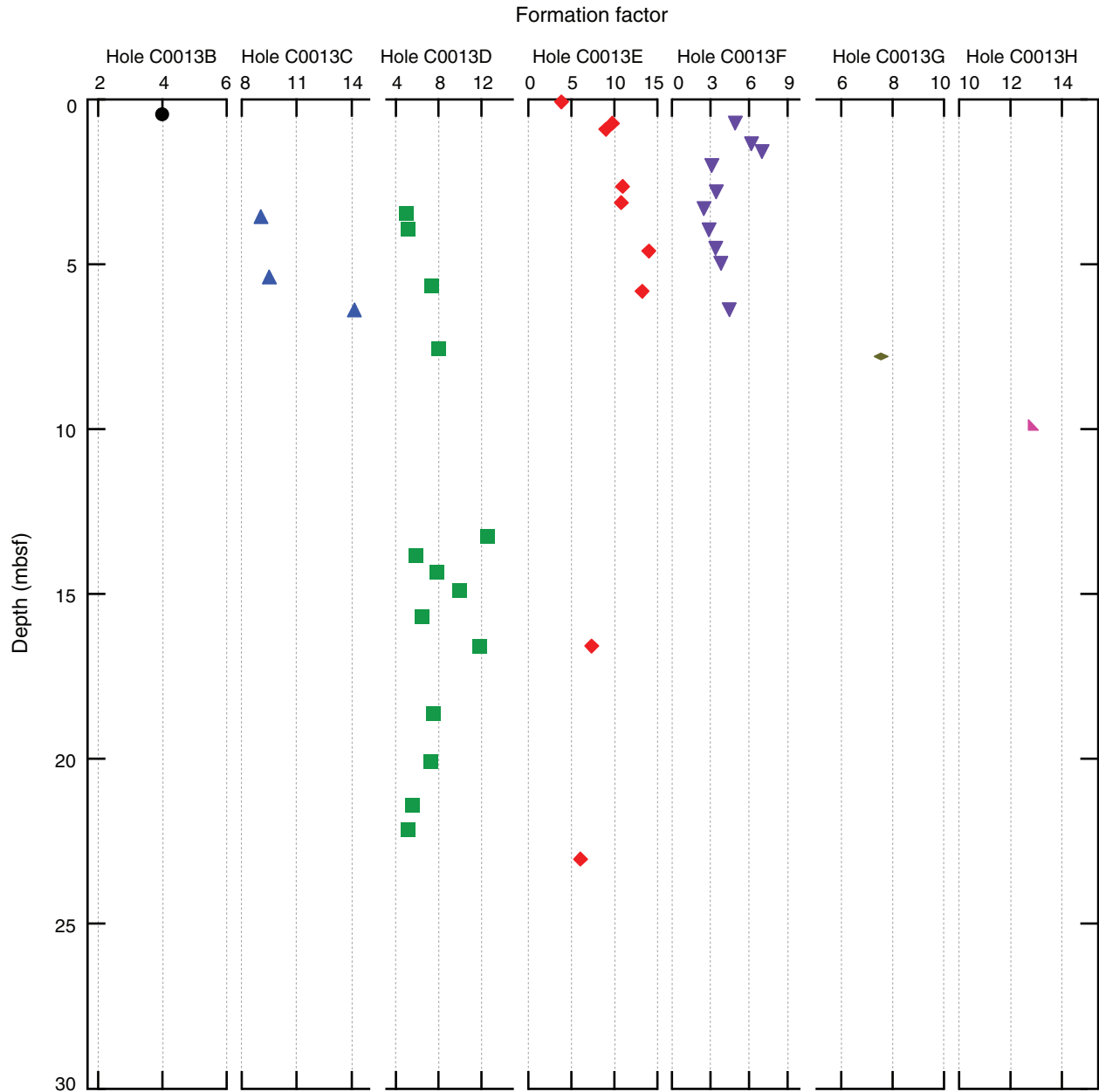
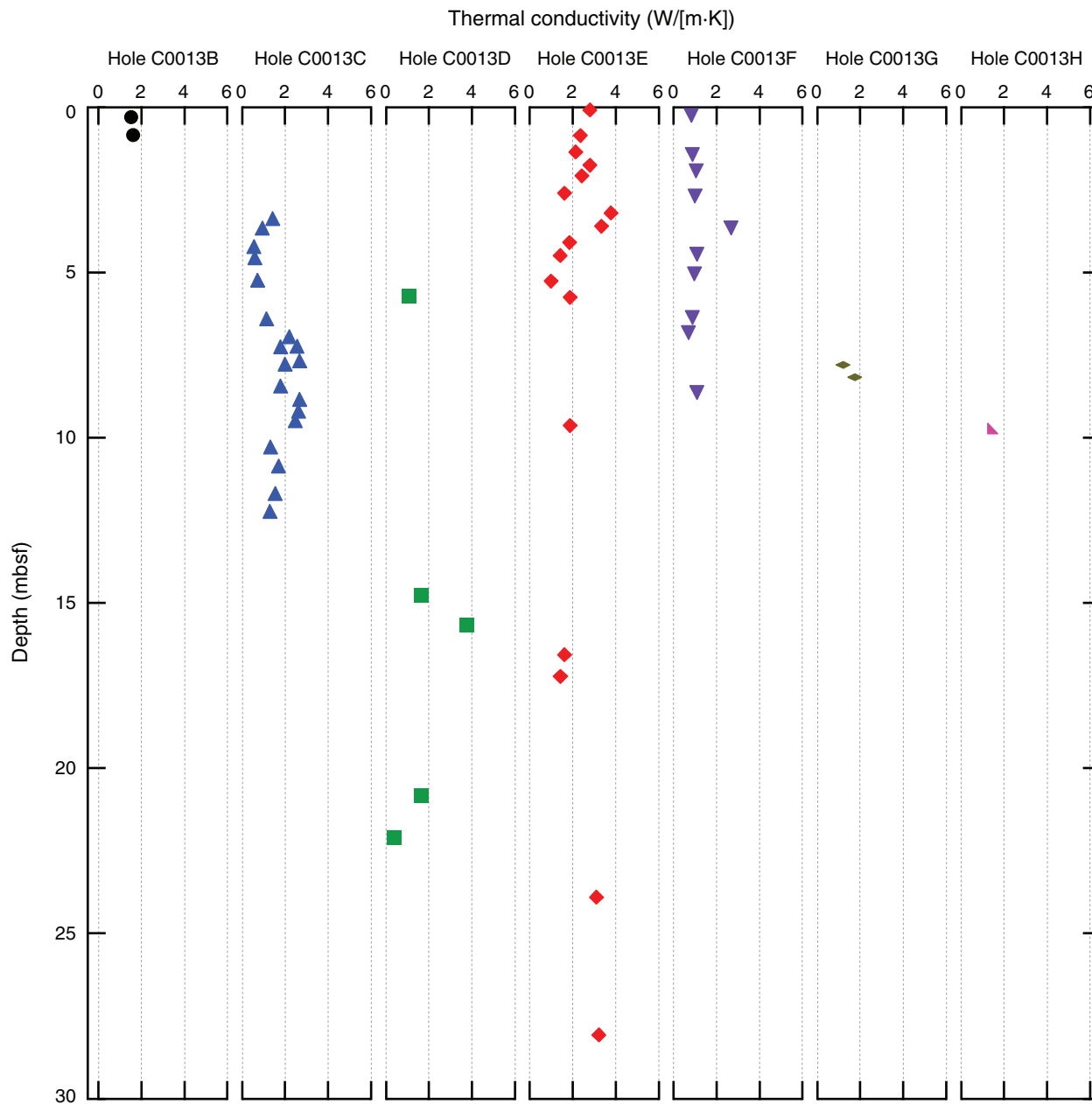


Figure F38. Plot of thermal conductivity, Site C0013.



**Figure F39.** Plot of MSCL-W derived electrical resistivity, Site C0013. No data exists for Holes C0013F–C0013H because of the use of aluminum core liners.

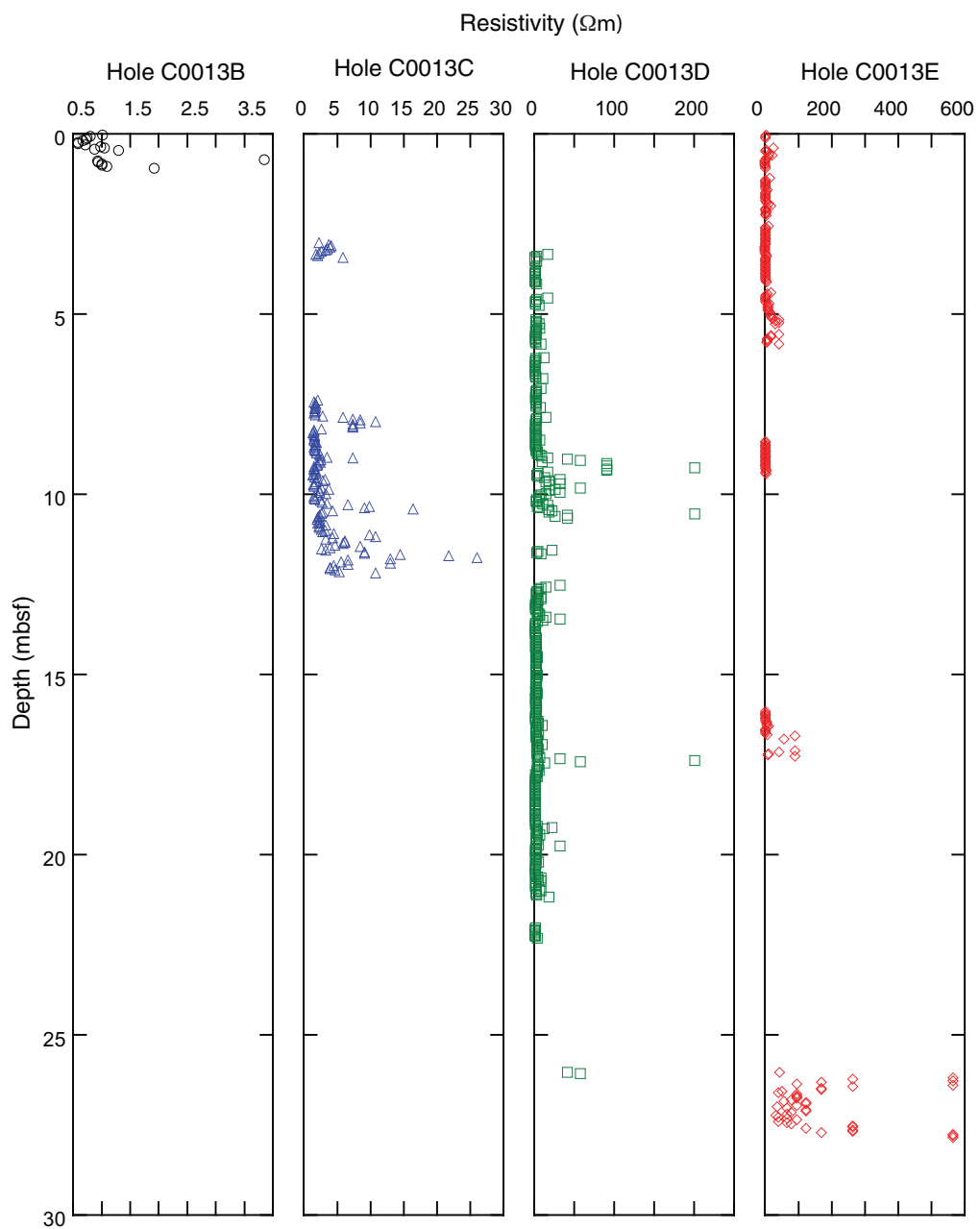


Table T1. Coring summary, Site C0013. (Continued on next two pages.)

**Site C0013**

Time on site (h): 113.5

**Hole C0013A**

Latitude: 27°47.4211'N

Longitude: 126°53.8533'E

Time on hole (h): 10.5 (0100 h, 10 September–1130 h, 10 September)

Seafloor depth (m DRF): 1063.5

Distance between rig floor and sea level (m): 28.5

Water depth (mbsl): 1035

Total depth (m DRF): 1070.5

Total penetration (mbsf): 7

Total length of cored section (m): 7

Total core recovered (m): 0

Core recovery: 0

Total number of cores: 0

**Hole C0013B**

Latitude: 27°47.4211'N

Longitude: 126°53.8533'E

Time on hole (h): 3 (2300 h, 10 September–0200 h, 11 September)

Seafloor depth (m DRF): 1064

Distance between rig floor and sea level (m): 28.5

Water depth (mbsl): 1035.5

Total depth (m DRF): 1073.5

Total penetration (mbsf): 9.5

Total length of cored section (m): 9.5

Total core recovered (m): 1.44

Core recovery: 15.2

Total number of cores: 1

**Hole C0013C**

Latitude: 27°47.4119'N

Longitude: 126°53.8606'E

Time on hole (h): 1 (0300 h, 11 September–0400, 11 September)

Seafloor depth (m DRF): 1063.5

Distance between rig floor and sea level (m): 28.5

Water depth (mbsl): 1035

Total depth (m DRF): 1076

Total penetration (mbsf): 12.5

Total length of cored section (m): 9.5

Total core recovered (m): 9.7

Core recovery: 102.1

Total number of cores: 1

**Hole C0013D**

Latitude: 27°47.4211'N

Longitude: 126°53.8533'E

Time on hole (h): 11.5 (0800 h, 11 September–1930 h, 11 September)

Seafloor depth (m DRF): 1065

Distance between rig floor and sea level (m): 28.3

Water depth (mbsl): 1036.5

Total depth (m DRF): 1100.5

Total penetration (mbsf): 35.5

Total length of cored section (m): 32.5

Total core recovered (m): 17.91

Core recovery: 50

Total number of cores: 4

**Hole C0013E**

Latitude: 27°47.4211'N

Longitude: 126°53.8533'E

Time on hole (h): 57 (0300 h, September 12–1200 h, September 14)

Seafloor depth (m DRF): 1062.5

Distance between rig floor and sea level (m): 28.5

Water depth (mbsl): 1034

Total depth (m DRF): 1117

Total penetration (mbsf): 54.5

Total length of cored section (m): 26

Total core recovered (m): 11.59

Core recovery: 35.41

Total number of cores: 9

Table T1 (continued). (Continued on next page.)

**Hole C0013F**

Latitude: 27°47.4122'N  
 Longitude 126°53.8601'E  
 Time on hole (h): 0.5 (1030 h, September 24–1100 h, September 24)  
 Seafloor depth (m DRF): 1063.6  
 Distance between rig floor and sea level (m): 28.5  
 Water depth (mbsl): 1035.1  
 Total depth (m DRF): 1071.1  
 Total penetration (mbsf): 7.5  
 Total length of cored section (m): 7.5  
 Total core recovered (m): 9.5  
 Core recovery: 126.7  
 Total number of cores: 1

**Hole C0013G**

Latitude: 27°47.4100'N  
 Longitude 126°53.8554'E  
 Time on hole (h): 1.5 (1200 h, September 24–13:30 h, September 24)  
 Seafloor depth (m DRF): 1063.6  
 Distance between rig floor and sea level (m): 28.5  
 Water depth (mbsl): 1035.1  
 Total depth (m DRF): 1072.9  
 Total penetration (mbsf): 9.3  
 Total length of cored section (m): 1.8  
 Total core recovered (m): 1.8  
 Core recovery: 100  
 Total number of cores: 1

**Hole C0013H**

Latitude: 27°47.4098'N  
 Longitude: 126°53.8565'E  
 Time on hole (h): 1 (1500 h, September 24–1600 h, September 24)  
 Seafloor depth (m DRF): 1063.6  
 Distance between rig floor and sea level (m): 28.5  
 Water depth (mbsl): 1035.1  
 Total depth (m DRF): 1073.5  
 Total penetration (mbsf): 9.9  
 Total length of cored section (m): 0.6  
 Total core recovered (m): 0.6  
 Core recovery: 100  
 Total number of cores: 1

Core	Date (2010)	Local time (h)	Depth DRF (m)		Depth (mbsf)		Advanced (m)	Recovered (m)	Recovery (%)
			Top	Bottom	Top	Bottom			
331-C0013A- 1H	10 Sep	1005	1063.5	1070.5	0	7	7	0	0
331-C0013B- 1T	10 Sep	2301	1064	1073.5	0	9.5	9.5	1.44	15.2
331-C0013C- 1H	11 Sep	0338	1066.5	1076	3	12.5	9.5	9.7	102.1
331-C0013D- 1H	11 Sep	0757	1068	1077.5	3	12.5	9.5	9.03	95.1
2H	11 Sep	1111	1077.5	1087	12.5	22	9.5	8	84.2
3T	11 Sep	1522	1087	1091	22	26	4	0.78	19.5
4X	11 Sep	1724	1091	1100.5	26	35.5	9.5	0.1	1.1
331-C0013E- 1H	12 Sep	0306	1062.5	1071	0	8.5	8.5	6.08	71.5
2H	12 Sep	0524	1071	1072.2	8.5	9.7	1.2	1.21	100.8
3X	12 Sep	0724	1072.2	1075.2	9.7	12.7	3	0.17	5.7
4X	12 Sep	0939	1075.2	1078.5	12.7	16	3.3	0.1	3
5H	12 Sep	1204	1078.5	1085.5	16	23	7	1.29	18.4
6X	12 Sep	1541	1085.5	1088.5	23	26	3	0.39	13
7L	13 Sep	0620	1088.5	1097.7	26	35.2	9.2	2.1	22.8
8X	14 Sep	0025	1097.7	1107.5	35.2	45	9.8	0	0
9X	14 Sep	0535	1107.5	1117	45	54.5	9.5	0.25	2.6
331-C0013F- 1H	24 Sep	1037	1063.6	1071.1	0	7.5	7.5	9.5	126.7
331-C0013G- 1H	24 Sep	1322	1071.1	1072.9	7.5	9.3	1.8	1.8	100

Table T1 (continued).

Core	Date (2010)	Local time (h)	Depth DRF (m)		Depth (mbsf)		Advanced (m)	Recovered (m)	Recovery (%)
			Top	Bottom	Top	Bottom			
331-C0013H-1H	24 Sep	1608	1072.9	1073.5	9.3	9.9	0.6	0.6	100

DRF = drilling depth below rig floor. H = HPCS, T = EPCS, X = ESCS, L = BHI.

Table T2. Lithostratigraphic units, Site C0013.

Lith. unit	Description	Hole, core, section, interval (cm)	Top depth (mbsf)	Bottom depth (mbsf)	Thickness (m)
I	Hydrothermally altered mud/clay, hydrothermal grit/gravel, metalliferous detrital sulfide	331-C0013B-1T-1, 0, to 1T-CC, 26	0.00	1.44	1.44
		C0013C-1H-1, 0, to 1H-5, 72	3.00	6.79	3.79
		C0013D-1H-1, 0, to 1H-3, 40	3.00	5.18	2.18
		C0013E-1H-1, 0, to 1H-5, 118	0.00	4.57	4.57
		C0013F-1H-1, 0, to 1H-8, 38	0.00	5.64	5.64
II	Hydrothermally altered mud, detrital metalliferous sulfide, anhydrite breccia	C0013C-1H-6, 0, to 1H-CC, 30	6.79	12.51	5.72
		C0013D-1H-3, 40, to 2H-1, 40	5.18	12.90	7.72
		C0013E-1H-5, 118, to 4X-CC, 4	4.57	12.74	8.17
		C0013F-1H-8, 38, to 1H-CC, 62	5.64	7.50	1.86
III	Hydrothermally altered mud, anhydrite nodules	C0013D-2H-1, 40, to 3T-CC, 45	12.90	22.79	9.80
		C0013E-5H-1, 0, to 6X-CC, 21	16.00	23.21	7.21
IV	Volcanic breccia	C0013D-4X-1, 0, to 4X-CC, 42.5	26.00	26.53	0.53
		C0013E-6X-CC, 21, to 9X-CC, 6.5	23.21	45.24	22.03

Table T3. Results of grain size distribution analysis, Hole C0013F.

Core, section, interval (cm)	Depth (mbsf)	Mean ( $\Phi$ )	Mean ( $\mu\text{m}$ )	SD ( $\Phi$ )	Sk	$K_G$	Clay (%)	Silt (%)	Sand (%)
331-C0013F-1H-2, 45–46	0.545	7.13	7.13	1.33	1.43	1.96	12.1	87.9	0
1H-3, 33–34	1.294	3.33	99.5	2.48	3.08	3.53	4.6	37.5	57.9
1H-4, 50–51	2.290	3.08	118.3	2.63	3.28	3.75	4.6	34.5	60.9
1H-5, 15–16	2.818	6.63	10.1	2.06	-0.83	2.59	13.6	73.7	12.7
1H-5, 90–91	3.456	2.94	129.9	2.68	3.33	3.8	3.9	35.3	60.8
1H-6, 80–81	4.222	4.17	55.5	2.68	3.15	3.54	7.8	44.8	47.4
1H-7, 60–61	4.912	2.89	135	2.43	3.08	3.57	3	34.5	62.5

SD = standard deviation, Sk = skewness,  $K_G$  = kurtosis.

**Table T4.** Dry mass and stereo light microscopic observations of micropaleontology samples, Site C0013.

Core, section, interval (cm)	Depth (mbsf)	Mass (g)			Comments
		>1 mm	150 µm to 1 mm	63–150 µm	
331-C0013A-		—	—	—	No core
331-C0013B- 1T-CC, 25.0–26.0	1.4	42.58	9.12	2.99	Centimeter-scale anhydrite clay clasts; very little material in <63 µm fraction
331-C0013C- 1H-CC, 19.0–20.0	12.6	1.96	6.39	7.81	White clay; very large <63 µm fraction
331-C0013D- 1H-CC, 37.5–38.5	12.1	8.84	8.45	3.55	Anhydrite white clay, large <63 µm fraction
2H-CC, 38.0–39.0	21.6	14.65	3.81	1.36	Anhydrite white clay glued with melted/resolidified plastic core liner
3T-CC, 43.0–44.5	22.8	20.46	8.47	2.03	Anhydrite white clay clasts; very little material in <63 µm fraction
4X-CC, 41.5–42.5	26.5	1.4	2.13	0.6	Sample possessed a weathered anhydrite white clay clast (mass = ~60 g)
331-C0013E- 1H-CC, 26.5–27.5	6.1	13.25	3.22	1.04	Centimeter-scale anhydrite white clay clasts; very little clay
2H-CC, 0.0–1.0	9.5	26.53	6.34	2.36	Anhydrite white clay with minor amount of adhered fines
3X-CC, 2.0–4.0	9.7	—	—	—	Anhydrite clast, mass = ~50 g (not processed)
4X-CC, 5.0–6.0	12.8	9.51	1.48	BD	Centimeter-scale anhydrite white clay clasts; very little material in <63 µm fraction
5H-CC, 0.0–1.0	17.3	33.25	0.6	0.07	Anhydrite white clay with minor amount of adhered fines
6X-CC, 0.0–1.0	23.0	12.52	5.39	1.44	Centimeter-scale anhydrite white clay clasts; very little material in <63 µm fraction
7L-CC, 74.5–75.5	28.6	—	—	—	Three unweathered pieces of basement rock, total mass = ~60 g (not processed)
8X-CC	—	—	—	—	Sample melted in core barrel
9X-CC, 16.0–17.0	45.2	12.82	5.37	1.9	Centimeter-scale anhydrite white clay clasts; very little material in <63 µm fraction
331-C0013F- 1H-CC, 61.5–62.5	8.8	22.05	5.94	2.46	White clay anhydrite, minor sphalerite
331-C0013G- 1H-CC, 24.5–25.5	9.2	34.45	7.03	0.43	Anhydrite, white clay, sphalerite, pyrite (washed sediment)
331-C0013H- 1H-CC, 10.0–11.0	10.5	39.44	0.44	BD	Washed sediment

— = no data. BD = below detection.



Table T5. Interpreted results of X-ray diffraction (XRD) analyses of samples, Site C0013. (Continued on next page.)

Sample number	Core, section, interval (cm)	Lithology	Subsampled for	Result
331-C0013B-				
29085	1T-1, 9–11	Bulk sample of clay and grit	Routine chemistry	Anhydrite, barite, muscovite
29088	1T-1, 25–26	White silty clay	XRD only—identification of phases	Kaolinite, woodhouseite ???, phosphorus sulfide ???, wurtzite/sphalerite
29089	1T-CC, 20–22	Bulk sample of clay and grit	Routine chemistry	Kaolinite, wurtzite/sphalerite, barite
331-C0013C-				
29143	1H-1, 2–4	Bulk sample of clay	Routine chemistry	Kaolinite, pyrite, wurtzite/sphalerite
29146	1H-1, 39–40	Gray clay and grit	XRD only—identification of phases	Kaolinite, pyrite, muscovite
29665	1H-2, 13–15	Dark brown silt	Routine chemistry	Muscovite, kaolinite, pyrite, barite
29668	1H-2, 83–85	Sulfidic grit	Routine chemistry	Barite, pyrite, wurtzite/sphalerite, kaolinite, vermiculite ???
29671	1H-4, 7–9	Pale gray clay altered volcanic clast	Routine chemistry	Illite/Muscovite, pyrite, galena, barite
29674	1H-5, 3–5	Bulk pale gray clay	Routine chemistry	Anhydrite, muscovite, vermiculite
29677	1H-5, 69–71	Clear euhedral crystal	XRD only—confirmation of VCD	Anhydrite
29679	1H-6, 16–18	Indurated dark gray clay	Routine chemistry	Anhydrite
29147	1H-11, 34–36	Bulk sample of clay and grit	Routine chemistry	Anhydrite, wurtzite/sphalerite, magnesite ???, galena
29152	1H-11, 74–75	Gray clay and grit	XRD only—identification of phases	Anhydrite, Mg chlorite, pyrite, galena
29153	1H-12, 7–9	White clay and grit	Routine chemistry	Mg chlorite, muscovite, wurtzite/sphalerite
29156	1H-12, 41–43	White clay	Routine chemistry	Anhydrite, Mg chlorite, muscovite, pyrite, wurtzite/sphalerite
29159	1H-13, 4–6	White clay and grit	Routine chemistry	Anhydrite, galena
29178	1H-13, 50–51	Clear euhedral mineral; anhydrite?	XRD only—confirmation of VCD	Anhydrite
29162	1H-13, 71–73	Horizon with brown layers	Routine chemistry	Anhydrite
29172	1H-13, 101–102	White anhydrite-silica-carbonate clast	XRD of TS sample 29173	Anhydrite, talc (10, dolomite)
29166	1H-14, 14–16	Clay-white opaque material	Routine chemistry	Anhydrite, quartz, Mg chlorite
29171	1H-15, 10–12	Clay-white material with small translucent anhydrite	Routine chemistry	Anhydrite, talc, quartz
29177	1H-16, 5–7	Clay-white/gray material	Routine chemistry	Anhydrite, Mg chlorite, pyrite
29179	1H-CC, 23–24	White anhydrite-silica-carbonate clast	XRD only—identification of phases	Anhydrite, dolomite, talc
331-C0013D-				
29222	1H-1, 45–47	Bulk gray clay and grit	Routine chemistry	Wurtzite/Sphalerite, galena, muscovite
29225	1H-2, 86–88	Bulk dark gray sulfidic clay and grit	Routine chemistry	Anhydrite, wurtzite/sphalerite
29228	1H-3, 42–44	Anhydrite vein	Routine chemistry	Anhydrite, galena, wurtzite/sphalerite
29231	1H-3, 82–83	Dark brown clay	XRD only	Anhydrite, pyrite, galena, muscovite
29232	1H-4, 50–52	Bulk pale gray clay	Routine chemistry	Anhydrite
29235	1H-5, 72–74	White anhydrite-silica-carbonate vein	Routine chemistry	Anhydrite
29238	1H-6, 110–112	Soft pale gray clay	Routine chemistry	Mg chlorite, anhydrite, pyrite
29241	1H-7, 126–128	Soft pale gray clay	Routine chemistry	Noncrystalline phases, quartz, pyrophyllite ???
29273	2H-1, 54–56	Bulk clay	Routine chemistry	Mg chlorite, pyrite
29276	2H-2, 64–66	Bulk clay	Routine chemistry	Mg chlorite, anhydrite, pyrite
29279	2H-3, 55–57	White anhydrite-silica-carbonate clast	Routine chemistry	Talc, anhydrite, quartz
29282	2H-4, 65–67	Bulk clay	Routine chemistry	Mg chlorite, anhydrite, pyrite
29285	2H-5, 5–7	Blue-white mottled clay	Routine chemistry	Mg chlorite
29288	2H-6, 104–106	Bulk clay	Routine chemistry	Mg chlorite, anhydrite, pyrite, calcite
29291	2H-7, 26–28	Blue-white mottled clay	Routine chemistry	Mg chlorite, pyrite, pyrrhotite ???
29459	3T-1, 18–20	Hydrothermal sand—redrill	Routine chemistry	Anhydrite, Mg chlorite, rest of material possibly magnesite, calcite, barite
29462	4X-1, 0–2	Silicified volcanic breccia	Routine chemistry	Quartz, muscovite, Mg chlorite
331-C0013E-				
29482	1H-1, 2–4	Native sulfur and clay	Routine chemistry	Sulfur, barite, quartz
29485	1H-2, 124–126	Sulfidic grit	Routine chemistry	Wurtzite/Sphalerite, barite, quartz
29491	1H-3, 40.5–42.5	Sulfidic grit	Routine chemistry	Wurtzite/Sphalerite, galena, pyrite
29488	1H-4, 68–70	Clay	Routine chemistry	Wurtzite/Sphalerite, pyrite
29494	1H-4, 116–117	Massive sulfide sediment	XRD only—sulfide mineralogy	Wurtzite/Sphalerite, pyrite, anhydrite



Table T5 (continued).

Sample number	Core, section, interval (cm)	Lithology	Subsampled for	Result
29495	1H-5, 41–43	Sulfidic grit	Routine chemistry	Lithium aluminous silicate ???, wurtzite
29498	1H-6, 99–101	White anhydrite-silica-carbonate clast	Routine chemistry	Anhydrite, wurtzite, Mg chlorite
29613	2H-1, 58–60	Sulfidic grit	Routine chemistry	Wurtzite/Sphalerite, anhydrite, galena, barite
29616	2H-CC, 5–7	Silica-carbonate-sulfate vein	Routine chemistry	Anhydrite, calcite, dolomite, talc
29619	3X-CC, 6–7	Silica-carbonate-sulfate vein	XRD only—silica-sulfate-carbonate vein	Anhydrite, magnesite
29620	5H-1, 21–23	Soft pale gritty clay	XRD only—identification of phases	Mg chlorite, anhydrite, pyrite
29621	5H-1, 82–84	Indurated mottled clay	Routine chemistry	Anhydrite, Mg chlorite, talc, pyrite
29624	6X-CC, 43–45	Silicified volcanic breccia	Routine chemistry	Quartz, anhydrite, Mg chlorite, hematite ?????
29696	7L-2, 43–46	Silicified volcanic breccia	Routine chemistry	Quartz, anhydrite, Mg chlorite, muscovite
29708	9X-CC, 8–10	Mud from core catcher	Routine chemistry	Quartz, Mg chlorite, muscovite, anhydrite
331-C0013F-				
34624	1H-1, 5–6	Sulfur cap	XRD only—mineralogy	Sulfur, barite
34622	1H-1, 11–13	Matrix mud/clay	Routine chemistry	Barite, sulfur, sphalerite/wurtzite, covellite (trace)
34625	1H-2, 30–32	Gray mud matrix	Routine chemistry	Kaolinite, sulfur, barite, sphalerite/wurtzite
34722	1H-2, 57–59	Indurated gray hydrothermal clay	Routine chemistry	Kaolinite, pyrite, sulfur, muscovite, sphalerite/wurtzite
34725	1H-2, 92–94	Soupy gray hydrothermal clay	Routine chemistry	Kaolinite, sphalerite/wurtzite, pyrite, muscovite, galena, cosalite (Pb <sub>2</sub> Bi <sub>2</sub> S <sub>5</sub> )
34728	1H-3, 7–9	Hydrothermal clay with native S	Routine chemistry	Sphalerite/Wurtzite, pyrite, galena, kaolinite
34726	1H-3, 28.5–30.5	Dark gray hydrothermal clay	Routine chemistry	Sphalerite/Wurtzite, pyrite, galena, kaolinite, muscovite/illite/montmorillonite
34729	1H-4, 62–64	Dark gray hydrothermal clay	Routine chemistry	Sphalerite/Wurtzite, pyrite, galena, muscovite
34731	1H-5, 18–20	Gray hydrothermal clay	Routine chemistry	Sphalerite/Wurtzite, pyrite, galena, anhydrite, muscovite
34734	1H-5, 86–88	Sulfidic grit	Routine chemistry	Sphalerite/Wurtzite, anhydrite, galena, pyrite
34735	1H-6, 74–76	Gray hydrothermal clay	Routine chemistry	Sphalerite/Wurtzite, covellite, pyrite, galena, muscovite
34738	1H-7, 62–64	Gray hydrothermal clay	Routine chemistry	Anhydrite, magnesite, sphalerite/wurtzite, Mg chlorite, pyrite, galena
34739	1H-8, 65–67	Gray hydrothermal clay—white mottling	Routine chemistry	Sphalerite/Wurtzite, anhydrite, pyrite, covellite, galena
34742	1H-9, 94–96	Bulk light gray gravel and anhydrite crystals	Routine chemistry	Anhydrite, pyrite
331-C0013G-				
34789	1H-2, 74–76	Redrill—hydrothermal gravel	Routine chemistry	Anhydrite, sphalerite/wurtzite, muscovite, pyrite, galena, halite
331-C0013H-				
34791	1H-2, 21–23	Redrill—grit, hydrothermal clay, anhydrite, and sulfides	Routine chemistry	Anhydrite, magnesite, dolomite, barite, sphalerite/wurtzite, galena

Phases listed in approximate order of decreasing abundance. VCD = visual core description, TS = thin section.

Table T6. Composition of interstitial pore water, Site C0013. This table is available in an [oversized format](#).

Table T7. Concentrations of hydrocarbons observed in safety gas vials, Site C0013.

Hole, core, section, interval (cm)	Depth (mbsf)	CH <sub>4</sub> in headspace (ppm)	C <sub>2</sub> H <sub>6</sub> in headspace (ppm)	C <sub>3</sub> H <sub>8</sub> in headspace (ppm)	Butane, ethylene, and/or propylene (Y or N)	Sediment mass (g)	CH <sub>4</sub> in pore water (μM)	C <sub>2</sub> H <sub>6</sub> in pore water (μM)
331-								
C0013B-1T-1, 114-118	1.14	117.9	BD	BD	N	5.044	86.2	BD
C0013F-1H-3, 0-4	1.19	1466.0	0.8	BD	N	5.473	583.2	0.3
C0013D-1H-1, 73.5-77.5	3.74	507.4	BD	BD	N	5.631	174.9	BD
C0013E-1H-6, 0-4	4.71	10.6	BD	BD	N	5.779	8.5	BD
C0013E-1H-6, 109.5-113.5	5.80	115.7	BD	BD	N	7.538	68.5	BD
C0013F-1H-9, 0-4	7.18	1177.2	0.5	BD	Y	2.017	1491.8	0.7
C0013G-1H-1, 0-4	7.50	16.8	BD	BD	N	6.610	9.8	BD
C0013C-1H-12, 0-4	8.28	2075.3	0.8	BD	N	5.144	691.5	0.3
C0013H-1H-2, 0-4	9.36	51.0	BD	BD	N	9.235	15.0	BD
C0013E-2H-1, 95.5-99.5	9.46	407.1	0.2	BD	N	6.838	326.4	0.2
C0013E-3X-CC, 14.5-18.5	9.85	37.5	BD	BD	N	9.488	11.1	BD
C0013C-1H-15, 42-46	11.76	830.5	BD	BD	N	4.583	396.8	BD
C0013E-4X-CC, 7-11	12.77	3187.7	0.5	BD	Y	8.117	640.9	0.1
C0013D-2H-1, 98-102	13.48	4.1	BD	BD	N	11.854	0.4	BD
C0013E-5H-1, 124.5-128.5	17.25	745.1	1.1	0.7	Y	4.336	293.0	0.4
C0013D-3T-1, 29.5-33.5	22.30	11.7	BD	BD	N	2.117	166.7	BD
C0013E-6X-CC, 0-4	23.00	1372.7	0.2	BD	N	5.734	338.1	BD
C0013E-7L-1, 0-4	26.00	169.5	1.1	0.4	Y	6.835	163.8	1.1
C0013D-4X-CC, 25-29	26.36	140.8	BD	BD	N	6.774	139.1	BD
C0013E-9X-CC, 0-4	45.07	145.5	BD	BD	N	7.636	190.0	BD

BD = below detection.

Table T8. Concentrations of H<sub>2</sub> and CH<sub>4</sub> in science gas, Site C0013.

Core, section, interval (cm)	Depth (mbsf)	H <sub>2</sub> in headspace (ppm)	CH <sub>4</sub> in headspace (ppm)	Sediment mass (g)	H <sub>2</sub> in pore water (nM)	CH <sub>4</sub> in pore water (μM)
331-C0013B-1T-1, 114–118	1.14	BD	39.61	—	—	—
331-C0013C-1H-12, 0–4	8.28	1.4	403.07	5.549	189	52.6
1H-13, 0–4	9.13	BD	315.27	4.163	BD	229.5
1H-13, 142–146	10.55	BD	251.34	2.053	BD	96.1
1H-14, 71–75	11.30	BD	284.54	1.469	BD	314.7
1H-15, 42–46	11.76	1.5	923.63	6.040	225	138.2
331-C0013D-1H-1, 73.5–77.5	3.74	BD	243.58	7.531	BD	28.5
1H-2, 96.5–100.5	4.74	BD	6.87	7.230	BD	0.8
1H-3, 138.5–142	6.17	0.6	1,565.21	8.126	44	122.2
1H-4, 136–140	7.57	BD	121.05	5.959	BD	14.5
1H-5, 137.5–141.5	8.99	BD	345.16	5.813	BD	204.0
1H-6, 121–125	10.24	BD	243.58	6.570	BD	—
2H-1, 98–102	13.48	BD	243.38	5.494	BD	27.5
3T-1, 29.5–33.5	22.30	54.4	467.59	7.698	6,821	58.6
3T-CC, 41.5–45.5	22.30	1.4	5.31	6.829	495	1.9
4X-CC, 25–29	26.36	8.5	16.31	5.580	—	—
331-C0013E-1H-2, 137–141	1.53	BD	6.87	8.562	BD	1.2
1H-3, 43–43.5	2.00	BD	7.90	10.270	BD	1.1
1H-4, 134.5–138.5	3.35	BD	10.26	9.790	BD	1.0
1H-5, 127.5–131.5	4.67	BD	7.79	9.953	BD	1.1
1H-6, 0–4	4.71	BD	148.65	6.835	BD	41.1
1H-6, 109.5–113.5	5.80	BD	450.94	5.377	BD	158.6
2H-1, 74.5–76.5	9.25	BD	171.82	10.609	143	34.5
3X-CC, 14–18.5	9.85	2.3	288.32	4.300	—	—
4X-CC, 7–11	12.77	16.3	1,019.97	5.218	—	—
5H-1, 0–4	16.00	13.9	1,211.07	4.409	2,377	207.3
5H-1, 124.5–128.5	17.25	1,485.8	450.38	6.018	137,925	41.8
6X-CC, 0–4	23.00	5.5	424.30	5.982	612	47.3
7L-1, 0–4	26.00	1,506.9	BD	2.715	—	BD
7L-2, 95.5–99.5	27.30	149.8	28.46	5.244	90,738	17.2
331-C0013F-1H-3, 0–4	1.19	339.6	540.9	6.028	51,894.2	82.6
1H-4, 0–4	2.19	857.9	479.6	3.975	189,742.6	106.1
1H-5, 0–4	3.16	482.4	8,430.0	5.820	78,032.6	1,363.6
1H-6, 97–101	5.13	987.2	1,168.3	4.701	201,442.0	238.4
1H-7, 96.5–100.5	6.13	413.0	1,982.6	4.059	76,529.7	367.4
1H-9, 0–4	7.18	9.9	BD	4.054	2,381.3	BD
331-C0013G-1H-1, 0–4	7.50	136.0	7.6	6.898	29,357.0	1.6
1H-2, 0–4	7.97	998.3	578.7	6.305	259,821.1	150.6
331-C0013H-1H-2, 0–4	9.36	170.0	70.8	8.181	24,090.9	10.0

BD = below detection. — = no data.

Table T9. Carbon, nitrogen, and sulfur contents of sediments, Site C0013. (Continued on next page.)

Core, section, interval (cm)	Depth (mbsf)	IC (wt%)	CaCO <sub>3</sub> (wt%)	TN (wt%)	TC (wt%)	TS (wt%)	TOC (wt%)	TOC/TN
331-C0013B-								
1T-1, 9.0–11.0	0.09	0.003	0.027	0.007	0.242	16.214	0.239	33.861
1T-1, 50.0–60.0	0.50	0.008	0.066	0.014	0.081	4.647	0.074	5.414
1T-1, 108.0–118.0	1.08	0.002	0.019	0.011	0.033	14.342	0.031	2.719
1T-CC, 20.0–22.0	1.38	0.004	0.034	0.013	0.067	13.726	0.063	4.693
1T-CC, 12.0–20.0	1.30	0.004	0.032	BD	0.031	13.077	0.027	NA
331-C0013C-								
1H-1, 2.0–4.0	3.02	0.001	0.006	BD	0.063	4.753	0.063	NA
1H-2, 13.0–15.0	3.58	0.013	0.112	0.029	0.375	8.079	0.362	12.572
1H-2, 83.0–85.0	4.28	BD	BD	0.009	0.072	7.164	0.072	8.366
1H-4, 7.0–9.0	4.81	BD	0.004	0.018	0.062	5.483	0.062	3.458
1H-5, 3.0–5.0	6.18	0.001	0.011	0.009	0.027	9.845	0.025	2.890
1H-6, 16.0–18.0	7.03	0.017	0.138	BD	0.827	9.039	0.810	NA
1H-11, 34.0–36.0	7.81	0.033	0.272	BD	1.254	17.758	1.222	NA
1H-12, 7.0–9.0	8.35	0.001	0.008	0.008	0.048	6.187	0.047	6.089
1H-12, 41.0–43.0	8.69	0.002	0.018	BD	0.244	6.954	0.242	NA
1H-13, 4.0–6.0	9.17	0.002	0.020	BD	0.015	21.943	0.013	NA
1H-13, 71.0–73.0	9.84	0.005	0.038	BD	0.076	10.319	0.072	NA
1H-14, 14.0–16.0	10.73	0.009	0.078	BD	0.020	8.072	0.011	NA
1H-15, 10.0–12.0	11.44	0.005	0.038	BD	0.026	17.184	0.022	NA
1H-16, 5.0–7.0	11.85	0.006	0.046	BD	0.018	5.262	0.013	NA
331-C0013D-								
1H-1, 0.0–9.5	3	0.008	0.068	0.010	0.056	12.443	0.048	4.795
1H-1, 19.0–29.0	3.19	0.006	0.047	0.008	0.040	16.173	0.034	4.382
1H-1, 45.0–47.0	3.45	0.002	0.015	0.006	0.016	21.253	0.014	2.334
1H-1, 57.0–67.0	3.57	0.009	0.074	0.005	0.013	24.356	0.004	0.821
1H-2, 41.0–53.0	4.185	0.013	0.112	BD	0.075	27.689	0.062	NA
1H-2, 68.0–80.0	4.455	0.065	0.544	BD	1.106	21.471	1.041	NA
1H-2, 86.0–88.0	4.635	0.048	0.401	BD	0.537	20.716	0.489	NA
1H-3, 0.0–10.0	4.78	0.005	0.039	0.013	0.119	10.844	0.114	9.117
1H-3, 25.0–35.0	5.03	0.003	0.029	BD	0.045	15.600	0.042	NA
1H-3, 42.0–44.0	5.2	0.002	0.013	BD	0.012	22.965	0.010	NA
1H-3, 107.5–117.5	5.855	0.004	0.034	BD	0.022	16.535	0.018	NA
1H-3, 132.5–142.5	6.105	0.003	0.021	0.009	0.035	5.156	0.032	3.581
1H-4, 50.0–52.0	6.705	0.003	0.024	BD	0.019	14.259	0.016	NA
1H-4, 60.0–70.0	6.805	0.003	0.023	BD	0.035	6.909	0.032	NA
1H-5, 0.0–10.0	7.615	0.003	0.025	BD	0.020	11.001	0.017	NA
1H-5, 72.0–74.0	8.335	0.007	0.059	BD	0.014	23.339	0.007	NA
1H-6, 110.0–112.0	10.13	0.043	0.356	BD	0.490	4.637	0.447	NA
1H-7, 126.0–128.0	11.54	0.007	0.059	BD	0.091	5.181	0.084	NA
2H-1, 54.0–56.0	13.04	0.018	0.149	BD	0.039	4.554	0.021	NA
2H-2, 64.0–66.0	14.16	0.009	0.079	BD	0.072	6.228	0.063	NA
2H-3, 55.0–57.0	15.07	0.005	0.045	BD	0.045	1.853	0.040	NA
2H-4, 65.0–67.0	16.18	0.001	0.007	BD	1.289	3.234	1.288	NA
2H-5, 5.0–7.0	16.475	0.005	0.040	BD	0.281	2.091	0.277	NA
2H-6, 104.0–106.0	18.87	0.001	0.010	BD	0.988	7.703	0.987	NA
2H-7, 26.0–28.0	19.5	0.002	0.014	BD	1.759	3.409	1.757	NA
3T-1, 18.0–20.0	22.18	0.174	1.452	0.012	0.729	9.480	0.555	47.176
4X-1, 0.0–2.0	26	0.000	0.000	0.008	0.015	0.906	0.015	1.923
331-C0013E-								
1H-1, 2.0–4.0	0.02	0.003	0.026	0.039	0.276	65.861	0.272	6.986
1H-2, 15.0–24.0	0.31	0.005	0.042	BD	0.095	29.712	0.090	NA
1H-2, 83.0–93.0	0.99	0.004	0.030	BD	0.028	30.006	0.024	NA
1H-2, 124.0–126.0	1.4	0.003	0.021	BD	0.087	23.978	0.085	NA
1H-3, 40.5–42.5	1.975	0.003	0.023	BD	0.123	32.613	0.120	NA
1H-4, 30.0–40.0	2.305	BD	BD	0.007	0.025	25.045	0.025	3.799
1H-4, 68.0–70.0	2.685	BD	0.007	BD	0.024	30.445	0.023	NA
1H-5, 41.0–43.0	3.8	0.004	0.036	BD	0.015	28.347	0.011	NA
1H-5, 76.0–86.0	4.15	0.002	0.017	0.010	0.066	11.984	0.064	6.285
1H-6, 62.0–72.0	5.325	0.003	0.022	BD	0.134	21.128	0.132	NA
1H-6, 99.0–101.0	5.695	0.001	0.011	BD	0.012	21.052	0.010	NA
2H-1, 58.0–60.0	9.08	0.106	0.879	BD	0.331	31.697	0.225	NA
2H-CC, 5.0–7.0	9.545	5.023	41.860	BD	4.881	5.576	BD	NA
5H-1, 82.0–84.0	16.82	0.003	0.023	BD	0.012	5.776	0.010	NA
5H-1, 88.0–96.0	16.88	0.002	0.013	BD	0.020	3.183	0.019	NA
6X-CC, 43.0–45.0	23.43	0.001	0.010	BD	0.012	3.112	0.010	NA
7L-2, 43.0–46.0	26.775	0.005	0.044	BD	0.008	1.424	0.003	NA

Table T9 (continued).

Core, section, interval (cm)	Depth (mbsf)	IC (wt%)	CaCO <sub>3</sub> (wt%)	TN (wt%)	TC (wt%)	TS (wt%)	TOC (wt%)	TOC/TN
9X-CC, 8.0–10.0	45.145	0.002	0.014	0.007	0.016	1.464	0.014	1.976
331-C0013F-								
1H-1, 11.0–13.0	0.11	0.008	0.069	0.124	0.635	37.891	0.626	5.045
1H-2, 30.0–32.0	0.485	0.008	0.063	0.010	0.236	43.268	0.229	22.713
1H-2, 57.0–59.0	0.755	0.008	0.069	0.011	0.200	17.787	0.192	17.529
1H-2, 92.0–94.0	1.105	0.011	0.093	0.016	0.283	11.877	0.272	16.580
1H-3, 28.5–30.5	1.47	0.004	0.036	0.014	0.233	10.264	0.228	15.972
1H-4, 62.0–64.0	2.805	0.005	0.038	0.013	0.164	10.673	0.160	12.643
1H-5, 18.0–20.0	3.335	0.005	0.044	0.010	0.065	21.199	0.060	6.271
1H-5, 86.0–88.0	4.015	0.004	0.033	BD	0.021	29.250	0.017	NA
1H-6, 74.0–76.0	4.895	0.005	0.040	0.024	0.090	11.004	0.085	3.463
1H-7, 62.0–64.0	5.785	0.063	0.521	BD	1.303	13.286	1.241	NA
1H-8, 65.0–67.0	6.82	0.004	0.031	0.008	0.033	22.379	0.029	3.762
1H-9, 94.0–96.0	8.115	0.011	0.089	BD	0.013	14.006	0.002	NA
331-C0013G-								
1H-2, 74.0–76.0	8.71	0.006	0.052	0.013	0.041	10.423	0.034	2.659
331-C0013H-								
1H-2, 21.0–23.0	9.565	0.461	3.839	BD	2.277	16.485	1.816	NA

IC = inorganic carbon, TN = total nitrogen, TC = total carbon, TS = total sulfur, TOC = total organic carbon. BD = below detection, NA = not applicable.

Table T10. Results of direct cell counting, Site C0013.

Core, section	Depth (mbsf)	Cells/mL sediment
331-C0013B-		
1T-1	0.6	ND
1T-1	0.98	ND
1T-CC	1.24	ND
331-C0013D-		
1H-1	3.095	4.36E+06
1H-1	3.29	ND
1H-1	3.67	ND
1H-2	4.305	ND
1H-3	4.88	ND
1H-3	5.955	ND
1H-4	6.905	ND
1H-5	7.715	ND
331-C0013E-		
1H-2	0.16	ND
1H-2	1.09	ND
1H-4	2.405	ND
1H-5	4.25	ND
1H-6	5.425	ND
5H-1	16.96	ND
7L-2	27.22	ND
331-C0013F-		
1H-2	0.157	2.35E+07
1H-3	1.375	8.72E+05
1H-5	3.128	ND
331-C0013G-		
1H-2	8.73	ND

ND = not detected (see Expedition 331 Scientists, 2011b).

**Table T11.** Results of contamination tests using fluorescent microspheres, Site C0013.

Core, section	Depth (mbsf)	Spheres/mL sediment	
		Interior	Outer edge
331-C0013B-			
1T-1	0.6	ND	5.8E+02
1T-1	0.98	ND	4.2E+02
331-C0013D-			
1H-1	3.095	1.6E+04	6.4E+04
1H-2	4.305	5.8E+02	8.4E+04
1H-4	6.905	ND	1.2E+03
1H-5	7.715	ND	0.0E+00
331-C0013E-			
1H-2	0.16	ND	3.9E+02
1H-2	1.09	ND	ND
1H-4	2.405	ND	ND
1H-5	4.25	ND	ND
1H-6	5.425	ND	ND
5H-1	16.96	ND	ND
331-C0013F-			
1H-2	0.157	ND	ND
1H-3	1.375	ND	1.5E+02
1H-5	3.128	ND	ND

ND = not detected.

**Table T12.** Results of contamination tests using perfluorocarbon tracer (PFT), Hole C0013E.

Core, section	Depth (mbsf)	PFT in test vial gas phase (ppm)		Sample weight in test vial (g)		PFT per g sample (ppm)	
		Interior	Outer edge	Interior	Outer edge	Interior	Outer edge
331-C0013E-							
1H-2	0.157	9.02E-03	9.40E+00	3.00	4.45	3.01E-03	2.11E+00
1H-5	3.128	ND	1.96E-02	4.55	2.84	ND	6.90E-03

ND = not detected.